Shaking table model tests of reinforced concrete tunnels under multiple earthquake shakings

Li Meng

Submitted in accordance with the requirements for the degree of
Doctor of Philosophy

The University of Leeds

School of Civil Engineering

September 2023

Declaration

The candidate confirms that the work submitted is his own and that appropriate credit has been given where reference has been made to the work of others. This copy has been supplied on the understanding that it is copyright material and that no quotation from the thesis may be published without proper acknowledgement. The right of Li Meng to be identified as Author of this work has been asserted by Li Meng in accordance with the Copyright, Designs and Patents Act 1988.

Acknowledgements

The research described in this thesis was carried out at the University of Leeds and Southwest Jiaotong University and it could not have been possible without the collaboration and support of many individuals. I greatly appreciate the opportunities my supervisors Professor Nikolaos Nikitas and Professor Raul Fuentes have given to me to become involved with international project as a PhD student at University of Leeds and have the amazing testing experience at Southwest Jiaotong University. They always gave me the guidance and help while preparing the shaking table tests.

I am also grateful to the staff of the National Engineering Laboratory for Technology of Geological Disaster Prevention in Land Transportation (NEDL) at Southwest Jiaotong University for helping to bring this project to realization. I particularly would like to thank Vice-Chancellor Professor Chuan He, who provided me the encouragement when I felt frustrated. I also want to thank Vice-dean Dr Yumin Wen, Professor Yusheng Shen, and Mr. Wubin Wang for their patience and efforts in operating the shaking table. I am very grateful to Professor Wenbo Yang for dedication to the project in coordination with all sides, and without whom the testing would not have proceed as smoothly as it did.

For financial support, I would like to thank School of Civil Engineering, University of Leeds, who provided the full scholarship for my PhD study. Many thanks also go to Professor Nikolaos Nikitas and Professor Raul Fuentes, who secured the funding for these expensive shaking table tests. It should be acknowledged that they gave me the opportunities to roam freely in the ocean of knowledge.

Finally, my special thanks to my parents for their endless love and patience and encouragement during this long journey. Without them, I would not be able to go through all the difficulties and enjoy these successes.

Abstract

The cumulative effect of multiple relatively low or moderate seismic events on tunnels is not well-understood within an earthquake prone region. To investigate the effect of multiple earthquakes on the integrity of tunnel structures, 1 g shaking table tests were performed. This research also explored the impact of tunnel presence on the soil response, namely analyzing soil-structure interaction effects. Within the tests, a free-field model and a soil-tunnel model were employed synchronously.

The shaking table study was designed and conducted following a new set of scaling laws able to faithfully simulate cracking of tunnel lining, and white noise tests were applied after each seismic shaking for dynamic identification. Except for the measurement of acceleration and bending strain, a new cracking monitoring system equipped with wireless mini-cameras was proposed to detect the evolution of tunnel damages during the tests, while Light Detection and Ranging (LiDAR) technology was utilized to examine the ground deformations in the two model configurations.

Based on the point cloud data, it was observed that sand densification effects were obvious in the two models and the influence of tunnel presence on the soil response was restricted in a limited region. The trend in the evolution of an image-based damage index kept similar to that in the progression of surface settlements, implying that the seismically-induced ground failure might play an important role in the seismic response of shallow tunnels. Also, the frequency shifting behaviour of lining did not follow the intuitive pattern, where a reduction in natural frequencies is expected when structural damage occurs. Moreover, the variation of acceleration amplification factors of the tunnel was almost consistent with that of the soil, and the trend of strain agreed with that of surface settlements. The findings from this study provide an insight to better understand the resilience and life-long performance of earthquakes exposed underground structures.

Table of Contents

List of Tables

List of Figures

Chapter 1 Statement of research

1.1 Introduction

Tunnels are an essential part of the public transportation systems in the modern world. As population growth and urbanization continue worldwide, nations look towards underground space for the future infrastructure. 5200 km of tunnels is being constructed each year around the world (Tsinidis et al., 2020). Considering the significant investment on each facility and the long service life (e.g. 100 years), the impact of seismic events on the stability of tunnels needs to be considered carefully.

Tunnels are traditionally considered to be less vulnerable to earthquake ground motions, compared to above-ground structures (Duke and Leeds, 1959; Stevens, 1977; Dowding and Rozen, 1978; Owen and Scholl, 1981; Sharma and Judd, 1991). However, evidences from recent large earthquakes, such as 1995 Kobe earthquake (Asakura and Sato, 1996; Asakura and Sato, 1998), 1999 Chi-Chi earthquake (Wang et al., 2001), and 2008 Wenchuan earthquake (Wang et al., 2009; Li, 2012; Shen et al., 2014), have showed that severe damage, ranging from cracking to collapse, also occurred in tunnels. Hence, many studies recently have been conducted to investigate the seismic response of tunnel linings, including numerical analyses (Kontoe et al., 2011; Tsinidis et al., 2015; Filomena et al., 2020), as well as shaking table tests (Sun et al., 2011; Wang et al., 2015; Xin et al., 2019; Xu et al., 2021) and centrifuge modelling (Cilingir and Madabhushi 2011; Lanzano et al., 2012; Tsinidis et al., 2015). These studies shed light on the behaviour of tunnels under single earthquakes or under progressive excitations with increasing intensities. Nevertheless, the cumulative effect of multiple relatively low or moderate seismic events on tunnels is not well-understood especially within an earthquake prone region. Moreover, a search in U.S. Geological Survey (USGS) reveals that 203 earthquakes near Chengdu, China occurred with a magnitude $M_W > 4.5$ and 2 with a magnitude $M_W > 6$ between May 12 and May 19, 2008, as shown in Figure 1.1, and that 253 earthquakes near Santiago, Chile occurred with a magnitude $M_W > 4.5$ and 13 with a magnitude $M_W > 6$ between September 17 and September 24, 2015, as shown in Figure 1.2. It should be noted that in Figure 1.1 and Figure 1.2 the diameter of each circle is proportional to magnitude.

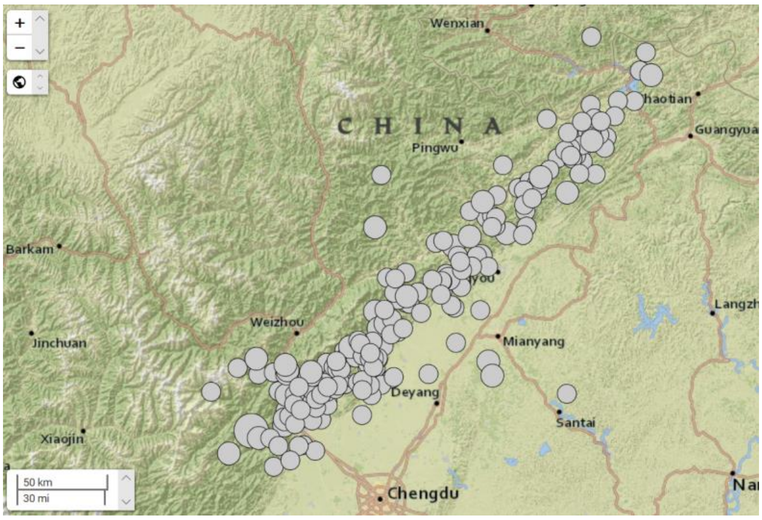

Figure 1.1: Distribution of earthquakes investigated after the 2008 Wenchuan earthquake.

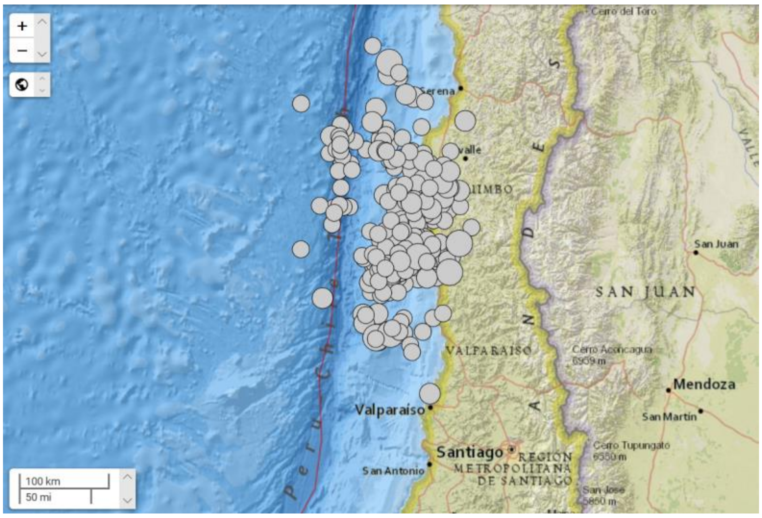

Figure 1.2: Distribution of earthquakes investigated after the 2015 Chile earthquake.

Nowadays, a limited studies have attempted to investigate the impact of cumulative effects on the stability of tunnels under earthquakes with Structural Health Monitoring (SHM) systems. Ikuma (2005) reported the earthquake data collected from a 54 km long Senkai Tunnel in Japan over a 14-year period after it was opened for service. Four large earthquakes occurred during the monitoring period. When the Hokkaido Southwestern Offshore earthquake occurred on July 12, 1993, a maximum PGA of

0.214 g was recorded on the ground surface, while a maximum PGA of 0.056 g was received on the undersea section of the tunnel. Hence, Ikuma indicated that the earthquake acceleration and its impact on the tunnel was much less than that on structures on the ground surface. Additionally, the study pointed out that the strain of the lining had a downward trend and subsequently fluctuated, and its impact on the lining stability was minimal. Wang et al. (2017) implemented a long-term health monitoring system for the Dujiashan tunnel as part of the Guang-Gan Expressway tunnel work of China in the Longmenshan fracture zone. The study presented the stress data of the secondary lining from August 22, 2012 to February 22, 2015 and, found that the axial forces decreased firstly and tended to be stable gradually and the bending moments had fluctuations firstly and subsequently became stable. After the reviewing in USGS, 20 earthquakes with $M_W > 4.5$ occurred during the monitoring period in the Wenchuan earthquake zone. Chiu et al. (2020) installed tri-axial accelerometers and optical fiber displacement meters on the Jiabao tunnel to monitor the life-cycle variations of the structures. 24 earthquakes were recorded in the system with peak accelerations larger than 0.008 g ranging from May 2014 to April 2017. The seismic response of the tunnel under the earthquake on May 25, 2014 was analyzed from the first three predominant frequencies and its amplitudes and the displacements of lining cracks.

Additionally, Sun et al. (2020) highlighted the effects of mainshock-aftershock (MSAS) ground motion sequences on hydraulic arched tunnels with finite element analyses using ABAQUS. 21 as-recorded MSAS ground motions were selected, and the time gap was 10 s between the mainshock and aftershock. The results indicated that MSAS excitations caused relatively severe cumulative damage and had a negative impact on the nonlinear dynamic analyses of the tunnel than applying single mainshock excitations. Meanwhile, the aftershocks increased the damage of the arch part and sidewall part, however there was no significant change at the bottom of the tunnel.

Although the number of tunnels equipped with SHM systems is growing worldwide, the study cases are still limited, particularly for tunnels experiencing many consecutive earthquakes. Degradation due to ageing effects might have an impact on the seismic response of tunnels. For numerical analyses, adequately validated nonlinear models are needed for a more rigorous evaluation of cumulative earthquake action on lining structures. Hence, this study employed 1 g shaking table tests to explore the effect of multiple earthquakes on the properties of tunnel structures.

1.2 Aims and objectives of the research

There are two aims of this research project. The first is to experimentally examine the performance of tunnel structures over the course of multiple earthquake shakings in the transversal direction. The second is to examine the effect of tunnel presence on soil response, namely analyze soil-structure interaction effects. Within the tests, site response test without the tunnel and structure response test with the tunnel will be pursued synchronously. To achieve the above aims there are five objectives that should be addressed:

(1) Simulate tunnel lining with more accurate similarity relations based on two dimensionless parameters. This will eliminate the limitation of previous elastic scaling laws in shaking table damage tests of tunnels and guarantee the similitude of lining nonlinear behaviour between scaled model and prototype.

(2) Examine ground deformations of the soil-tunnel and free-field models synchronously. Sand densification effects and the influence of tunnel presence on the soil response will be assessed quantitatively based on 3D point cloud data.

(3) Track the variation of dynamic properties of tunnel structures. The status of tunnel structures in the course of multiple seismic actions will be evaluated based on the identified parameters such as natural frequencies and damping ratios.

(4) Monitor the cracking process of tunnel lining in typical monitoring sections. The evolution of tunnel damages under multiple earthquake shakings will be analyzed quantitatively based on image data, and its relationship with the variation of structural dynamic properties and ground deformation will be analyzed.

(5) Establish damage patterns of tunnel lining at the end of the tests. The final damage

patterns will provide more evidence to the vulnerabilities of tunnels under multiple earthquake actions.

1.3 Research methodology

The case studies of monitored actual tunnels in seismic prone areas are limited. Shaking table tests, as an advanced method, provide an excellent opportunity to study how the cumulative effect of multiple earthquakes affects tunnel integrity, and afford the ability to do so under controlled and varied conditions. In this project, two rigid containers were employed simultaneously during each shaking, respectively a free-field model and a soil-tunnel model. A new set of scaling laws was used to simulate the cracking process of the lining which was observed by a new cracking monitoring system consisting of distributed mini-cameras. Damage patterns of tunnels were examined and compared with post-earthquake observations in the field. Based on image processing techniques, cracks in acquired images were identified and measured. To quantify the level of tunnel damage, a damage index was defined based on the ratio between the area of lining cracks and the area of original image. Also, the dynamic properties of the tunnel structures were extracted from the white noise tests, while the seismically-induced ground deformations for two systems during the tests were studied with LiDAR technology. Finally, the relationship among data of different sensors was established.

1.4 Outline of the thesis

In Chapter 2, a literature review of previous work relevant to this research is introduced. Its first section describes the tunnel performance in past earthquakes, and presents the typical modes of tunnel damage and failure under seismic loading. A second section reports the shaking table technology, including the theory of scaling laws, and previous experimental work dealing with cumulative damage of tunnels. The third section presents the main change detection approaches used to measure surface elevation changes between multi-temporal point cloud datasets, and the estimation of surface volumetric changes in recent laboratory experiments and field measurements. The fourth section presents the previous image acquisition systems for tunnel crack detections, and the application of image processing techniques for tunnel cracks. The fifth section reports some previous efforts on damage indexes or damage levels utilized to quantify the level of tunnel damage.

In Chapter 3, the experimental models used in this research project are described. The shaking table facility, similarity relations, model containers, test materials and models, and model construction routines are first presented. The instrumentation used in the tests including accelerometers, strain gauges, 3D laser scanner, and mini-cameras is then introduced. Lastly, input motions and loading sequence are explained.

In Chapter 4, the results of the synchronous free-field and soil-tunnel tests are reported. Firstly, the seismically-induced ground deformations are presented based on the 3D point cloud datasets and post-earthquake observations. Secondly, the structural damages are discussed through the image data and post-earthquake observations. Thirdly, the dynamic properties of tunnel structures are analyzed based on the white noise tests. Also, the acceleration amplification effects in the seismic response of the tunnel and soil are presented. Finally, the lining dynamic strains are studied using the strain data at the monitoring positions.

Finally, based on the work presented in this thesis, the main experimental findings are collected and suggestions for future research are given in Chapter 5.

Chapter 2 Literature review

The following sections of this chapter provide a comprehensive review to understand the seismic damage characteristics of tunnels based on post-earthquake observations, the application of shaking table technology on cumulative damage of tunnels, and the methods about quantifying the damage both on the tunnel and the surrounding ground. This chapter is organized as follows. Firstly, observed seismic performance of tunnels in the past earthquakes is presented. Secondly, similitude rules used in previous 1 g shaking table tests of underground structures and previous experimental work about cumulative damage of tunnels are reviewed. Thirdly, change detections between multi-temporal point cloud datasets are discussed. Also, existing crack monitoring system of tunnels and the corresponding image processing techniques of tunnel cracks are presented. Finally, previous damage indexes or levels to quantify the level of tunnel damage are reviewed.

2.1 Seismic performance of tunnels

The seismic response of tunnels is different from that of above ground structures, since kinematic loading induced by the surrounding ground plays an important role compared to inertial loads resulting from the vibration of the tunnel itself (Wang 1993; Hashash et al., 2001). Many researchers have reported the earthquake-induced damage of underground structures. Dowding and Rozen (1978) correlated earthquake-induced tunnel damage with peak ground accelerations from 71 tunnels. Owen and Scholl (1981) extended the above database to 127 cases and concluded that slight damage occurred in rock tunnels for peak ground acceleration below 0.4 g. Sharma and Judd (1991) further extended the database to 192 cases and identified correlations between the extent of damage and influencing factors such as ground conditions, type of support, and peak ground accelerations. They found that tunnel damage decreased with increasing overburden depth, while damage was related to the earthquake magnitude and epicentral distance. Examining the tunnel damages in 1995 Hyogoken-Nambu earthquake, Power et al. (1998) expanded the previous database only considering the shaking induced damage. They concluded that minor damage on tunnels occurred for peak ground acceleration below 0.2 g, while slight to heavy damage for PGA greater than 0.2 g (see Figure 2.1).

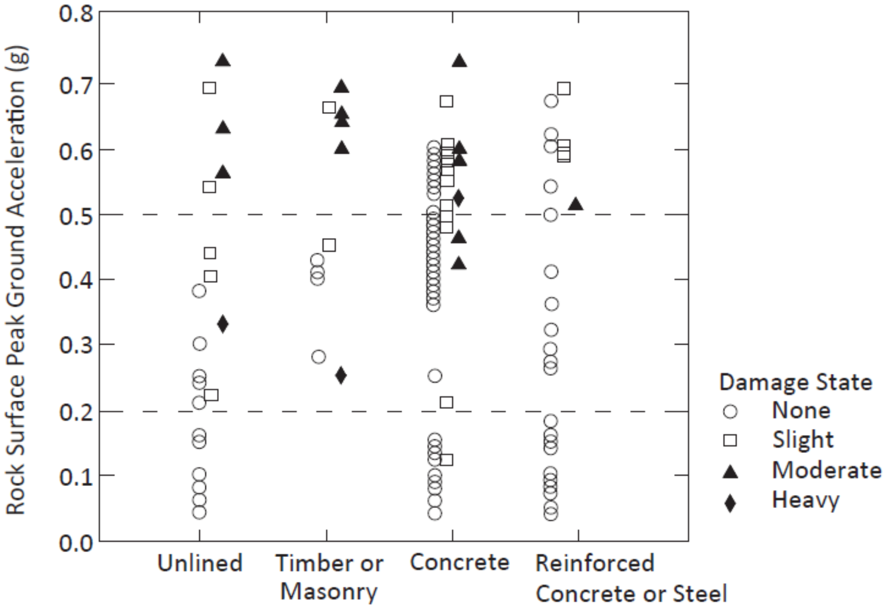

Figure 2.1: Observed bored/mined tunnel damage due to ground shaking (Power et al., 1998).

Wang et al. (2001) investigated 57 mountain tunnels following the 1999 Chi-Chi earthquake; 26% of the 50 tunnels located within 25 km of the earthquake fault were severely damaged, while over 20% of the tunnels were moderately damaged. Typical earthquake induced damage types are presented in Figure 2.2. Clearly, the most common damage types following earthquakes are lining cracks, portal failure, and concrete spalling; the lining cracks can be classified into: longitudinal, transverse, oblique cracks, ring cracks and invert cracks. Similar damage types were observed in mountain tunnels during the 2004 Mid Niigata Prefecture earthquake in Japan (Yashiro et al., 2007; Konagai et al., 2009; Jiang et al., 2010) and the 2008 Wenchuan earthquake in China (Wang et al., 2009; Tao et al., 2011; Chen et al. 2012; Li, 2012; Wang and Zhang 2013; Yu et al., 2013; Yu et al., 2016a,b; Shen et al., 2014). The damage patterns identified by Wang et al. (2001) and associated recorded damage in recent earthquakes are illustrated in Figure 2.3.

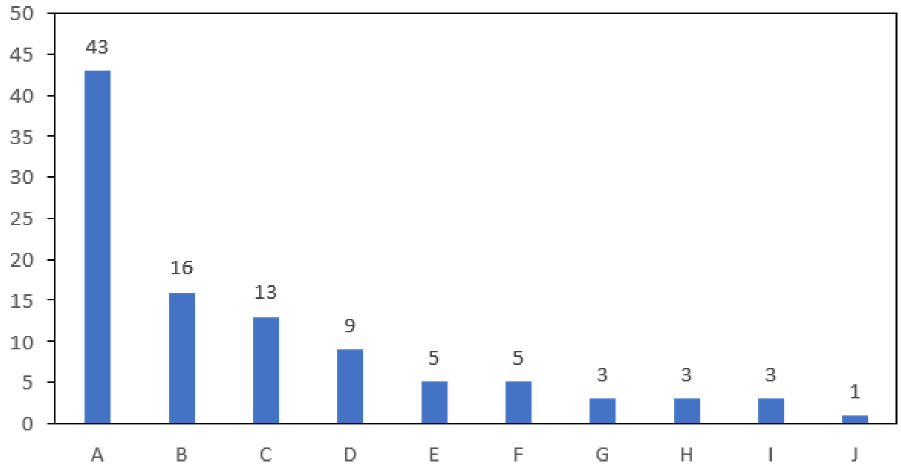

A: Lining cracks, B: Portal failure, C: Concrete spalling, D: Water inrush, E: Exposed reinforcement, F: Displaced lining, G: Pavement cracks, H: Slope induced failure, I: Rock falls in unlined sections, J: Sheard-off lining.

Figure 2.2: Tunnel damages observed in the 1999 Chi-Chi earthquake (redrawn after Wang et al., 2001).

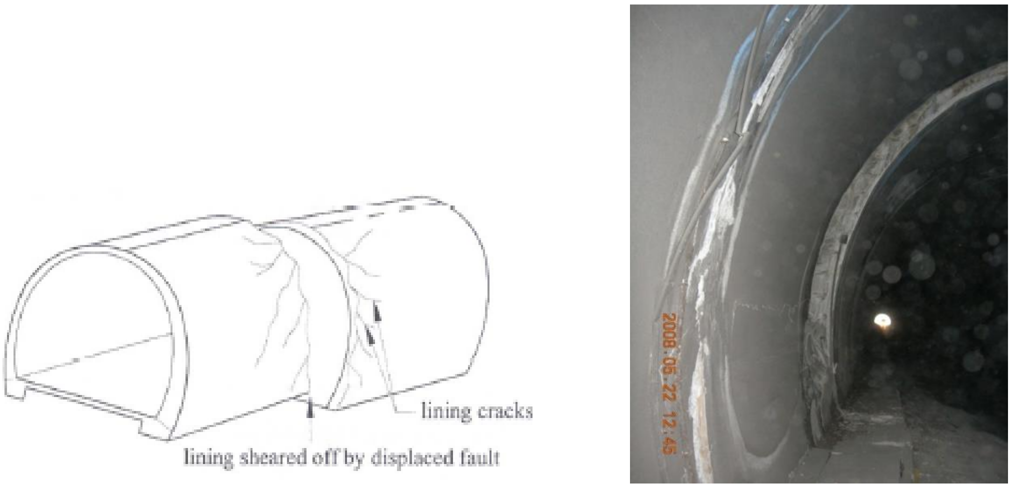

(a) Sheared off lining damage and observed damage at Longxi tunnel in the 2008 Wenchuan earthquake

(b) Slope failure induced tunnel collapse and observed damage at Longdongzi tunnel in the 2008 Wenchuan earthquake

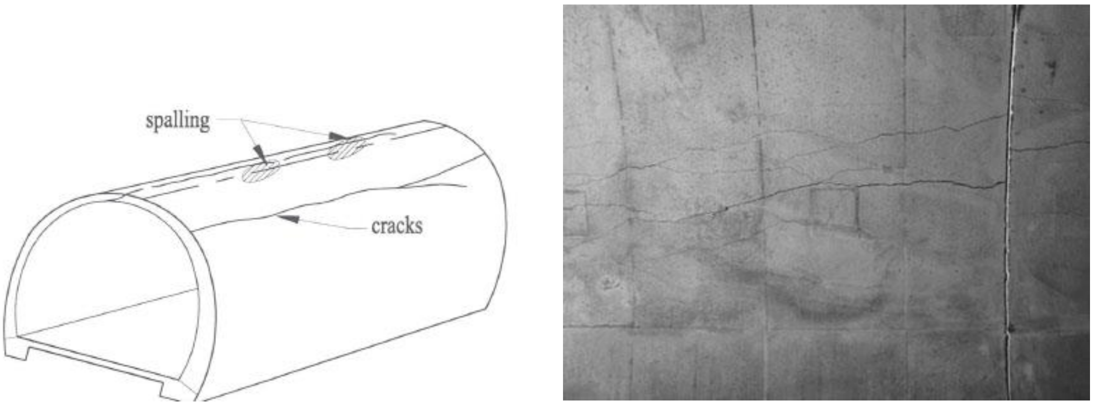

(c) Longitudinal cracks and observed damage at Longxi tunnel in the 2008 Wenchuan earthquake

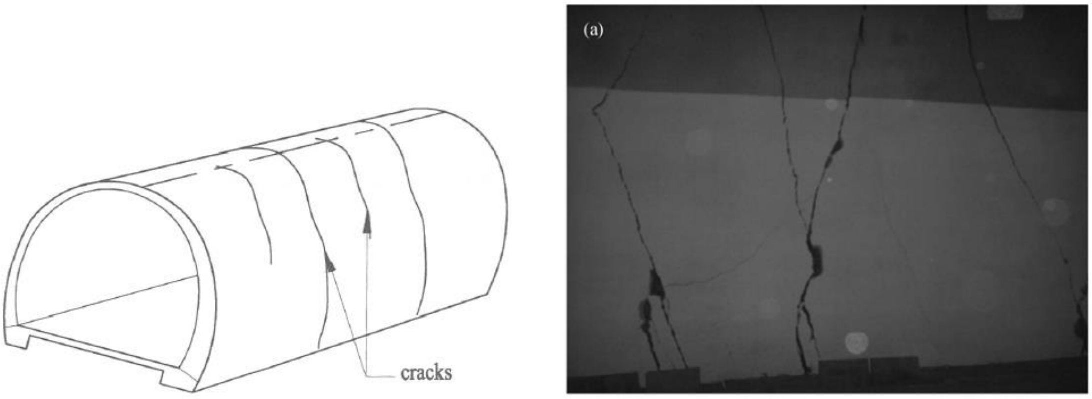

(d) Transverse cracks and observed damage at Longdongzi tunnel in the 2008 Wenchuan earthquake

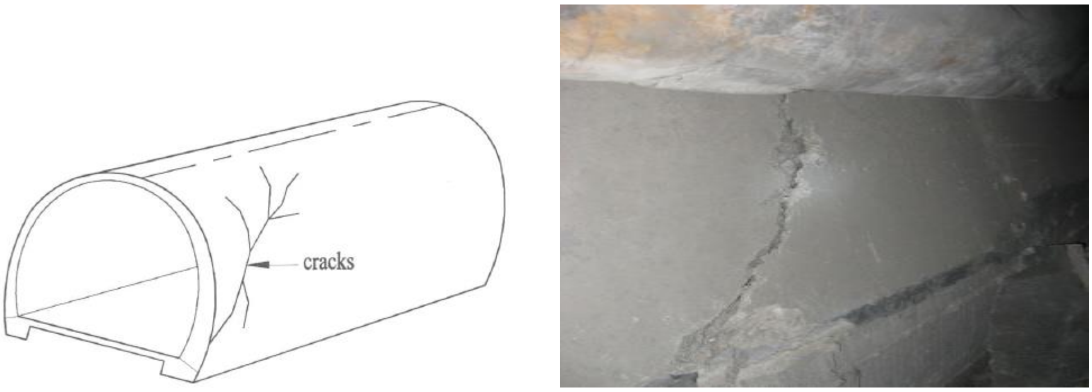

(e) Inclined cracks and observed damage at Jiujiaya tunnel in the 2008 Wenchuan earthquake

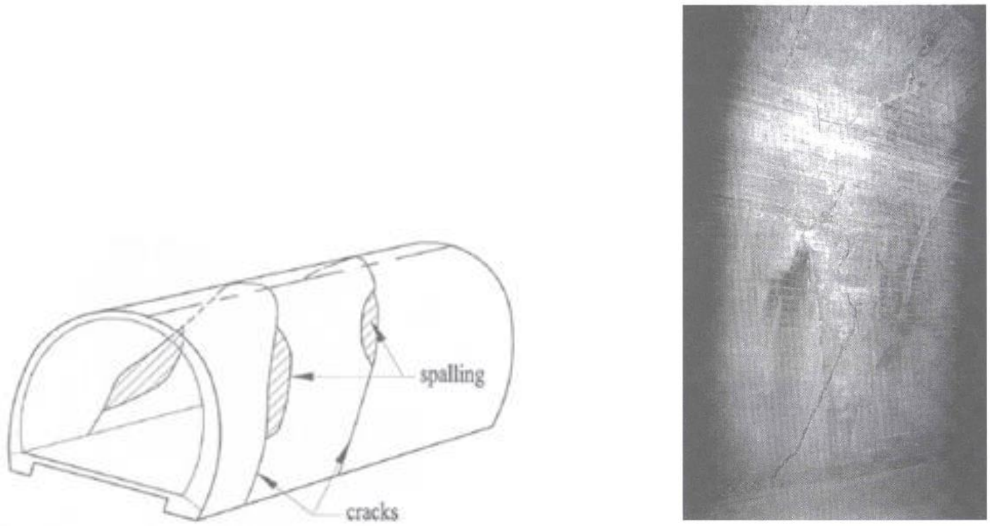

(f) Extended cross cracks and observed damage at No.1 Shuang-Tung Tunnel in the 1999 Chi-Chi earthquake

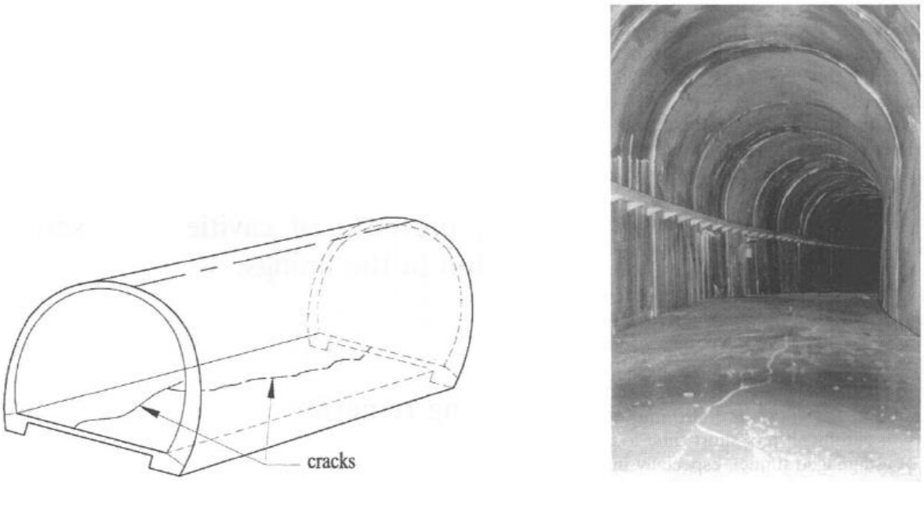

(g) Pavement or bottom cracks and observed damage at No1. San-I railway tunnel in the 1999 Chi-Chi earthquake

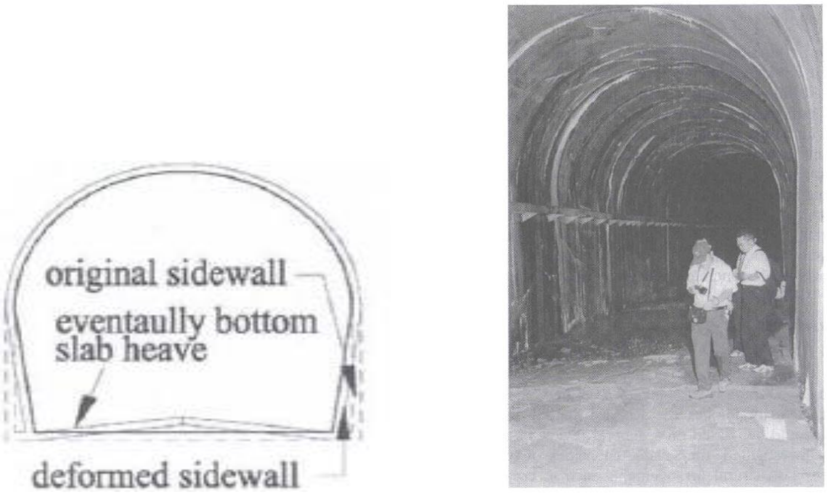

(h) Sidewall/invert deformation and observed damage at No1. San-I railway tunnel in the 1999 Chi-Chi earthquake

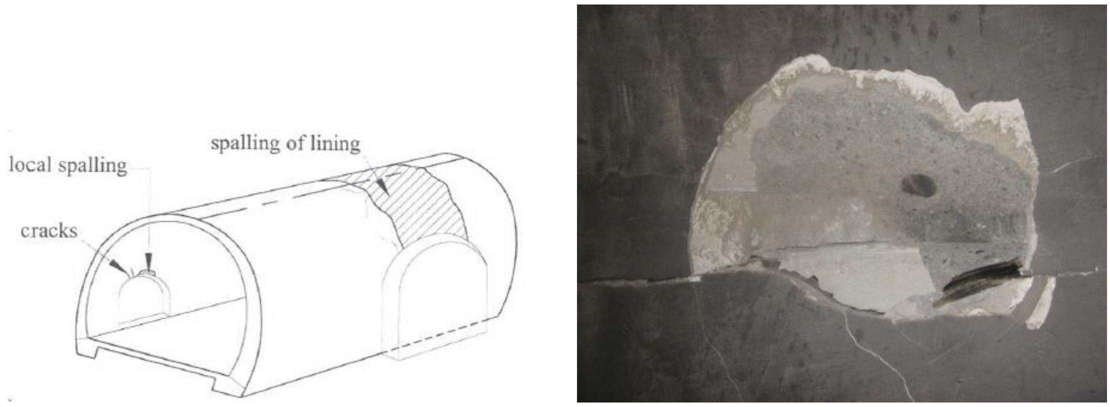

(i) Damage nearby the opening and observed damage at Youyi tunnel in the 2008 Wenchuan earthquake

Figure 2.3: Damage pattern and associated observed damage (Wang et al., 2001; Wang et al., 2009; Geng et al., 2011; Li, 2012).

According to the observation of damage from past earthquakes, damage in underground structures can be induced by two phenomena: ground shaking and ground failure (Wang, 1993). Ground shaking involves effects caused by deformation of the support medium by seismic waves, while ground failure refers to sudden loss of support induced by liquefaction, fault displacement, and slope collapse. For ground shaking, normally three deformation modes are explicitly considered (Owen and Scholl, 1981): (1) axial compression and extension; (2) longitudinal bending; (3) ovaling/racking (Figure 2.4(a) and (b)). Ovaling/racking deformations are caused by the seismic waves normal or nearly normal to the tunnel axis, resulting in a distortion of tunnels' cross-section. It has the significant influence on the seismic behaviour of tunnels, and is taken into account in this research. On the other hand, the surrounding ground experiences large permanent deformations due to seismically-induced ground failure, which may cause the significant damages of shallow tunnels. Although many experimental and numerical studies focused on the behaviour of tunnels under single earthquakes or under seismic excitations with increasing intensities, the cumulative effect of multiple seismic events is not well-understood within an earthquake prone region. Therefore, it is necessary to further investigate the impact of such cumulative effect on the tunnel integrity.

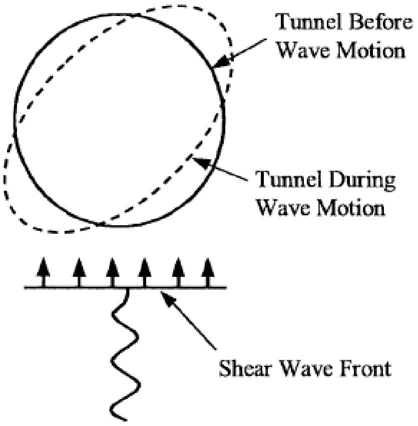

(a) Ovaling deformation of circular tunnel section

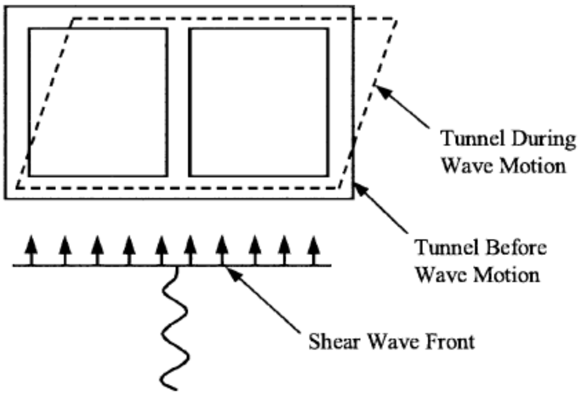

(b) Racking deformation of rectangular tunnel section

Figure 2.4: Ovaling/Racking deformation modes due to seismic waves (Owen and Scholl, 1981).

2.2 Shaking table technology

2.2.1 Scaling laws

Model similitude provides the relationship between the test model and prototype. Based on the Buckingham-π theorem, dimensional analysis was adopted to determine the similarity relations of physical parameters in the test program (Meymand, 1998). For 1 g shaking table tests, the objective is to achieve dynamic similarity, which means a condition where homologous parts of the model and prototype experience homologous net forces (Langhaar, 1951). In this section, four derived similitude rules, used in previous 1 g shaking table tests of underground structures, including elastic-gravity similarity law, elastic similarity law (gravity distortion method), artificial mass method, and general similarity law (less artificial mass method), will be described.

2.2.1.1 Elastic-gravity similarity law

In dynamic tests of structures, relationship of physical quantities of interest can be expressed as:

$$f(\sigma, l, E, \rho, T, u, v, a, g, \omega) = 0 \qquad (2.1)$$

Where σ is stress, l is length, E is elastic modulus, ρ is density, T is time, u is displacement, v is velocity, a is acceleration, g is gravitational acceleration, and ω is circular frequency.

Length l, density ρ, and elastic modulus E are selected as the fundamental physical quantities, and then other physical quantities can be expressed by them based on dimensional analysis. Therefore, equation (2.1) can be converted to,

$$f = \left(\frac{\sigma}{E}, \frac{t}{l\sqrt{\rho/E}}, \frac{u}{l}, \frac{v}{\sqrt{E/\rho}}, \frac{a}{E/\rho l}, \frac{g}{E/\rho l}, \frac{\omega}{l^{-1}E^{0.5}\rho^{-0.5}}\right) = 0 \qquad (2.2)$$

Dimensionless parameters are defined as,

$$\pi_1 = \frac{\sigma}{E},\ \pi_2 = \frac{t}{l\sqrt{\rho/E}},\ \pi_3 = \frac{u}{l},\ \pi_4 = \frac{v}{\sqrt{E/\rho}},\ \pi_5 = \frac{a}{E/\rho l},\ \pi_6 = \frac{g}{E/\rho l},\ \pi_7 = \frac{\omega}{l^{-1}E^{0.5}\rho^{-0.5}}$$

These dimensionless parameters should be the same for the model and prototype structures. S is defined as the similarity ratio of the model to prototype structures (m/p), and then the following similarity relations can be obtained,

$$S_\sigma = S_E \tag{2.3}$$

$$S_T = S_l S_E^{-0.5} S_\rho^{0.5} \tag{2.4}$$

$$S_u = S_l \tag{2.5}$$

$$S_v = S_E^{0.5} S_\rho^{-0.5} \tag{2.6}$$

$$S_a = S_l^{-1} S_E S_\rho^{-1} = S_g \tag{2.7}$$

$$S_\omega = S_l^{-1} S_E^{0.5} S_\rho^{-0.5} \tag{2.8}$$

Where S_l, S_ρ, S_E are the similarity ratios of length, density, and elastic modulus respectively, S_σ, S_T, S_u, S_v, S_a, S_g, and S_ω are the similarity ratios of stress, time, displacement, velocity, acceleration, gravitational acceleration, and circular frequency respectively.

In elastic-gravity similarity law, $S_g = 1$ is considered. Then equation (2.7) is converted to,

$$S_\rho = S_E / S_l \tag{2.9}$$

Based on equation (2.9), equations (2.4), (2.6), (2.7), and (2.8) are converted to equations (2.10), (2.11), (2.12), and (2.13) respectively. Similarity relations for the elastic-gravity similarity law are summarised in Table 2.1.

$$S_T = S_l^{0.5} \tag{2.10}$$

$$S_v = S_l^{0.5} \tag{2.11}$$

$$S_a = S_g = 1 \tag{2.12}$$

$$S_\omega = S_l^{-0.5} \tag{2.13}$$

Table 2.1 Similitude rules in shaking table damage tests of underground structures.

Physical quantity	Elastic-gravity similarity law	Elastic similarity law (Gravity distortion method)	Artificial mass method	General similarity law (Less artificial mass method)
Length	S_l	S_l	S_l	S_l
Density	$S_\rho = S_E S_l^{-1}$	S_ρ	S_ρ	S_ρ
Elastic modulus	S_E	S_E	S_E	S_E
Strain	$S_\varepsilon = 1$	$S_\varepsilon = 1$	$S_\varepsilon = 1$	$S_\varepsilon = 1$
Stress	$S_\sigma = S_E$	$S_\sigma = S_E$	$S_\sigma = S_E$	$S_\sigma = S_E$
Time	$S_T = S_l^{0.5}$	$S_T = S_l S_E^{-0.5} S_\rho^{0.5}$	$S_T = S_l^{0.5}$	$S_T = S_l S_E^{-0.5} S_\rho^{0.5}$
Velocity	$S_v = S_l^{0.5}$	$S_v = S_E^{0.5} S_\rho^{-0.5}$	$S_v = S_l^{0.5}$	$S_v = S_E^{0.5} S_\rho^{-0.5}$
Displacement	$S_u = S_l$	$S_u = S_l$	$S_u = S_l$	$S_u = S_l$
Acceleration	$S_a = 1$	$S_a = S_l^{-1} S_E S_\rho^{-1}$	$S_a = 1$	$S_a = S_l^{-1} S_E S_\rho^{-1}$
Gravitational acceleration	$S_g = 1$	/	$S_g = 1$	/
Artificial mass	/	/	$m_a = S_E S_l^2 m_P - m_m$	$0 \le m_a \le S_E S_l^2 m_P - m_m$

2.2.1.2 Elastic similarity law

In the elastic-gravity similarity law, S_l, S_ρ, and S_E cannot be selected randomly due to the equation (2.9), which is difficult for the selection of model materials. Two alternatives, elastic similarity law (gravity distortion method) and artificial mass method, are used to solve this problem (Meymand, 1998). In elastic similarity law (Zhang, 1997; Lin et al., 2000), the similarity of gravitational acceleration ($S_g = 1$) is ignored. Therefore equation (2.7) can be adjusted to equation (2.14), and other similarity relations are the same as equations (2.3), (2.4), (2.5), (2.6), and (2.8). Similarity relations of the elastic similarity law are presented in Table 2.1. According to previous research (Lin et al. 2000; Chi and Lin, 2004), elastic similarity law is suitable to study natural frequency and vibration modes of structures, compared to the elastic-gravity similarity law.

$$S_a = S_l^{-1} S_E S_\rho^{-1} \tag{2.14}$$

2.2.1.3 Artificial mass method

In the artificial mass method (Zhang, 1997; Lin et al., 2000), artificial mass is fixed on the model structures supplementing the gravity and inertial forces of model structures due to the usual model materials with properties of large density and small elastic modulus. The stiffness of structures cannot be affected by the artificial mass blocks. Based on equation (2.9), the artificial mass m_a is calculated by,

$$m_a = S_m m_P - m_m = S_E / S_l \, S_l^3 m_P - m_m = S_E S_l^2 m_P - m_m \tag{2.15}$$

Where S_m is the similarity ratio of mass, m_m and m_p are the mass of model structure (without artificial mass) and prototype structure respectively.

Other similarity relations are the same as equations (2.3), (2.5), (2.10), (2.11), (2.12), and (2.13), and all similarity relations of the artificial mass method are summarised in Table 2.1.

2.2.1.4 General similarity law

Practically, artificial mass method cannot be achieved seriously due to the limitations of loading capacity of shaking table and available spaces of model structures. General similarity law (less artificial mass method) (Zhang, 1997), which is between the elastic similarity law and artificial mass method, is proposed. Its similarity relations are the same as equations (2.3), (2.4), (2.5), (2.6), (2.8), and (2.14) in which artificial mass m_a

ranges from 0 to $S_E S_l^2 m_P - m_m$. If $m_a = 0$, similarity relations of the general similarity law are the same as that of the elastic similarity law, while if $m_a = S_E S_l^2 m_P$, it is the same as that of the artificial mass method. Similarity relations of the general similarity law are summarised in Table 2.1.

2.2.1.5 Comparisons of theses similitude rules

Based on the above analysis, four similitude rules have been used in previous shaking table tests of underground structures, and their relationships are illustrated in Figure 2.5. Also, the differences within the similitude rules of structures are described in Table 2.2.

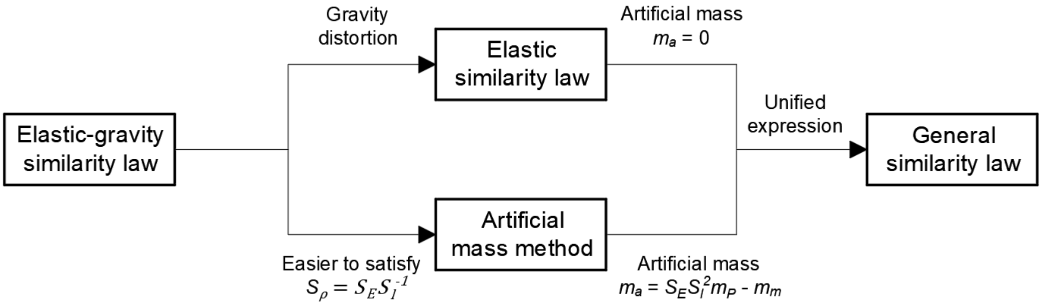

Figure 2.5: Relationship within similitude rules of underground structures.

Theoretically, elastic-gravity similarity law should be satisfied strictly for the similarity relations between the model and prototype structure in damage tests, but sometimes it is simplified for some reasons such as the capacity and size limitations of shaking table, the selection of model material, and the fabrication of model structure. Moreover, some factors are not considered in these similitude rules, such as the similitude of stress-strain curves and similitude of fracture characteristics. The former could be attempted by using the suitable model materials such as micro-concrete and emulation concrete, while the latter could be solved through the derivation of new similarity relations involved the fracture parameters. Overall, existing similitude rules cannot guarantee the similitude of the structural nonlinear behaviour while simulating the tunnel lining. Therefore, it is necessary to further investigate the more accurate similarity relations.

Table 2.2 Comparisons of similitude rules of structures in shaking table damage tests.

NO.	Similitude rules	Assumptions	Limitations
1	Elastic-gravity similarity law (Sun et al., 2011; Wang et al., 2015; Yang et al., 2015; Xin et al., 2019; Shen et al., 2020)	No lack of gravity and inertial force.	Similarity relation $S_\rho = S_E S_l^{-1}$ restricts the selection of model material.
2	Elastic similarity law (Gravity distortion method) (Meng et al., 2016; Sui et al., 2017; Xu et al., 2021)	Similitude of gravitational acceleration ($S_g = 1$) is ignored. (gravity distortion model)	It is not applicable to plastic or destructive stage of model structure.
3	Artificial mass method (Chen et al., 2013; Xin and Gao, 2014; Tao et al., 2015)	1) Similarity relation $S_\rho = S_E S_l^{-1}$ is easier to be achieved for selection of model material by supplementary artificial mass. 2) Artificial mass blocks do not affect the stiffness of model structures, 3) No lack of gravity and inertial force.	1) Internal space of model structure should be sufficient for putting artificial mass blocks (Generally the size of tunnel model structure is small), 2) Loading capacity of shaking table is limited.
4	General similarity law (Less artificial mass method) (Yu, 2013; Chen et al., 2015; Quan, 2016)	1) Artificial mass is not sufficient due to the limitation of loading capacity of shaking table and internal space of model structure, 2) Artificial mass blocks do not affect the stiffness of model structures, 3) Lack of part gravity and inertial forces.	Model structures are easier to damage.

2.2.2 Model tunnel shaking table tests

Based on the above similitude rules, 1g shaking table tests have been used to study the dynamic response of tunnels under seismic loadings by many researchers. The model tunnels have been modelled by gypsum (Xu et al., 2016), reinforced concrete (Jiang et al., 2010, Chen et al., 2010), micro-concrete (cement-aggregate-water mixtures), reinforced with steel mesh or polypropylene fibers (Xin et al., 2019), organic glass (Wang et al., 2018), and aluminium (Yu et al., 2018). Gypsum has been used for many years, particularly for analyses in the elastic stage, due to its high workability and linear or nearly linear stress–strain relationship. However, its stress-strain response is different from that of prototype concrete especially when entering the non-linear post-cracking stage, while it also shows the larger tensile strength. Microconcrete, the mix of cement, coarse sand, fine sand, and water, has similar stress-strain curves with concrete.

Based on these model materials, some research work focuses on the damages of underground structures using the shaking table tests (Sun et al., 2011; Wang et al., 2015; Meng et al., 2016; Xin et al; 2019; Shen et al; 2020; Xu et al; 2021). Sun et al. (2011) performed shaking table tests to investigate the nonlinear seismic response of portals of two parallel tunnels fabricated by gypsum material and the interaction between lining and surrounding rock, using the elastic-gravity similarity law. The results indicated that when seismic wave went through the model material, the low-frequency segment of acceleration response was magnified and the high-frequency segment was attenuated according to the Fast Fourier Transform (FFT) results of acceleration signals on the tunnel invert. The damage of left and right tunnels was distinctly different on the amount of cracks, width of cracks and distribution laws of cracks. The through cracking mainly located at the spandrel and arch springing. Also, the cracking of surrounding ground appeared obvious horizontal shear failure due to the sol-structure interaction effects. For this damage test, the authors did not consider the similarity laws in post-cracking phase while scaling the tunnel lining, and also the gypsum material had the limitation in simulating the concrete.

Wang et al. (2015) researched the progressive damage of unreinforced concrete linings under increasing intensities by 1 g shaking table tests. The elastic-gravity similarity relations were employed and the model tunnel was simulated with gypsum material. Crack patterns were observed in the experiment, including the longitudinal crack at the shoulder, inclined crack at the sidewall, and longitudinal crack on the invert, which is similar to the observation in the field investigation. The effect of cracking on the seismic performance of tunnel lining was identified by the degradation of the dominant frequency of tunnel lining after each excitation, see Figure 2.6. This frequency was extracted based on the transfer functions of response signals of invert accelerometer. Finally, the damage states of tunnel lining were proposed based on the PGA, Modified Mercalli (MM) intensity and damage description of lining. For this damage test, the authors observed the development of tunnel cracking after each excitation, which is useful to better describe the damage progress of lining, however the quantitative information of cracking such as width and length was not obtained. In addition, the similarity law in post-cracking phase were not considered and the gypsum material with linear characteristic was used to simulate the concrete lining.

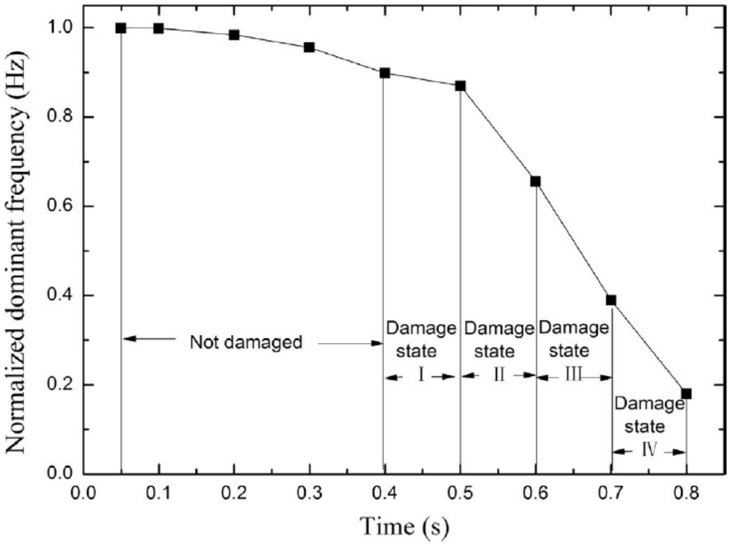

Figure 2.6: Decrease of normalized dominant frequency with progressive damage states (Wang et al., 2015).

Meng et al. (2016) investigated the dynamic responses of fiber reinforced concrete tunnel lining under increasing seismic intensities with shaking table tests. The lining was simulated by the microconcrete (cement-sand-water)-fiber and the similarity ratios were obtained based on the gravity distortion method. During the tests, a crack observation system equipped with five cameras was used to monitor the vulnerable positions including crown, shoulder, sidewall, springing and invert. Each camera can cover the region of 80 mm*80 mm on the lining inner surface. The results indicated that the using of fiber can postpone the occurrence and development of tunnel cracking to some extent, compared to the results of plain concrete tunnel lining. Longitudinal cracks occurred at the shoulder, sidewall, springing and invert, and the development of cacking on the tunnel invert was shown in Figure 2.7. For this damage test, although microconcrete was used to simulate the lining, there were limitations by using gravity distortion method as the similitude rules when entering the destructive stage of model structure. Also, the use of camera was an important step towards the automatic cracking monitoring of tunnel lining, but digital image processing techniques were not applied to extract the cracks for further analysis.

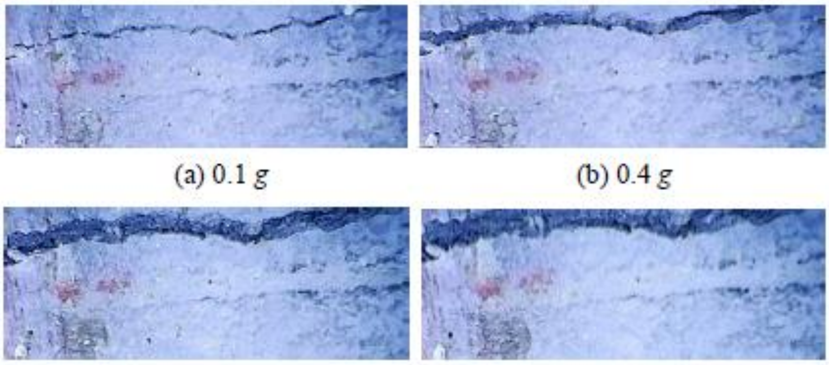
(a) 0.1 g (b) 0.4 g

(c) 0.8 g (d) 1.0 g

Figure 2.7: Evolution of damage on the invert of fiber reinforced concrete tunnel lining (Meng et al., 2016).

Xin et al. (2019) employed shaking table tests to investigate the progressive damage of scaled model tunnels with plain concrete (PC), steel reinforced concrete (RC), and polypropylene fiber reinforced concrete (PFRC) under increasing seismic intensities. Similarity ratios were derived based on the elastic-gravity similarity law, and the geometry, density and elastic modulus were selected as the fundamental physical parameters. The lining was fabricated by microconcrete made of ordinary Portland cement, 0.15–2.5 mm medium sand and water, and the flexibility of lining was improved by steel rebar and polypropylene fiber. Five cameras, installed on a wood stick along the longitudinal direction of lining, were utilized to track the evolution of tunnel damage during the shakings. The results demonstrated that Polypropylene fiber changed the brittle behavior of PC and the damage patterns of RC along with the distribute paths of cracks, and can postpone the appearance and propagation of cracks. Therefore, PFRC had the potential for application in the large deformation sections of tunnel lining in soft surrounding rock due to its better aseismic performance. For this nonlinear seismic response test, the limitation in similitude rules was still existed. Furthermore, there were not quantitative analysis of cameras' results, just qualitative descriptions.

Xu et al. (2021) conducted 1 g shaking table model tests to study the seismic performance of precast horseshoe segmental tunnel (PHST) in the transversal direction. The laminar box was used to simulate the free-field boundary, reducing the influence of boundary on the soil-tunnel system. The elastic similarity rule was applied in the design of tunnel lining and three basic physical parameters were geometry, acceleration and elastic modulus respectively. Micro-aggregate-concrete and galvanized steel wire were used to cast the tunnel lining, while sand collected from the site of PHST was adopted to model the surrounding ground. During the multiple shakings, the inner views of lining were recorded by a video camera, and the settlement of soil surface was measured by three laser displacement sensors. The results demonstrated that with the increasing of seismic intensity, the dominant frequencies of lining decreased first and then kept steady, whereas the damping ratios of lining increased first and then kept steady, which might result from the combined effects of soil shear deformation, structural damage and soil settlement. It should be noted that no damage of lining was observed at the 0.2 g stage and obvious damage occurred after the 0.4 g stage. For these non-linear dynamic response tests, the elastic similarity relations cannot guarantee the similitude in post-cracking phase and more accurate similitude rules need to be explored. Also, the settlement values measured by laser displacement sensors only focused on several points, which cannot reflect the deformation of whole soil surface. As for the data of video camera, the lining cracks were not extracted.

2.3 Change detection of point cloud datasets

LiDAR technique as a remote sensing method is increasingly used in the applications of topography change detection to various scales since it can provide highly dense and accurate point cloud data with non-contact and time-saving properties (Brodu and Lague, 2012; Qin et al., 2016; Telling et al., 2017). The measurement is based on the reflected energy from emitted laser pulse after interacting with media and objects. There are four main change detection approaches to measure surface elevation changes between multi-temporal point cloud datasets, including Digital Elevation Models of difference (DoD) (Wheaton et al., 2010), Cloud to Cloud (C2C) (Girardeau-Montaut et al., 2005), Cloud to Mesh (C2M) (Cignoni et al., 1998), and Multiscale Model to Model Cloud Comparison (M3C2) (Lague et al., 2013). DoD is the common method when the geometry of the surface is planar. Two points clouds are gridded to generate DEMs, followed by producing a DoD to calculate the vertical distances at each cell of grid. The fixed resolution of this method strongly limited the exhibition of different characteristic scales. C2C is the simplest and fastest method to compare the two point clouds, which computes the distance from each point in the compared cloud to the closet point in the reference cloud, as shown in Figure 2.8(a). It does however not provide accurate distance measurement, suitable for the very dense point clouds. C2M computes the surface height changes between a point cloud and a mesh constructed from the reference point cloud, as shown in Figure 2.8(b). The meshing process reduces the local properties of surface and increases the time-consuming steps. DoD and C2M, as the indirect comparison of two point clouds, require the gridding or meshing processes.

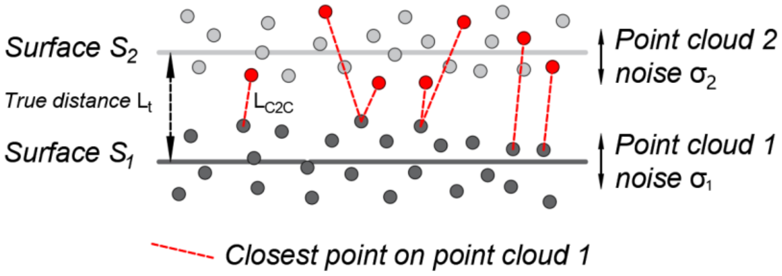

(a) C2C

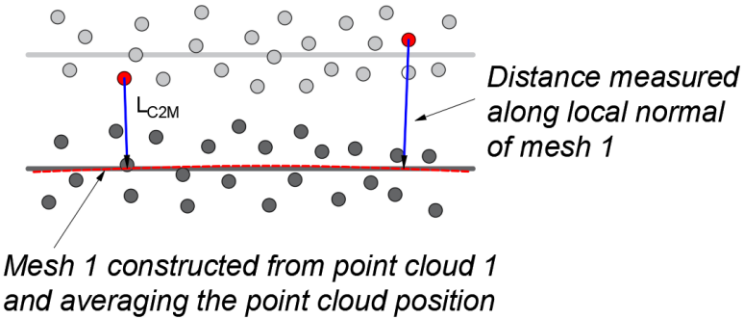

(b) C2M

Figure 2.8: Description of the C2C and C2M methods (redrawn after Lague et al., 2013).

Lague et al (2013) filled this gap and proposed the M3C2 algorithm which can measure the distance on two 3D point clouds directly without any gridding or meshing, thus avoiding the interpolation errors. The local normal vector is estimated based on each point's neighborhood for core points which can be the entire reference cloud or a subset of reference cloud, as shown in Figure 2.9(a). The search cylinders then are created along the local normal vector to calculate the locally average change between two epoch clouds, as shown in Figure 2.9(b). Meanwhile, a spatially variable confidence interval is firstly constructed to assess significant changes, considering the uncertainties from surface roughness, position uncertainty, and registration error. Although the M3C2 algorithm is a 3D method, it can be used as a substitute of the DoD method under 2D surface conditions. For the comparison of C2M and M3C2 on synthetic point clouds, Lague et al (2013) concluded that the C2M method can be accurate as the M3C2 algorithm on calculating the average vertical distances, but not offering the estimation of spatially variable confidence interval. Barnhart and Crosby (2013) found that the

M3C2 algorithm was more robust to estimate elevation changes than the C2M method in Terrestrial Laser Scanning (TLS) data of different timespan.

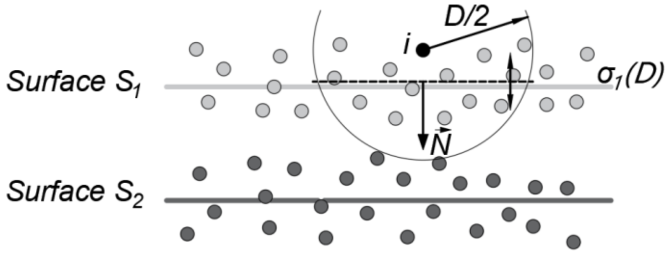

(a) Estimation of local normal vector at a scale D around the core point i

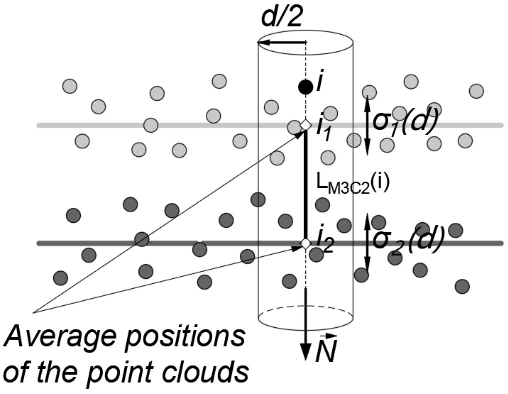

(b) Average distance between the two clouds at a scale d along the normal vector

Figure 2.9: Description of the M3C2 method (redrawn after Lague et al., 2013).

The estimation of surface volumetric changes between two successive scans follows the elevation change detections in recent studies including laboratory experiments (Li et al., 2020; Gao et al., 2021) and field measurements (Benjamin et al., 2016; Goodwin et al., 2016; Eltner et al., 2018; Bernard et al., 2020; DiFrancesco et al., 2020; Gomez-Gutierrez and Rito Goncalves, 2020; Winiwarter et al., 2021). Li et al. (2020) measured the soil erosion on experimental plots (12 m^2) with three slope treatments through 11 simulated rainfall applications via terrestrial LiDAR technology. The surface elevation changes were detected by the M3C2 algorithm in the software CloudCompare. Points with significant changes (M3C2 distances greater than Level of Detection (LOD)) were found as shown in Figure 2.10 and then projected on to the 10 mm grid. The average differences in height of all points inside the grid was calculated for each cell. The volumetric changes were estimated as the sum of the contribution of each cell dV=cell size*cell size*difference of height. The sign of volume indicated the eroded volume (-) and deposited volume (+). Finally, the eroded mass was estimated based on the volumetric changes and density (i.e. soil bulk density and runoff sediment density), and was compared to the measured sediment yield. The results indicated that LiDAR could be a feasible tool to quantify the soil erosion, but low levels of erosion might add the uncertainty for measurement.

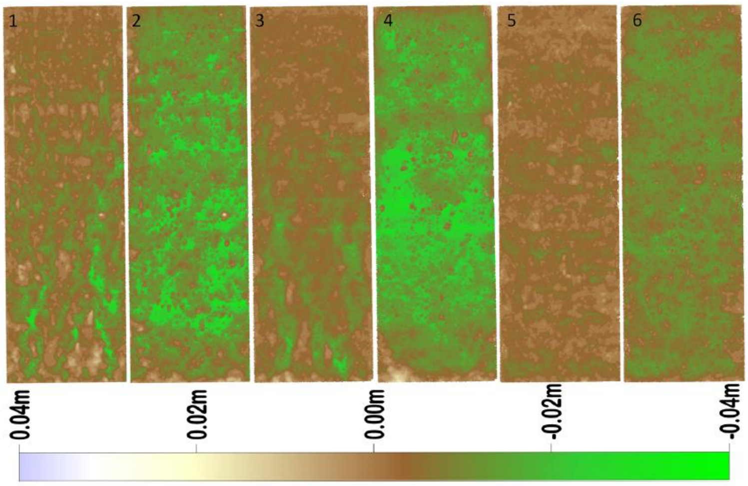

Figure 2.10: Significant surface elevation changes compared with initial surfaces (1-2 for 20 % slope; 3-4 for 12 % slope; 5-6 for 5 % slope) (Li et al., 2020).

On 14 November 2016, Kaikoura region, New Zealand was hit by the earthquake with a magnitude of M_W=7.8. Bernard et al. (2020) detected and measured the landslides of this region (5 km^2) with 3D point clouds data obtained by airborne LiDAR technology. Two approaches, 3D-M3C2 and vertical-M3C2, were applied in the software CloudCompare. The 3D approach was used to detect geomorphic changes. Considering that 'shadow zone' effects can be caused by 3D normals due to surface roughness, the landslide volume was estimated with the vertical approach. Corresponding significant changes were assigned to the regular grid cells spaced by 1 m and the landslide volume was simply the sum of the vertical-M3C2 distances. The results indicated that 3D point cloud differencing had a greater sensitivity to detect small distance changes compared to the traditional DoD method. The volume uncertainty was specific to each landslide source and deposit and depended on the local surface properties like roughness, the number of points and registration error, thus it was calculated from the sum of the 3D-

M3C2 uncertainty measured for each core point. Benjamin et al. (2016) estimated the rockfall volume with different change detection methods (DoD, M3C2, C2C, and improved C2C methods) based on two TLS datasets obtained from coastal cliffs of Staithes, North Yorkshire, UK. The results indicated that rockfall geometry has a notable influence to quantify rockfall volume for these methods due to view angle and surface texture. The DoD volume estimation was larger than all other methods, especially over 25% compared to the M3C2 significant results. They thus suggest that DoD, as a 2.5D raster method, may overestimate rockfall volumes.

These studies demonstrated the wide application of M3C2 algorithm on soil erosion, landslides, and rockfalls for the estimations of surface elevation and volumetric changes. However, the systematic detections for the seismically-induced ground deformations of the synchronous free-field and soil-tunnel systems through 3D point clouds have not been attempted. Additionally, it is common that occlusion effects exist during TLS data acquisition due to the location of scanner and the roughness characteristics of surfaces (Brodu and Lague, 2012). Although multiple scanning positions can obviously reduce this issue, it will increase the acquisition efforts and time, not feasible for some measurements. Interpolation can be used to fill in the voids within the points from surrounding data with simple linear interpolation or nearest neighbor methods or more advanced techniques (Telling et al., 2017). Interpolation should be applied after the calculation instead of on the raw point cloud.

2.4 Crack monitoring and identification of tunnels

With the utilization of underground space (National Research Council, 2013; United Nations, 2019), concerns have been raised on the condition assessment of existing underground structures during the operational life with inspection and monitoring, owing to aging and natural disasters like seismic events. Cracks are the primary indicator of structure degradation and its development might impact the integrity of structures and reduce the serviceable life, even collapse (Asakura and Kojima, 2003; Wang et al., 2015; Attard et al., 2018). Therefore, timely and accurate inspection or monitoring is of great importance to the maintenance of underground structures and prevention of accidents.

Conventionally, visual inspection with manual measurement is used to detect the lining defects such as crack, spalling, and corrosion by trained inspectors. However, such method lacks objectivity to assess the status of structures, highly depending on the knowledge and experience of inspectors, hence leading to possible inaccuracies, false positives, and missing. It is also time-consuming and laborious for tunnel structures, particularly when inspection tasks are expected to be completed at late night. As computer vision (CV) techniques have been booming in the field of civil infrastructures over the recent years, image processing (IP) is involved in the detection and measurement of concrete cracks from captured image data with reliable, time-saving, and automatic properties (Koch et al., 2015; Mohan and Poobal, 2017; Spencer et al., 2019). However, compared to IP for crack detection in pavements and bridges (Ouyang et al., 2011; Oliveira and Correia, 2013; Ai et al., 2018), the application in tunnels is limited since the low and uneven lighting, serious noise, and background interference. Therefore, the image acquisition system for tunnel crack detections needs to be individually designed to capture the high-quality image data, mainly consisted by camera, light source, power, storage, and control device. Furthermore, during the image processing such as contrast enhancement, segmentation, and morphological operations, the suitable methods need to be used to identify and measure the cracks.

Ukai (2007) developed a tunnel scanner with multiple line sensor cameras capable of taking panoramic annular images of the lining surface, to carry out crack detection at low cost. The system equipped with Hydrargyrum Medium-Arc Iodide (HMI) lighting was mounted on the railcar which can move at the speed of 10-30 km/h. An improved method was utilized to perform the focus adjustments, by evaluating the sharpness of the picture signal waveforms using threshold values calculated from the first derivation histogram. Once the tunnel-scanning work was completed, the captured images were first corrected to remove blurring caused by the railcar vibration, using the track's electric cables as a standard baseline, then followed by the image mosaicking based on the characteristic points and noise reduction through the horizontal and vertical projection. Furthermore, taking the existence of variations in the luminance gradient along line edges into consideration, cracks with more detailed luminous variation were selected. A hysteresis threshold-processing method was then employed to select only edges joined to edges detected by high threshold values, followed by the measurement of extracted cracks including width, length, and direction. To improve the detection rate of cracks, the author emphasized the importance of removing the distractions of concrete joints, cables and cable shadows in the preprocessing stage, which is very useful for the complex tunnel environment. However, the author focused on the minute cracks (0.5 mm width) for the extraction and measurement of cracks, therefore the applicability under complex crack regions and spalling need to be studied further.

Qi et al. (2014) proposed an automatic algorithm to detect the cracks of subway tunnel based on the IP. First, the tunnel surface images were obtained using nine linear CCD cameras covering the whole surface with neighboring overlap areas, and lasers were employed to offer even illumination, as shown in Figure 2.11. A controller was used to synchronize these cameras however no more details were mentioned, and the collected images of each camera were stored in a server equipped with Redundant Arrays of Independent Disks (RAID) to avoid the loss of data. Second, the acquired images were processed by histogram Tula stretching, median filter, and top-hat transform to enhance the contrast and remove the noise, followed by the proposed block binarization using the average intensity value of the square adjacent pixels as the threshold, which can better distinguish the crack from the background and reduce the interference of other items such as cables and pipes. After the segmentation, the connected regions for which area was lower than the pre-defined value were removed. Although the algorithm was simple and easily implemented and had good performance on crack identification in complex tunnel environment, the threshold during the process of binarization and noise removing was selected by many attempts, and this selection cannot adapt to the characteristics of images by itself. Therefore, the author suggested that the means of machine learning can be used to achieve the automatic threshold selecting.

Figure 2.11: Image acquisition system including laser source and CCD camera (Qi et al., 2014).

Zhang et al. (2014) presented an automatic crack detection and classification method to monitor the safety status of subway tunnel. The images of tunnel surface were acquired by high-speed complementary metal-oxide-semiconductor (CMOS) line scan cameras covering the whole surface of lining. After the acquisition, the images were stitched together and then smoothed with an averaging filter to reduce the noise. Considering that the crack regions with low intensity values are darker than their surroundings in gray-scale images, a black top-hat transformation was utilized to detect the local dim regions. Subsequently, the image segmentation was achieved by a thresholding operation, followed by the area opening operation to eliminate the irrelevant connected regions. For the crack measurement, the length was calculated as the sum of line segments along the crack skeleton, while the width was regarded as the number of the pixels in the transversal direction of the skeleton. The proposed approach was effective for crack detection, but the detection rate and accuracy can be improved further. The optimized parameter settings in segmentation may need to be adjusted in other applications.

Shen et al. (2015) proposed an automatic crack detection method based on a wireless multimedia sensor network for subway tunnels. This system consisted of a vehicular wireless multimedia sensor node, a station sink node, a transmission module, and a central server. The sensor node installed on the train, mainly comprising a CCD camera, a storage module, and a high-speed processor, was used to collect, store, binarize, and compress images. When the train arrived at a station, the compressed image data was transmitted to a sink node, followed by moving the data to a central server. The received data was then processed by a new crack recognition algorithm. Furthermore, the images were processed by median filtering, high cap transformation, and OTSU threshold segmentation, as shown in Figure 2.12. Thus, the crack area was calculated by the area of connected regions, the length was the sum of all the skeleton white pixels, and the average width was obtained by the ratio of area to length. Although the method had good performance, some weakness still existed in the proposed system. For example, the limited bandwidth of sensor network was difficult to transmit a great deal of image data in a short time, and by using binary images for fast transmission and crack identification, the original image was lost and need to be searched in sensors. Also, the authors did not mention the synchronization of cameras while collecting the data.

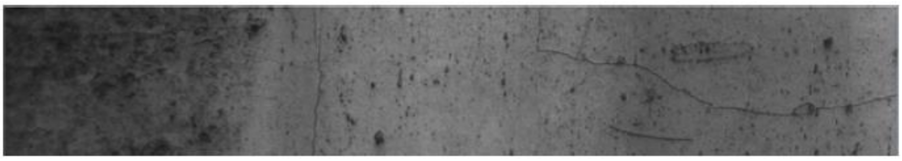

(a) Original image

(b) Crack identification

Figure 2.12: Results of image processing (Shen et al., 2015).

Huang et al. (2017) developed a subway tunnel inspection equipment MTI-100 which consisted of image acquisition system based on the line-scan CCD cameras, control system, and moving control system, to capture the stable images of lining surface, as shown in Figure 2.13. This equipment could be assembled and disassembled with 5 min and 3 min respectively, time-saving for the actual inspection in the limited time. To reduce the influence of vibration caused by the moving equipment, the max image shift was controlled to be less than 0.03 mm. For the crack recognition, the acquired images were divided into local image elements with the background grid and crack grid. The brightness difference and contrast difference were calculated using the pixel grayscale values, then an index ranging from 0 to 1 was defined by the product of two difference factors. The lower the index is, the greater the possibility that the center pixel is the seed point. Once all the points determined by a threshold value were found, the crack was recognized as the connected line of the seed points, and the crack length and average width were calculated. The proposed non-destructive detection equipment had about 87% accuracy in the simulative tunnel tests and about 85% in the actual tunnel for crack inspection. It should be noted that the cracks were missing when the width was below 0.3 mm in the tests.

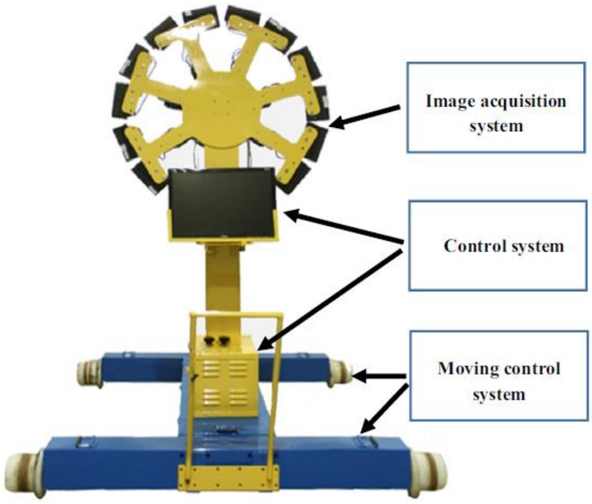

Figure 2.13: Tunnel inspection system (Huang et al., 2017).

2.5 Damage level of tunnels

To quantify the level of tunnel damage, a damage index could be used. In the past, several damage indexes or damage levels were proposed with quantitative (Argyroudis and Pitilakis, 2012; Fabozzi et al., 2017; Andreotti and Lai, 2019) and qualitative methods (Huang et al., 1999; ALA, 2001; HAZUS, 2004; Corigliano et al., 2007). Quantitative damage indexes were traditionally determined by the demand-capacity ratios of structural response parameters such as bending moment and displacement by using numerical approach. Argyroudis and Pitilakis (2012) defined the damage index as the ratio between the actual and capacity bending moment of the tunnel cross section, which is the simplified method used by many studies (Argyroudis et al., 2017; Huang et al., 2017; de Silva et al., 2021; Huang et al., 2022). The actual bending moment was computed considering the combination of static and seismic loading at the time step when the maximum ovaling deformation of tunnel structure occurred. The capacity bending moment was calculated on the basis of material and geometry properties of tunnel lining considering the induced axial forces and bending moments. Fabozzi et al. (2017) expressed the damage index as the ratio between the permanent rotation and reference thresholds for the segmental tunnel lining. Andreotti and Lai (2019) considered the non-linear dynamic response of the tunnel lining, and selected the relative displacement between the crown of arch and the inverted arch normalized by the equivalent diameter of the tunnel lining cross-section. This quantity was also related to numerical description, qualitative description, and functionality. Alternatively, qualitative methods in the literature described the performance of tunnel lining according to the visual signs of distress, such as cracking, spalling and crushing of concrete, and bending and buckling of reinforcing bars, from past earthquakes. In the database, structural damages were collected considering the different types of underground structures, different types of tunnel support, different soil conditions, and various ground motions. Overall, the above damage indexes or damage levels were proposed based on the response of tunnels following an earthquake, and their performance in the literature indicated the obvious differences (Argyroudis and Pitilakis, 2012; de Silva et al., 2021). Also, the seismically-induced ground failure was not included in the previous studies. It therefore is necessary to further investigate the damage index of tunnels under earthquakes.

2.6 Conclusion

In the first section, according to the observation of damage from past earthquakes, damage in underground structures can be induced by two phenomena: ground shaking and ground failure. The lining cracks are the predominant damage type. Although many experimental and numerical studies focused on the behaviour of tunnels under single earthquakes or under seismic excitations with increasing intensities, the cumulative effect of multiple seismic events is not well-understood within an earthquake prone region. Therefore, it is necessary to further investigate the impact of this cumulative effect on the tunnel integrity.

In the second section, four derived similitude rules, used in previous 1 g shaking table tests of underground structures, including elastic-gravity similarity law, elastic similarity law (gravity distortion method), artificial mass method, and general similarity law (less artificial mass method), and their application on the tunnel damage tests are described. Their limitation is that using existing similitude rules to simulate the tunnel lining cannot guarantee the similitude of the structural nonlinear behaviour. Therefore, it is necessary to explore more accurate similarity relations. Also, the quantitative analysis of lining cracks (e.g. average width, length and area) and ground deformations (e.g. volume) need to be further explored.

In the third section, four main approaches used to measure surface elevation changes between multi-temporal point cloud datasets, are reviewed including DoD, C2C, C2M and M3C2. The advantage of M3C2 is highlighted. Following the elevation change detections, the estimation of surface volumetric changes is reviewed through the recent studies including laboratory experiments and field measurements. Based on the wide application of M3C2 algorithm on soil erosion, landslides and rockfalls, it is worthy attempting 3D point clouds to detect the seismically-induced ground deformations in two equivalent free-field and soil-tunnel systems exposed to earthquake shaking simultaneously.

In the fourth section, previous crack monitoring systems of tunnels, which mainly consists of camera, light source, power, storage and control device, and the corresponding image processing techniques of tunnel cracks, which contains contrast enhancement, segmentation and morphological operations and so on, are presented. Due to the low and uneven lighting, serious noise, and background interference of tunnel environment, acquisition systems need to be individually designed to capture the high-quality image data, and the crack identification and measurement need to be realized with suitable methods. In order to detect the evolution of tunnel damages during the 1 g shaking table tests, a new cracking monitoring system will be proposed.

In the final section, previous damage indexes or levels used to quantify the level of tunnel damage are reviewed. Quantitative damage indexes were traditionally determined by the demand-capacity ratios of structural response parameters such as bending moment and displacement by using numerical approach. Qualitative methods in the literature described the performance of tunnel lining according to the visual signs of distress, such as cracking, spalling and crushing of concrete, and bending and buckling of reinforcing bars, from past earthquakes. Both are proposed based on the response of tunnels following an earthquake, and their performance in the literature indicate the obvious differences. Also, the seismically-induced ground failure was not included in the previous studies. It therefore is necessary to further investigate the damage index of tunnels under earthquakes.

Chapter 3 Shaking table test program

3.1 Introduction

Shaking table tests, as an advanced method, provide an excellent opportunity to study how the cumulative effect of multiple earthquakes affects tunnel integrity, and afford the ability to do so under varied controlled conditions. Also, in order to better assess the influence of the tunnel presence on the soil response, two model boxes are employed simultaneously during each shaking, one with the tunnel and the other without the tunnel. This chapter provides a description of preparation and operation of shaking table model tests, and is organized as follows. Firstly, the main technical parameters of the shaking table are introduced. Secondly, the geometry of the two model boxes and the corresponding boundary conditions are presented. Thirdly, a new set of scaling laws used to simulate the cracking process of lining and the derived similarity ratios are described. Also, material tests of microconcrete and steel wire reinforcement, and the fabrication of the model tunnel are presented. Furthermore, material tests of sand and the placement of surrounding ground are introduced. In addition, technical parameters of different sensors and their installation methods are discussed. Finally, the test input signals and the loading sequence are explained.

3.2 Shaking table facility

The shaking table tests were performed on the new earthquake simulator at National Engineering Laboratory for Technology of Geological Disaster Prevention in Land Transportation (NEDL) at Southwest Jiaotong University, China. The shaking table mainly consists of the following components: steel table, actuators, reaction foundation, static equilibrium support and shutdown support, as shown in Figure 3.1. The size of testing platform is 10 m × 8 m and the maximum load capacity is 160 t. This shaking table can provide six controlled degrees of freedom, thus allowing for two- and three-dimensional input motions, and is driven by hydraulic actuators equipped with servo-valves at the frequency band 0.1-50 Hz. The MTS control system allows the table to run under acceleration, velocity, and displacement control, but it limits the accelerations to 1.2 g in horizontal direction and 1.0 g in vertical direction. The specification of the shaking table is given in Table 3.1.

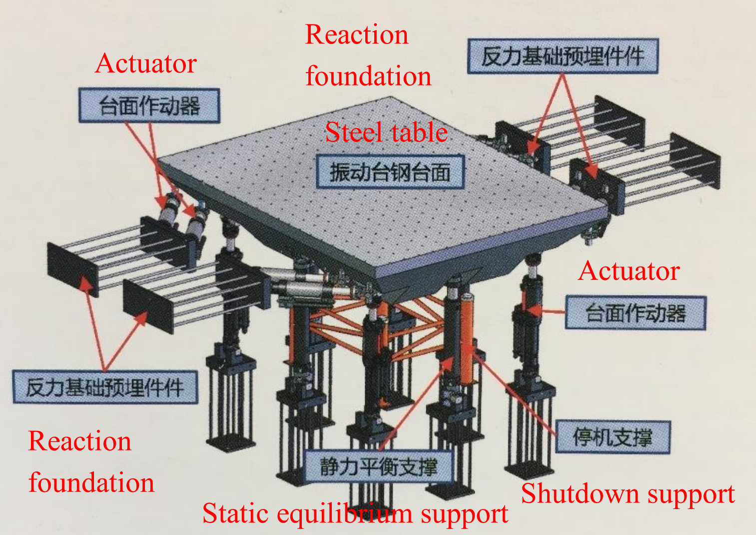

Figure 3.1: Shaking table layout.

Table 3.1 Main technical parameters of shaking table.

Technical indicators	Parameters
Table size (m×m)	8.0×10.0
Frequency range (Hz)	0.1-50
Degree of freedom	Six
Maximum weight (t)	160
Maximum displacement (mm)	Horizontal direction: ±800, Vertical direction: ±400
Maximum velocity (mm/s)	Horizontal direction: ±1200, Vertical direction: ±1000
Maximum acceleration (g)	Horizontal direction: 1.2, Vertical direction: 1.0
Maximum overturning moment (kN·m)	6000

3.3 Model boxes and boundary conditions

Two rigid model boxes were used for the soil-tunnel and free-field tests respectively, both with the dimension 2.5 m length, 2.5 m width, and 2.0 m height, as shown in Figure 3.2. In order to guarantee the stability of model boxes during the shaking, two model boxes were firmly bolted on the steel platform of shaking table with high shearing strength bolts and each bolt was checked by torque wrench. EPS geofoams with thickness of 15 cm as absorbing boundaries were placed on the inner sides of containers to reduce the reflections and refractions of seismic waves during the tests, as shown in Figure 3.3(a). It is a low stiffness and lightweight material, and has been used in previous shaking table model tests (Sun et al., 2011; Wang et al., 2015; Xin et al., 2019; Han et al; 2020). Through the above measures, the tunnel model was allowed to deform under the seismic loadings without much interference from the boundary regions. In this study, the properties of EPS geofoam were density 20 kg/m^3, elastic modulus 0.3 MPa and Poisson's ratio 0.35. Moreover, a layer of gravel with thickness of 30 mm was glued at the bottom of the model boxes to increase the friction between ground and model container (Figure 3.3(b)). Over the course of multiple earthquake shakings, two model boxes filled with models were vibrated simultaneously in a single horizontal direction perpendicular to the tunnel axis, as shown in Figure 3.4.

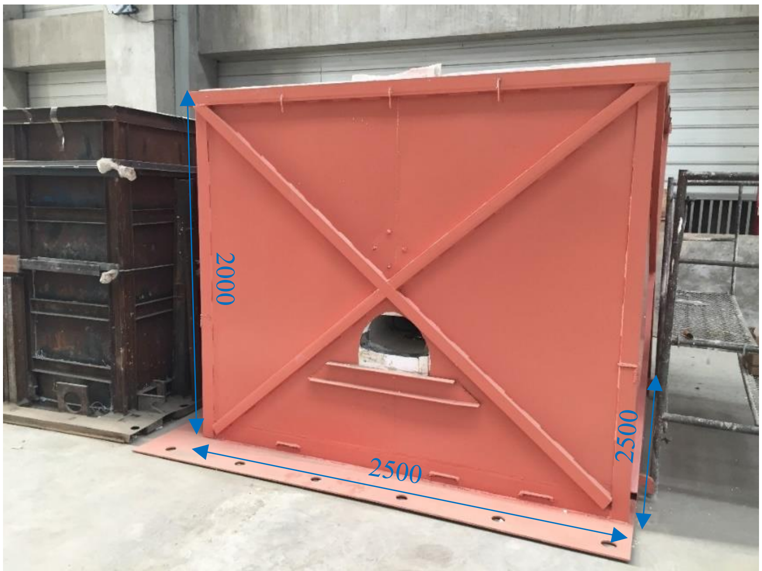

(a) Model box 1 (for soil-tunnel model)

(b) Model box 2 (for free-field model)

Figure 3.2: Geometry of two model boxes (Unit: mm).

(a) EPS geofoam

(b) Gravel

Figure 3.3: Inside of two model boxes.

Figure 3.4: Overview of shaking table tests.

3.4 Similarity relations

In order to accurately simulate the seismic behaviour of tunnel lining in model scale, the similarity relations between the model and prototype need to be defined. Traditionally, based on the Buckingham-π theorem, dimensional analysis was adopted to determine the similarity relations of physical parameters in the test program (Meymand, 1998). Similarity ratios of three fundamental factors, e.g. length (S_L), density (S_ρ), and elastic modulus (S_E) were selected, followed by deriving the similarity ratios of other factors. Obtained similarity relations cannot guarantee the similitude of structural nonlinear behaviour, like some previous experiments (Sun et al. 2011; Wang et al. 2015; Meng et al. 2016; Xin et al. 2019) investigating the development of seismically-induced cracks (nonlinear behaviour) on tunnel linings. Recently, Antoniou et al. (2020), extending previous endeavours, proposed a new set of scaling laws to study the post-cracking behaviour of reinforced concrete tunnel linings during 1g shaking table tests. The proposed scaling laws were numerically examined under three boundary conditions (i.e. a rigid box, a laminar box and a very wide model) with two seismic actions (i.e. Kobe earthquake in 1995 and Wenchuan earthquake in 2008). The results indicated a good similitude between model (1:30 scale) and prototype performance such as the time histories of mean tensile damage over the tunnel and crack pattern of linings. For the proposed post-cracking similarity relations, two dimensionless parameters s and N_P were used. Stress brittleness number s governs the fracturing phenomenon of brittle unreinforced concrete elements and it is defined by (Carpinteri, 1982; Corrado et al., 2011),

$$s = \frac{K_{IC}}{\sigma_u h^{1/2}} \tag{3.1}$$

Where K_{IC} is the material fracture toughness, σ_u is its ultimate tensile strength of concrete, and h is a characteristic linear size of the specimen.

The dimensionless number N_P applies to lightly reinforced concrete elements and it plays a primary role for the stability of the process of concrete fracture and steel plastic flow (Carpinteri, 1984; Corrado et al., 2011). It is given by the following equation,

$$N_P = \rho_t \frac{\sigma_y h^{1/2}}{K_{IC}} \tag{3.2}$$

Where ρ_t and σ_y are the percentage and the yielding strength of steel reinforcement respectively.

Based on equations (3.1) and (3.2), similarity scales of s and N_P are:

$$S_s = \frac{s_m}{s_P} = \frac{K_{ICm}/(\sigma_{um} t_m^{1/2})}{K_{ICP}/(\sigma_{uP} t_P^{1/2})} = \frac{K_{ICm}}{K_{ICP}} \frac{\sigma_{uP}}{\sigma_{um}} \sqrt{\frac{t_P}{t_m}} = 1 \tag{3.3}$$

$$S_{N_P} = \frac{N_{Pm}}{N_{P_P}} = \frac{\rho_{tm}\sigma_{ym} t_m^{1/2}/K_{ICm}}{\rho_{tP}\sigma_{yP} t_P^{1/2}/K_{ICP}} = \frac{\rho_{tm}}{\rho_{tP}} \frac{K_{ICP}}{K_{ICm}} \frac{\sigma_{ym}}{\sigma_{yP}} \sqrt{\frac{t_m}{t_p}} = 1 \tag{3.4}$$

where the subscripts m and P denote properties of the model and of the prototype respectively.

Based on equations (3.3) and (3.4),

$$\frac{\sigma_{um}}{\sigma_{uP}} \sqrt{\frac{h_m}{h_P}} = \frac{\rho_{tm}}{\rho_{tP}} \frac{\sigma_{ym}}{\sigma_{yP}} \sqrt{\frac{h_m}{h_P}} \tag{3.5}$$

Then,

$$\frac{\sigma_{um}}{\sigma_{uP}} = \frac{\rho_{tm}}{\rho_{tP}} \frac{\sigma_{ym}}{\sigma_{yP}} \tag{3.6}$$

Namely,

$$S_{\sigma_u} = S_{\sigma_y} S_{\rho_t} \tag{3.7}$$

Where S_{σ_u}, S_{σ_y}, and S_{ρ_t} are the similarity ratios of ultimate tensile strength of concrete, yielding strength of steel reinforcement, and percentage of steel reinforcement respectively.

Equation (3.7) shows the internal relations among the concrete tensile strength, reinforcement yield strength and reinforcement percentage, thus the model material can be selected according to this equation. The reinforcement focused similarity relations are expected to play a primary role in the seismic behaviour of overall structures during the cracking stage. In this study, the elastic similarity relations derived by the Buckingham-π theorem and the equation (3.7) proposed by Antoniou et al (2020) are combined together to investigate the seismic response of tunnel structures with 1 g shaking table tests, as shown in Table 3.2. This is the first use of relationship (3.7) to faithfully simulate the cracking of tunnel lining. As for the design of soil, it will be described in Section 3.6.

Table 3.2 Scaling laws adopted for tunnel in shaking table test.

Physical quantity	Unit	Similarity relation	Similarity ratio (model/prototype)
Length	$L{:}\,m$	S_L	1/30
Density	$\rho{:}\,t/m^3$	S_ρ	1/1.5
Elastic Modulus	$E{:}\,Mpa$	$S_E = S_L S_\rho$	1/45
Strain	ε	$S_\varepsilon = 1$	1
Stress	$\sigma{:}\,MPa$	$S_\sigma = S_L S_\rho$	1/45
Poisson's ratio	υ	$S_\upsilon = 1$	1
Time	$T{:}\,s$	$S_T = S_L^{0.5}$	1/5.5
Acceleration	$a{:}\,m/s^2$	S_a	1
Displacement	$u{:}\,m$	$S_u = S_L$	1/30
Velocity	$V{:}\,m/s$	$S_V = S_L^{0.5}$	1/5.5
Friction angle	$\varphi{:}\,°$	$S_\varphi = 1$	1
Cohesive strength	$c{:}\,kPa$	$S_c = S_E$	1/45
New relationship		$S_{\sigma_u} = S_{\sigma_y} S_{\rho_t}$	

Note: Friction angle and cohesive strength are not scaled directly.

3.5 Model tunnel

A real tunnel in China is used as the prototype in this study. The Lebuguo tunnel is a highway tunnel connecting the towns of Mianning and Chengxiang, located in a highly earthquake-prone area. It has a horseshoe shape with excavated dimensions of 12.64 m width and 10.14 m height. The thickness of primary lining and secondary lining are 24 cm and 45 cm respectively. In the model tunnel, the thickness of primary lining is converted to that of secondary lining following the equivalence principle of transverse bending stiffness. Thus, the thickness of the model lining is 2 cm. Figure 3.5 shows the cross section of the model tunnel according to the length similarity ratio. The marked vibration direction is normal to the tunnel axis because this study focuses on the ovaling/racking deformation mode of the tunnel.

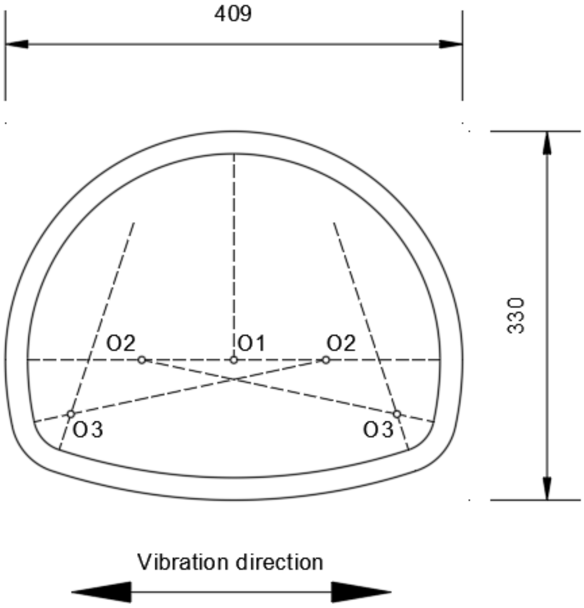

Figure 3.5: Cross section of model tunnel (Unit: mm).

3.5.1 Model concrete

According to the similarity relations in Table 3.2, the properties of tunnel lining in the prototype and model are listed in Table 3.3. Typical values of a Class 25/30 concrete are used in the prototype tunnel. As previously presented, microconcrete has similar stress-strain properties to the concrete, and thus is adopted to simulate the model lining in this study. Microconcrete is a mix of cement, coarse sand, fine sand and water;

cement is the binding material to bind the ingredients due to hydration reaction, and sand of different sizes is analogous to the aggregates of concrete. Before casting the model lining, the mix proportion of microconcrete needs to be determined based on the laboratory tests of specimens. In the following sections, the uniaxial compression tests of cubic specimens and of prismatic specimens, and four-point bending tests of prismatic specimens are conducted to find the appropriate mix proportion of microconcrete. The testing methods refer to the standard of concrete and mortar.

Table 3.3 Concrete lining properties in prototype and scaled model.

Properties	Prototype tunnel	Scaled tunnel
Elastic modulus (E: MPa)	29700	660
Density (ρ: t/m^3)	2.5	1.67
Compressive strength (f_c: MPa)	30.15	0.67
Tensile strength (f_t: MPa)	3.015	0.067
Poisson's ratio	0.2	0.2

3.5.1.1 Uniaxial compression tests

The weight ratio of microconcrete was cement (P.C 32.5R), slaked lime ($Ca(OH)_2$), river sand (≤ 5 mm), and water with 0.8: 0.8: 6: 2.4. Slaked lime was mainly used to soften microconcrete to decrease the elastic modulus. In order to guarantee the good grading of aggregates, dry river sand was sieved to remove the coarse aggregates. Model properties of microconcrete specimens were listed in Table 3.4, closed to the theoretical values in Table 3.3. Cubic compressive strength was 0.63 MPa measured with the specimens of 70.7 mm × 70.7 mm × 70.7 mm according to the standard JGJ/T70-2009 (MOHURD, 2009), as shown in Figure 3.6. It could be observed that cyclo-hoop effect was obvious in the cubic specimens, which resulted from the constrain to the transverse expansion of specimen by the friction between the pressure plate and the compressed surface of specimen. This was a typical damage phenomenon of concrete cubic specimens, indicating that the properties of microconcrete were similar to that of concrete. In addition, based on the standard GB/T 50081-2002 (MOC and GAQSIQ, 2002), loading rate of concrete below C30 grade is 0.3-0.5 MPa/s, therefore the median is 0.4 MPa/s. The loading rate of microconcrete can refer to that of concrete and be calculated as follows:

$$\Delta\sigma_{mic} = \Delta\sigma \times S_E = \frac{0.4}{45} = 0.0089\ MPa/s \tag{3.8}$$

$$\Delta F_{mic} = \Delta\sigma_{mic} \times A = 0.0089 \times 70.7 \times 70.7 = 44\ N/s \approx 40N/s \tag{3.9}$$

Where $\Delta\sigma_{mic}$ is the stress increment for microconcrete, $\Delta\sigma$ is the stress increment for concrete, S_E is the similarity ratio of elastic modulus, ΔF_{mic} is the force increment for microconcrete, and A is the bearing area of specimens.

Table 3.4 Model properties of microconcrete specimens.

Cubic compressive strength (MPa)	Axial compressive strength (MPa)	Elastic modulus (MPa)	Density (g/cm^3)
0.63	0.51	730	1.77

Figure 3.6: Damaged cubic specimen in uniaxial compression tests.

According to the standard GB/T 50081-2002 (MOC and GAQSIQ, 2002), axial compressive strength and elastic modulus were 0.51 MPa and 730 MPa respectively measured with the specimens of 100 mm × 100 mm × 300 mm, as shown in Figure 3.7. It could be observed that shear failure occurred to the specimens, similar to the damage phenomena of concrete. In the prismatic specimens, the axial deflection was recorded from the strain gauges which were installed on the two opposite sides of the specimens. Then, the typical stress-strain curve of microconcrete was generated, as shown in Figure 3.8. It was found that at initial stage, there was an approximately linear relationship between the stress and strain. Elastic modulus was calculated from the middle segment of this stage (about 20 % - 30 % peak stress). With the increasing of stress, the slope of curve gradually decreased and finally tended to be zero at the maximum stress. Due to the limitation of testing machine, the descending section of the stress-strain curve cannot be obtained. Overall, above mentioned mix proportion could be used to obtain the required microconcrete properties within the reasonable deviations. Also, microconcrete demonstrated the similar damage phenomena and stress-strain properties, compared to that of concrete.

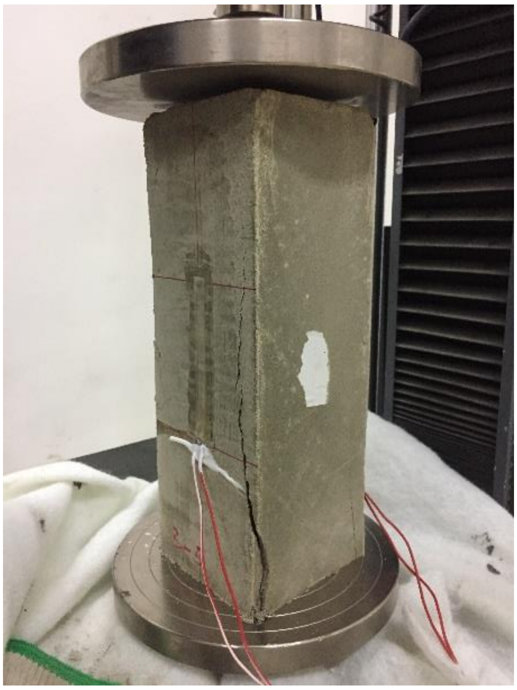

Figure 3.7: Damaged prismatic specimen in uniaxial compression tests.

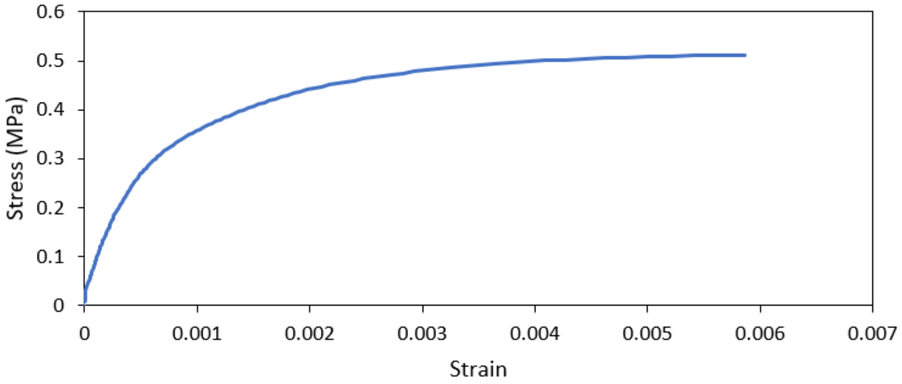

Figure 3.8: Typical stress-strain curves for prismatic specimen.

3.5.1.2 Four-point bending tests

Generally, tensile strength of concrete is only 10 % of its compressive strength. The mix proportions of concrete thus are mainly determined based on the compressive strength. In this study, microconcrete was adopted to simulate the tunnel lining and except for its compressive strength, tensile strength was investigated. Considering the actual conditions of laboratory, it was difficult to measure the strength in direct tensile tests, thus four-point bending tests were performed. According to the standard GB/T 50081-2002 (MOC and GAQSIQ, 2002), flexural tensile strength was 0.249 MPa measured with the specimens of 100 mm × 100 mm × 400 mm, as shown in Figure 3.9 and Figure 3.10. It was larger than the direct tensile strength 0.067 MPa because of the stress distribution in relation to the distance from the neutral axis, rather than the uniform distribution in the uniaxial tensile tests. Moreover, it could be observed that the fracture occurred at the middle 1/3 section of the specimen, similar to the damage phenomenon of concrete. The crack developed from the bottom to the top of specimen. While reaching the coarse aggregate, the crack progressed along the interface between the aggregate and mortar. In addition, there was an approximately linear relationship between the load and displacement as shown in Figure 3.11, indicating when subjected to bending, microconcrete had the brittleness property which is similar to concrete. Thus, in practical, reinforcements need to be used to withstand the tensile forces and control the development of cracks. It should be noted that there was a fluctuation at the initial stage of load-displacement curve, which might be caused by the tiny gap between the top surface of specimen and the bearing surface of testing machine.

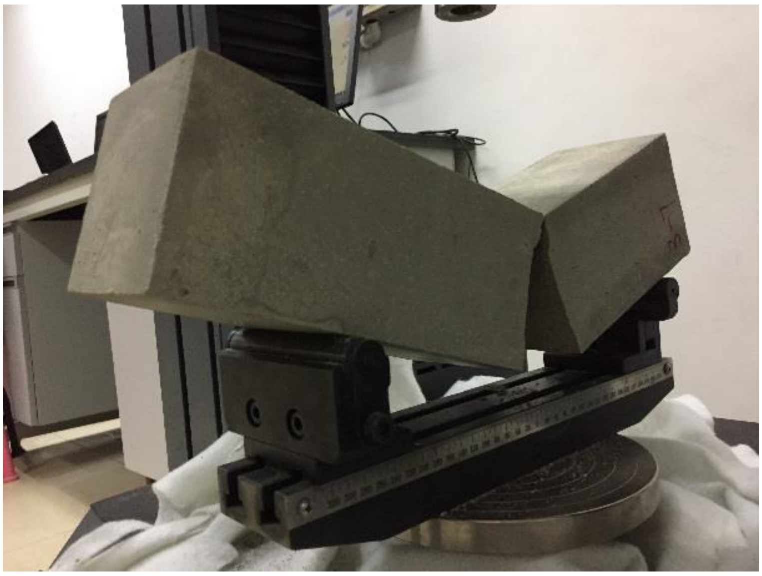

Figure 3.9: Damaged prismatic specimen in four-point bending tests.

Figure 3.10: Fracture section of damaged prismatic specimen in four-point bending tests.

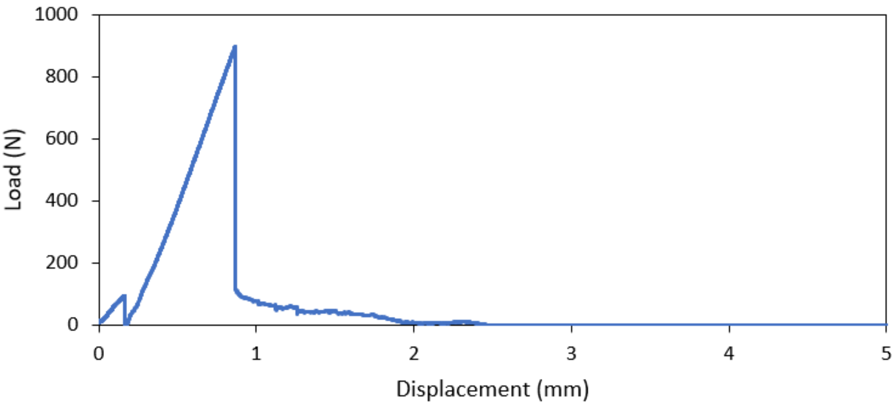

Figure 3.11: Typical load-displacement curve in four-point bending tests.

3.5.2 Model reinforcement

The properties of the steel reinforcement in prototype and scaled model tunnel are listed in Table 3.5. To simplify the model, tunnel is assumed with one array of rebars in the middle of lining. In the prototype, concrete lining is lightly reinforced with reinforcement ratio 0.169 % and steel bars with diameter 22 mm are spaced at 0.5 m along the tunnel longitudinal axis. In the model, the steel wire with diameter 0.2 mm is used to simulate the reinforcement. The corresponding reinforcement ratio could be calculated based on the previously mentioned new similarity relationship equation (3-7), followed by the computation of rebar spacing with the following equation,

$$\rho_{t_m} = \frac{\pi\left(\frac{d_m}{2}\right)^2 \frac{1}{S_{Pa_m}}}{t_m} \tag{3.10}$$

Where ρ_{t_m} is the reinforcement ratio of model tunnel, d_m is the diameter of model rebars, S_{Pa_m} is the spacing of model rebars, and t_m is the thickness of model tunnel.

In Table 3.5, it could be observed that the elastic modulus, density, geometry, and yield strength of steel wire do not meet the elastic similarity relations of Table 3.2. This difference is caused by following the equation (3.7) which is adopted to guarantee the similitude in post-cracking phase. Equation (3.7) denotes the internal relations among the concrete tensile strength, reinforcement yield strength and reinforcement percentage, thus the selection of model material is more flexible compared to the traditional elastic similarity relations.

Table 3.5 Steel reinforcement properties in prototype and scaled model.

Properties	Prototype tunnel	Scaled tunnel	Actual ratio (model/prototype)
Elastic modulus (E: MPa)	200000	179250	1/1.115
Density (ρ: t/m^3)	7.85	7.85	1/1
Poisson's ratio (μ)	0.20	0.20	1/1
Diameter (d_P: m)	0.022	0.0002	1/110
Spacing (S_{Pa}: m)	0.50	0.05	1/10
Reinforcement ratio (ρ_t: %)	0.169	0.00419	1/40.3
Steel yield strength (f_y: MPa)	400	359	1/1.115

In this study, 316 stainless steel wire with diameter 0.2 mm was selected as the model material and its strength and elongation were measured by tensile tests according to the standard GB/T 228.1-2010 (GAQSIQ and SA, 2010), as shown in Figure 3.12. The parallel length was 100 mm and the loading rate 12 mm/min. Model properties of 316 stainless steel wire were listed in Table 3.6, closed to the theoretical values in Table 3.5. The tensile strength was 705 MPa, and the percentage elongation was 66.20%. In the standard, if there is not yield plateau in stress-strain curves of metallic materials, $R_{p0.2}$, which is the stress when the plastic elongation is 0.2%, represents the plastic extension strength. Therefore, the stress-elongation curves of steel wire were printed in coordinate grids to quickly find the yield strength 323.33 MPa which was the average of three tests. It could be observed that when the tensile force was applied to a mild steel wire, it had some elongation. When the force was small enough, there was an approximately liner relationship between the stress and elongation. With the increasing of the stress, the steel wire experienced the non-linear elastic stage and then reached the yield point. Beyond the yield strength, the plastic deformation of steel wire increased rapidly until reaching the tensile strength. Overall, the properties of steel wire were similar to that of steel bar and it could be used to simulate the reinforcement.

Figure 3.12: Tensile tests of 316 stainless steel wire.

Table 3.6 Model properties of 316 stainless steel wire.

Diameter (mm)	Density (t/m^3)	Yield strength (MPa)	Tensile strength (MPa)	Percentage elongation
0.2	7.85	323.33	704.78	66.20%

Note: Loading rate is 0.002 * 100 * 60 = 12 mm/min.

3.5.3 Construction of model tunnel

Once the mix proportion of microconcrete and type of steel wire were determined, the model tunnel could be constructed by the following steps. Firstly, steel wire meshes with spacing 5 cm were manually produced using the wooden frame by connecting the lengthwise steel wire and crosswise steel wire at right angles with the bamboo shuttle, as shown in Figure 3.13. Lengthwise steel wire was first tied to the iron nails, and crosswise wire then passed over and knotted with lengthwise one. To keep the regular grid, the control baseline was employed, as shown in Figure 3.14. It took 2 days to complete a steel wire mesh of 1.5 m × 0.6 m.

Secondly, two wooden rings were prepared according to the dimension of tunnel cross section. Holes were drilled with spacing of 5 cm on rings for the assembling of handmade steel wire mesh, as shown in Figure 3.15. The thickness of internal and external aluminum plate mould was 1.5 mm and 0.8 mm respectively, as shown in Figure 3.16. To prevent concrete bulging, the internal mould was braced by sand, while the external mould was strengthened by iron hoops. Also, adhesive tape was installed on the outer surface of internal mould and inner surface of external mould along the lining longitudinal axis, which could be convenient for demoulding and guarantee the smoothness of lining surface.

Thirdly, the lining was poured in the moulds through the reserved grooves on the wooden rings. In the pouring process, slight vibration on the outer surface of external mould could increase the uniformity and compactness of micconcrete. The moulds were removed after 5 days, and the tunnel lining can be used for shaking table tests after 28 days' curing. Each lining had a thickness of 2 cm and a length of 58 cm.

Finally, four lining sections were connected and installed in the soil-tunnel model box. In the connection process, lining sections were placed on the wooden frame and the sponge between the lining and frame was used to protect the lining. After the alignment of lining sections, they were adhesively connected as shown in Figure 3.17(a), and then the joints were covered by the rubber plate for which the width was 15 cm as shown in Figure 3.17(b). In the installation process, model tunnel was moved into the model box by the crane, see Figure 3.17(c). Once the lining was aligned with the two reserved openings on the model box, asphalt tape was used to seal the gap at the two ends, as shown in Figure 3.17(d).

Figure 3.13: Steel wire mesh.

Figure 3.14: Control baseline.

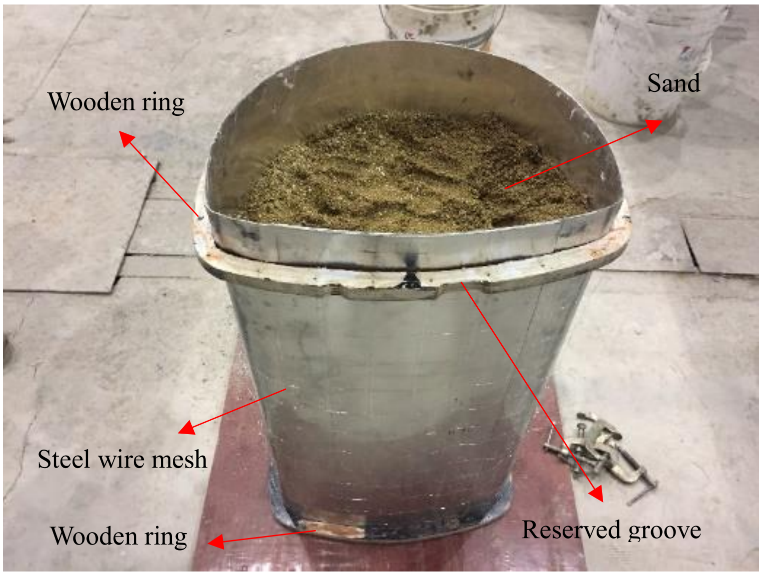

Figure 3.15: Installation of steel wire mesh.

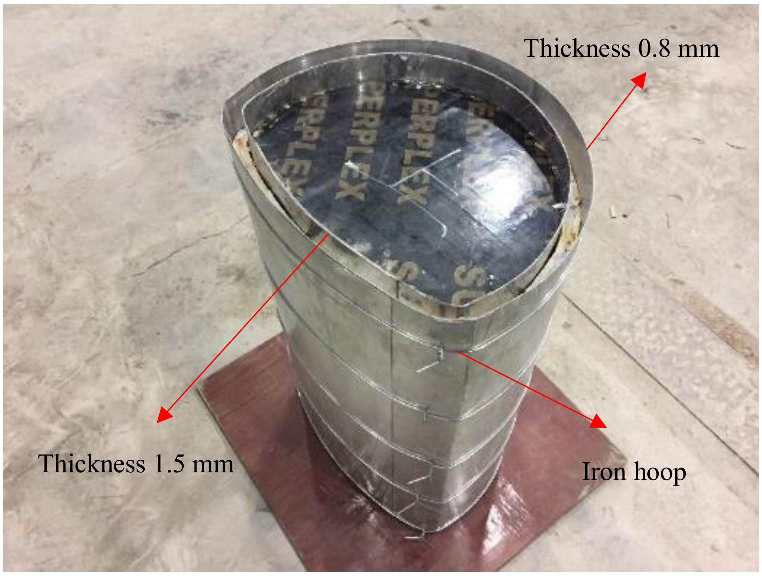

Figure 3.16: Mould for pouring.

(a) Connection

(b) Rubber plate

(c) Hoisting

(d) Placement

Figure 3.17: Connection and installation of tunnel model lining.

3.6 Model soil

Dry sand has been used to simulate the surrounding soil in the previous shaking table tests of tunnels (Huang et al., 2019; Han et al., 2020; Zhang et al., 2020; Yuan et al; 2020; Xu et al., 2021; Yang et al., 2021), mainly for reducing the complexities of field ground geometry and the uncertainties of parameters. Therefore, the dry river sand in Sichuan province was adopted to model the ground surrounding the tunnel in this study. The sand properties were measured in the following sections by sieve analysis, compaction tests, funnel method, pycnometer tests and direct shear tests.

3.6.1 Sieve analysis

A dry sieve analysis was performed, following the standard GB/T 50123-2019 (MOHURD and AMR, 2019). The aperture size of 5 mm, 2.0 mm, 1.0 mm, 0.5 mm, 0.25 mm, and 0.075 mm were selected to describe the grain size distribution of sand, as shown in Figure 3.18. The coefficient of uniformity C_u and coefficient of curvature C_C are calculated by equations (3.11) and (3.12) respectively. This sand is classified as poorly graded sand.

$$C_u = \frac{d_{60}}{d_{10}} = \frac{0.38}{0.0855} = 4.44 \tag{3.11}$$

$$C_c = \frac{d_{30}^2}{d_{10} \cdot d_{60}} = \frac{0.188^2}{0.0855 \times 0.38} = 1.09 \tag{3.12}$$

Where d_{60} means that 60% of the grains are smaller than this size by weight, d_{30} 30% of the grains are smaller than this size by weight, and d_{10} 10% of the grains are smaller than this size by weight.

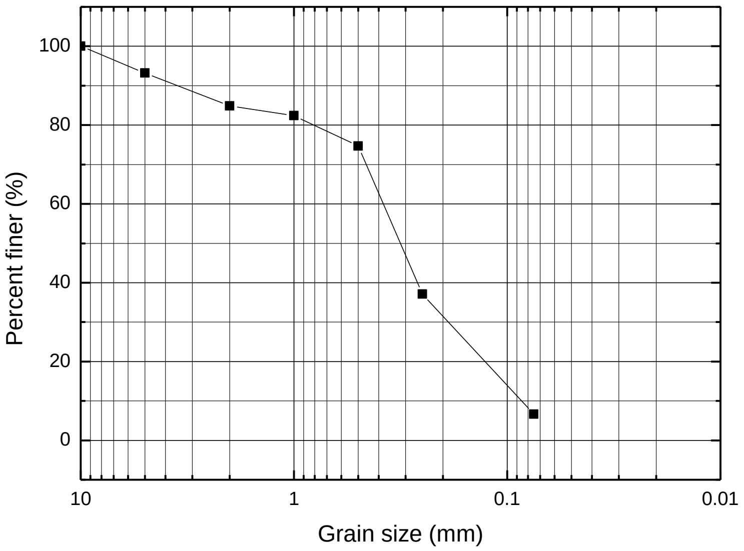

Figure 3.18: Grain size distribution of sand.

3.6.2 The maximum and minimum dry density

The minimum dry density of sand was measured by funnel method, as shown in Figure 3.19. Initially, 700 g of sand was placed in a 1000 ml glass graduated cylinder by funnel. Smooth the sand surface slightly and the volume of sand V_1 was measured on the graduated cylinder. With the top of the cylinder sealed, the sample was turned upside down, then steadily rotated back upright at a constant rate. The maximum volume V_2 was measured during the process of turning. Finally, the maximum value of V_1 and V_2 was determined, and the minimum dry density calculated by equation (3.13). The average value of two tests was 1.36 g/cm3, listed in Table 3.7.

$$\rho_{dmin} = \frac{m_d}{max\{V_1,V_2\}} \tag{3.13}$$

Where ρ_{dmin} is the minimum dry density, $\max\{V_1, V_2\}$ is the maximum volume of loose sand, and m_d is the weight of sample sand.

Figure 3.19: Funnel method.

Table 3.7 Dry density and specific gravity of sand.

Minimum dry density (g/cm3)	Maximum dry density (g/cm3)	Specific gravity
1.36	1.87	2.70

The maximum dry density of sand was obtained through compaction test, as shown in Figure 3.20. The sand compaction was carried out in three layers in mould (1000 ml), by using a rammer in the vertical direction and a fork in the horizontal direction simultaneously. Then the mass of the sand was measured and the maximum dry density calculated by equation (3.14). The average value of two tests was 1.87 g/cm3.

$$\rho_{dmax} = \frac{m_d}{V_{min}} \tag{3.14}$$

Where ρ_{dmax} is the maximum dry density, and V_{min} is the minimum volume of compacted sand.

Figure 3.20: Compaction test.

3.6.3 Specific gravity

The specific gravity of sand was measured by pycnometer method, as shown in Figure 3.21. First, the dry sand was placed in pycnometers (V=50 ml) and immersed in distilled water at room temperature. After immersion the entrapped air was removed from the sample by using vacuum saturation meter taking about 2 hours. Then add additional water to return the pycnometer to its calibrated capacity and determine the total weight of pycnometer, specimen, and water. The specific gravity was 2.70 calculated by the following equation,

$$G_s = \frac{m_d}{m_{bw}+m_d-m_{bws}} G_{wT} \tag{3.15}$$

Where m_{bw} is the weight of pycnometer and water, m_{bws} is the weight of pycnometer, specimen and water, and G_{wT} is the specific gravity of distilled water at T°C。

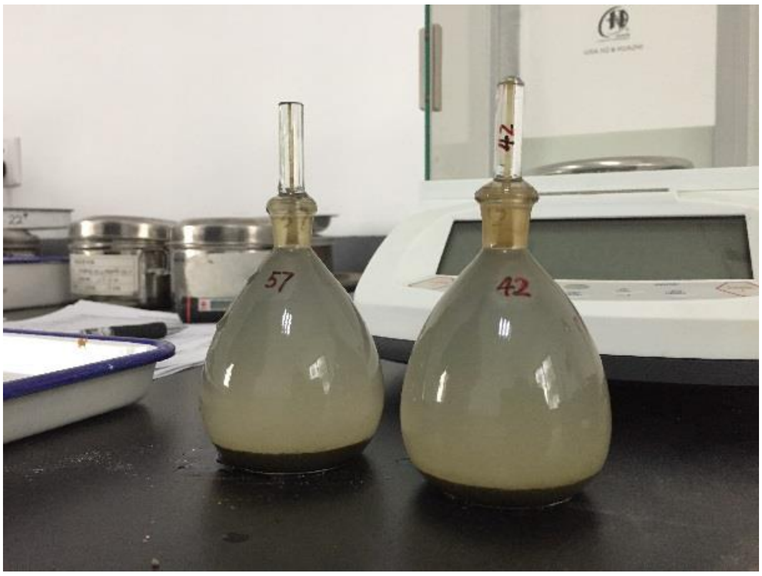

Figure 3.21: Pycnometer test.

3.6.4 Direct shear tests

Direct shear tests were used to determine the angle of internal friction and cohesion of loose/dense sand as shown in Figure 3.22. The density of loose and dense sand corresponded to the minimum and maximum dry density respectively. According to the standard GB/T 50123-2019 (MOHURD and AMR, 2019), shear stress-shear displacement curves, as shown in Figure 3.23 and Figure 3.24, were defined with different normal stresses (100, 200, 300 and 400 kPa) and peak shear stress was computed as the shear strength. For different soil density, there was a different behaviour in terms of shear stress-shear displacement curves. In case of dense sand, shear stress increased with the increase of shear displacement, however after reaching the peak stress, the shear stress decreased with further increase in the shear displacement. For loose sand, the shear stress continually increased with the increase in shear displacement. In addition, it could be observed that with the increase of normal stress, the shear strength of sand increased, but the time of reaching the shear strength increased. Then, four coordinates were plotted in the shear strength-normal stress plane, and a best fit line which determined the Mohr-Coulomb failure envelope was obtained as shown in Figure 3.25 and Figure 3.26. The intercept of the line with the y-axis gave the cohesion, and the slope of the line gave the friction angle. The results are given in Table 3.8.

Shear stress was calculated as follow,

$$\tau = \frac{CR}{A_0} \times 10 \tag{3.16}$$

Where τ is the shear stress (kPa), C is the calibration coefficient of displacement indicator (N/0.01mm), R is the reading of displacement indicator (0.01mm), and A_0 is the initial area of sample (cm^2).

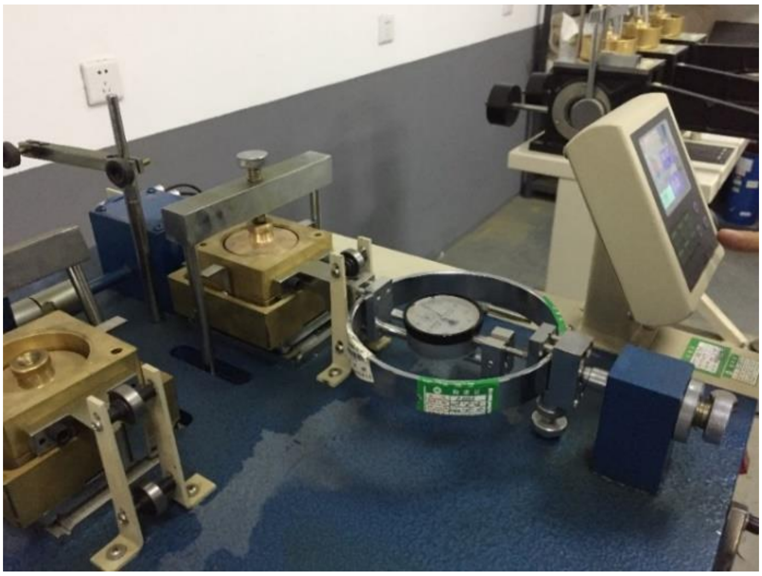

Figure 3.22: Direct shear test.

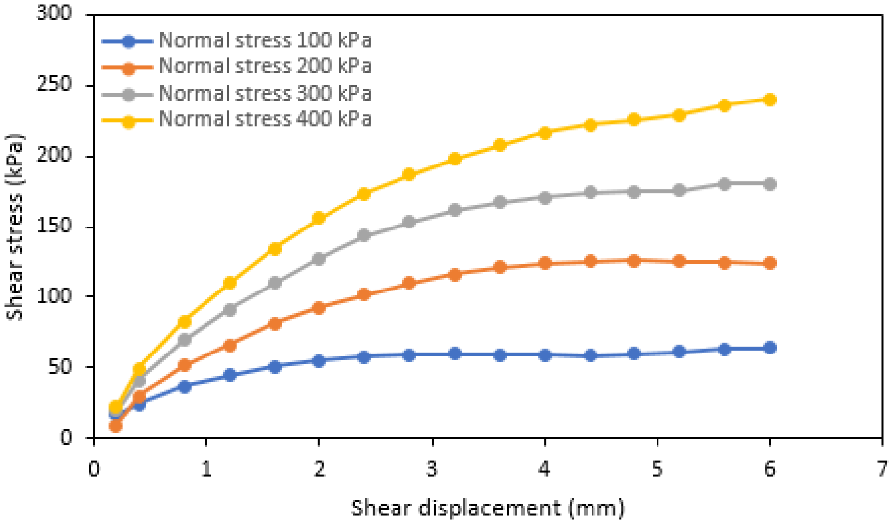

Figure 3.23: Shear stress-shear displacement curves for loose sand.

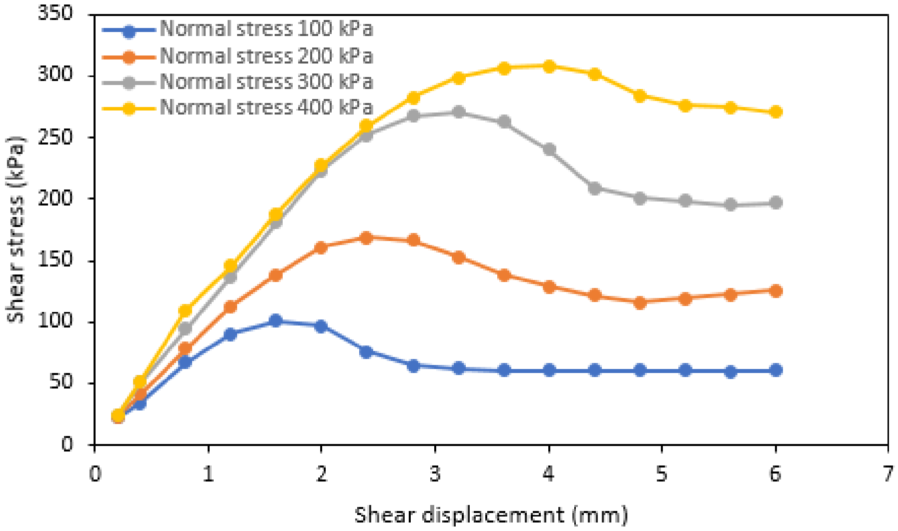

Figure 3.24: Shear stress-shear displacement curves for dense sand.

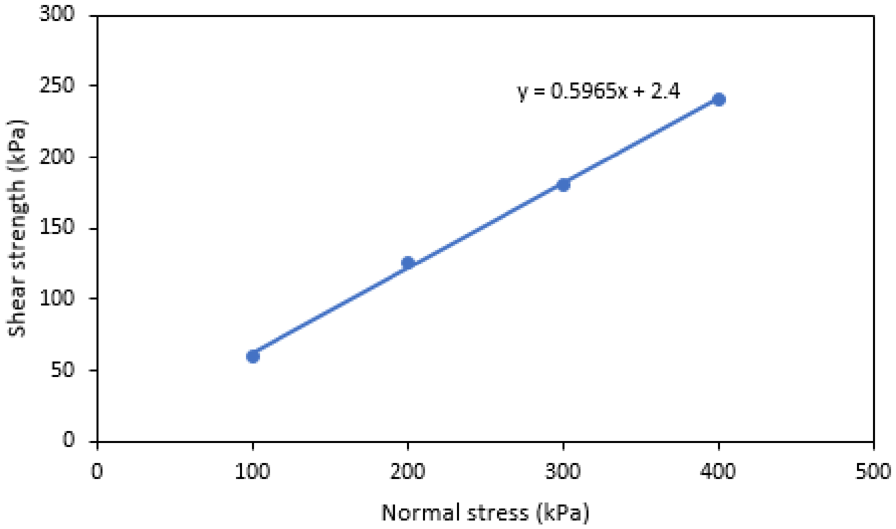

Figure 3.25: Shear strength-normal stress curve for loose sand.

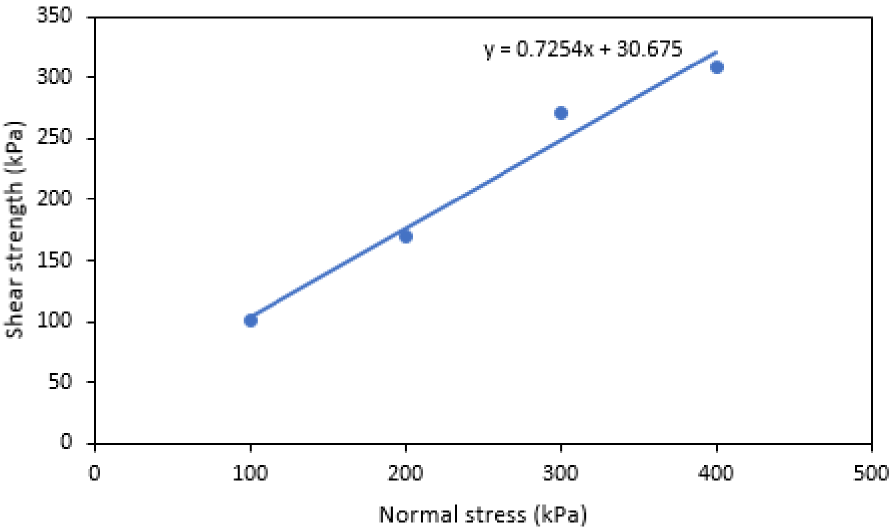

Figure 3.26: Shear strength-normal stress curve for dense sand.

Table 3.8 Angle of internal friction and cohesion of sand.

Type	Density (g/cm3)	Angle of internal friction (°)	Cohesion (kPa)
Loose	1.36	31	2.4
Dense	1.87	36	30.7

Note: Displacement rate is 0.8 mm/min.

3.6.5 Construction of model soil

The river sand was spread out on the ground and allowed to air dry for one week. Then the dry river sand was sieved with the aperture size 2 mm before filling the soil-tunnel and free-field model boxes. Compaction method was adopted to place the model soil layer by layer and the thickness of each layer was 30 cm. The predefined density was 1630 kg/m^3, corresponding to the relative density 60%. In order to ensure the uniformity of the ground, soil samples were obtained from each layer and its density was checked.

3.7 Instrumentation

Four types of data were desired to be obtained from the shaking table tests and therefore four classes of instrumentation were required. Accelerations of the sand mass, tunnel structure, and model containers could be measured by accelerometers. Bending strains in the model lining were to be obtained by resistance-type strain gauges. Deformations of the sand surface could be measured by a 3D laser scanner. Cracking of the tunnel lining during the shaking was to be observed by miniature cameras.

3.7.1 Accelerometers

The selection criteria for the accelerometers are high sensitivity, DC response, small size, and economy. Integrated Electronics Piezo Electric (IEPE) uniaxial accelerometers (TST120A500) manufactured by Test Electron were found to have good performance. For this type of accelerometer, piezo-electric crystal is mounted to the base of the accelerometer and the mass is mounted to the crystal. When the accelerometer is under vibration, the mass tends to continue its existing state of rest due to the inertia and therefore compression and tension force occur between mass and crystal. This force is proportional to acceleration following $F = ma$. The charge output generated by the crystal is converted to a low impedance voltage output. As seen in the typical frequency response curve in Figure 3.27, the resonant frequency is in the range of 25 kHz and the flat response area is approximate 0.2 ~ 2500 Hz. Table 3.9 shows the specification of the accelerometer, and Figure 3.28 illustrates its dimensions.

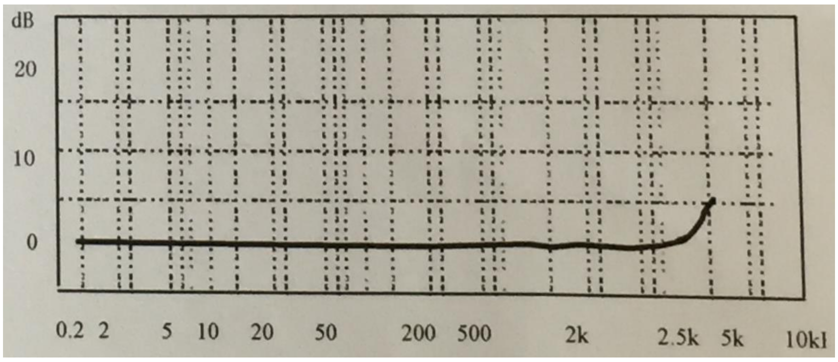

Figure 3.27: Typical frequency response curve of TST120A500 accelerometer.

Figure 3.28: Dimensions of IEPE uniaxial accelerometer (Unit: mm).

Table 3.9 Specification of uniaxial accelerometers.

Sensitivity	5.1 mV/g
Frequency range	0.2-2500 Hz
Range	±60 m/s^2
Resonant frequency	25 kHz
Supply voltage	DC 18 ~ 28 V
Weight	75 g

IEPE uniaxial accelerometers were fixed on the tunnel invert to record the horizontal response acceleration of lining. As for the response of surrounding soil, accelerometers were normally placed in the non-rigid box to increase the surface area for resistance to twisting (Chen et al., 2015; Quan, 2016; Chen et al., 2020; Han et al., 2020). In this study, accelerometers were placed in the box of polymethyl methacrylate, as shown in Figure 3.29. The size of box was $5 \times 5 \times 5$ cm which was determined following the principle of density equivalence, and the calculation process was as follow,

$$V = V_1^3 - V_2^3 = 5^3 - 3^3 = 98 \ \text{cm}^3 \tag{3.17}$$

$$m = \rho V_3 = 1.19 \times 98 = 116.62 \ \text{g} \tag{3.18}$$

$$\rho_{eq} = \frac{m+m_a}{V_1^3} = \frac{116.62+75}{125} = 1.53 \ \text{g/cm}^3 \approx 1.63 \ \text{g/cm}^3 \tag{3.19}$$

Where V is the volume of polymethyl methacrylate box, m is the mass of polymethyl methacrylate box, m_a is the mass of accelerometers, ρ is the density of polymethyl methacrylate, and ρ_{eq} is the equivalent density.

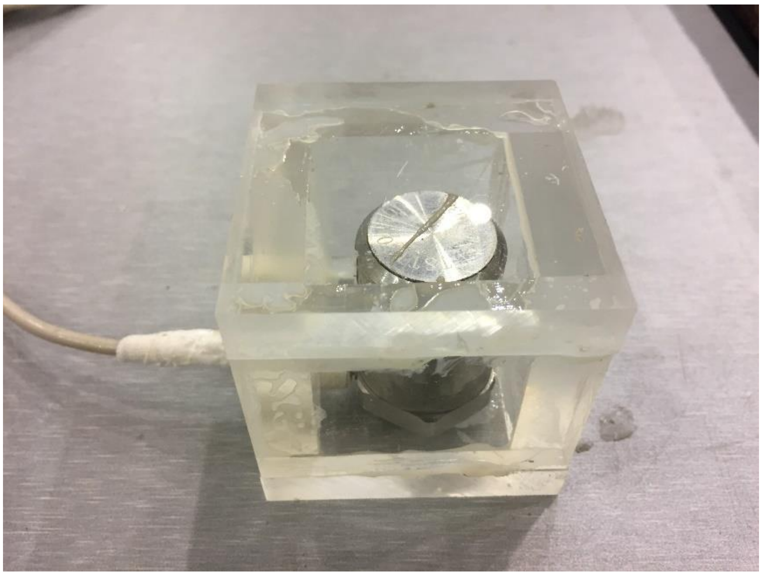

Figure 3.29: IEPE uniaxial accelerometer installed in the box of polymethyl methacrylate.

The arrangement of accelerometers in two model boxes was shown in Figure 3.30 and Figure 3.31. In the soil-tunnel mode box, 8 IEPE uniaxial accelerometers were deployed in 4 vertical arrays in the soil, and 4 accelerometers were installed in four monitoring sections of the tunnel. In the free-field model box, 12 accelerometers were placed at 4 vertical arrays in the soil. In order to assess the impact of tunnel presence on the surrounding soil, accelerometers in the soil have corresponding relationship in two model boxes. In addition, 4 Magneto-Electric accelerometers were fixed on the shaking table to monitor the input signals.

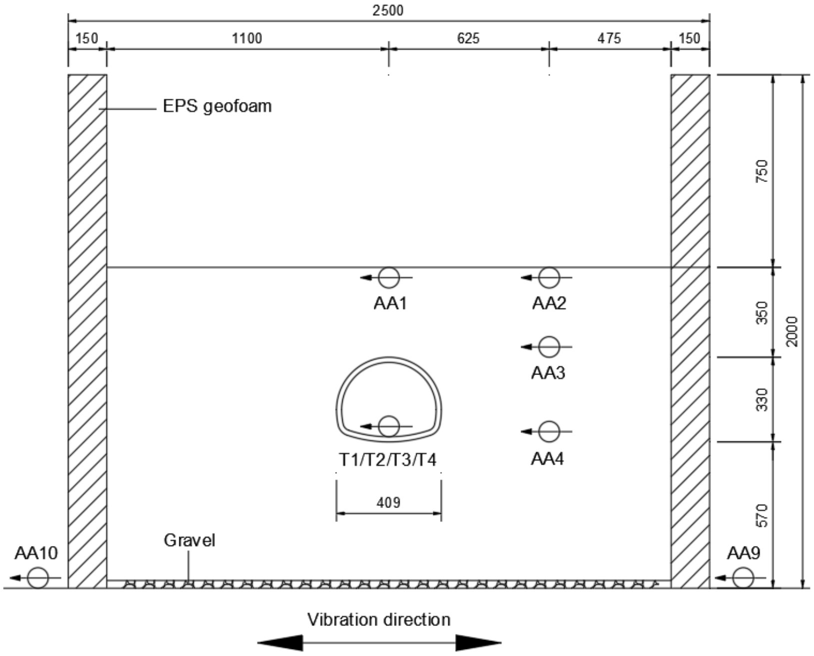

(a) Front view

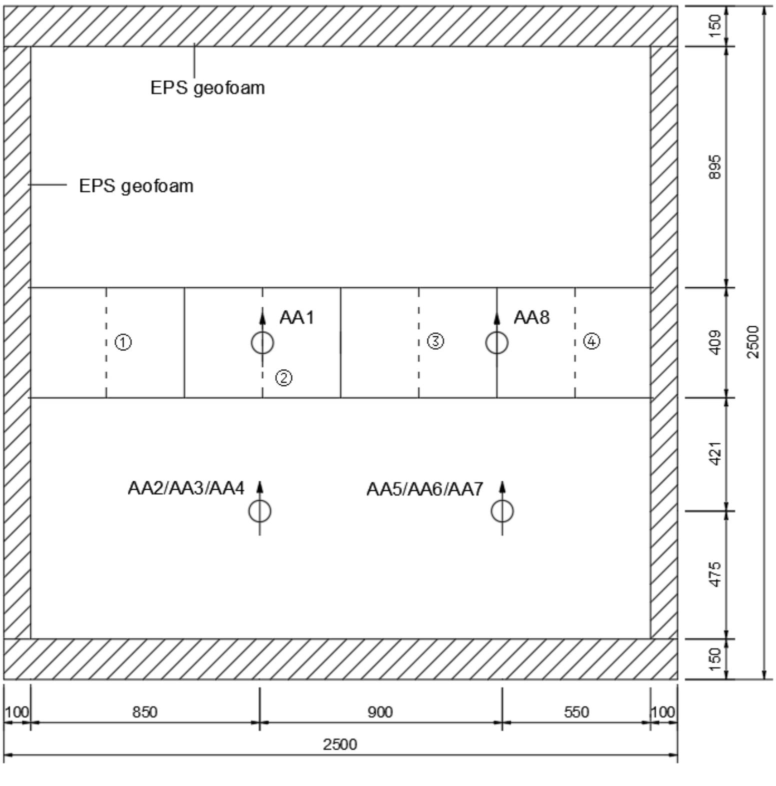

(b) Vertical view

Figure 3.30: Accelerometer arrangement in model box 1. AA means accelerometer. Direction of arrow is vibration direction. ① ~ ④ denote monitoring sections of bending strain and acceleration of lining. (Unit: mm)

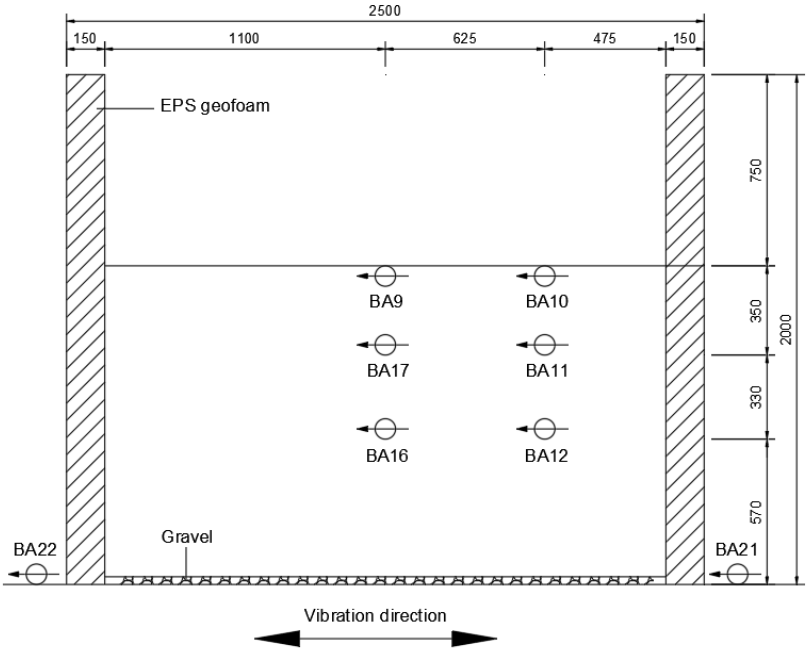

(a) Front view

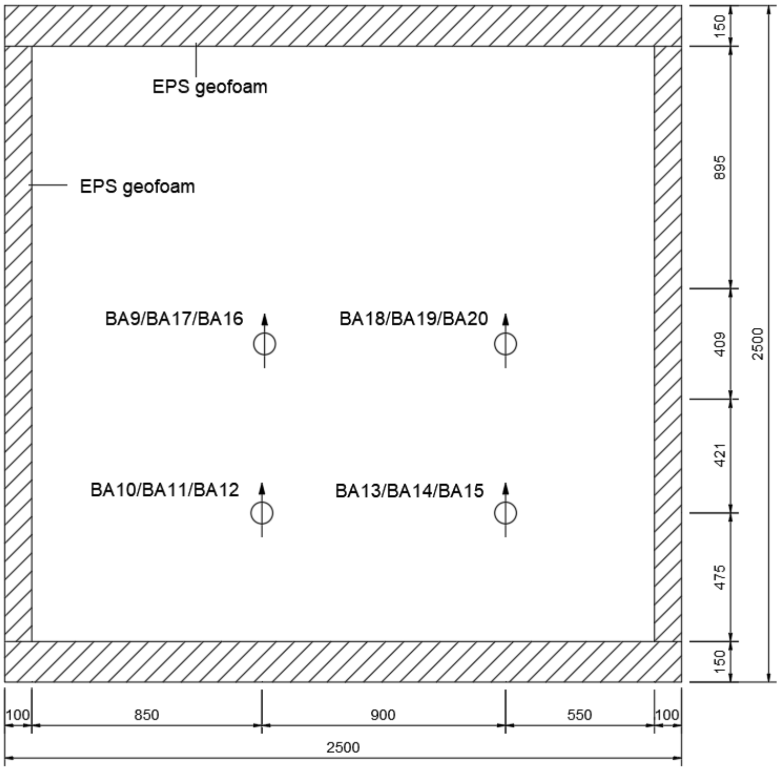

(b) Vertical view

Figure 3.31: Accelerometer arrangement in model box 2. BA means accelerometer. Direction of arrow is vibration direction. (Unit: mm)

3.7.2 Strain gauges

Temperature-compensated bonded electrical resistance foil strain gauges (BX120-3AA) as shown in Figure 3.32, manufactured by Xingtai Jinzhi Sensing Elements Factory, were used to measure bending strains of the lining structure. There were four monitoring sections longitudinally as shown in Figure 3.30 and each monitoring section was provided with eight pairs of strain gauges on opposing sides of given positions as shown in Figure 3.33. The strain gauges were attached to the compression and tension faces of the lining to record bending strains. At the gauge positions, the surface of the lining was processed by cleaning and sanding. The strain gauges were adhesive to the surface of the lining by 502 Glue, and lead wires were soldered and route through the interior and exterior of the lining. The strain gage and wire assemblies were covered by 704 silicon rubber for dampproof treatment. Then the strain gauges were calibrated by a multimeter and the deviation of resistance should be lower than 1 Ω relative to the standard resistance.

Figure 3.32: BX120-3AA strain gauges.

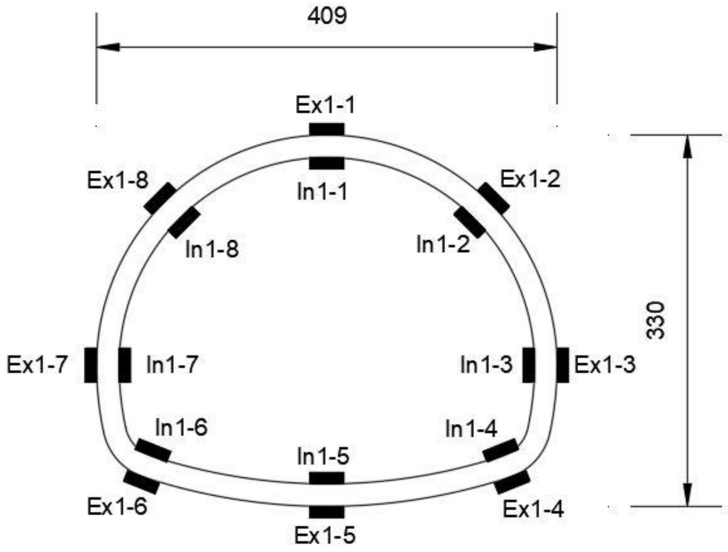

Figure 3.33: Layout of strain gauges in each monitoring section.

3.7.3 Data acquisition system

The data acquisition system is managed by the integrated software AeroPro which is run with the MTS shaking table control system. The maximum 192 data channels were provided, and acceleration and strain data can be collected synchronously. Collection of data was from the start of shaking to +10s after the shaking stops. The additional 10s could be used to capture associated free vibration behaviour of the model. The accelerometers were wired into the acquisition system with the configuration shown in Figure 3.34(a). The strain gauges were wired by the quarter bridge configuration with temperature self-compensation as shown in Figure 3.34(b). Constant input excitation voltages were supplied to the accelerometers and strain gauges, with 0.5 V and 5 V respectively. The sampling rate for the tests was 256 Hz, which is adequate for objectives of this research. The shaking table data acquisition instrument was shown in Figure 3.35.

Before the shaking table tests, the accelerometers and strain gauges were checked online through the data acquisition system, in order to identify any malfunctioning or miswired sensors. The data was collected by the acquisition system with normally units of g (acceleration) and μstrain (bending strain).

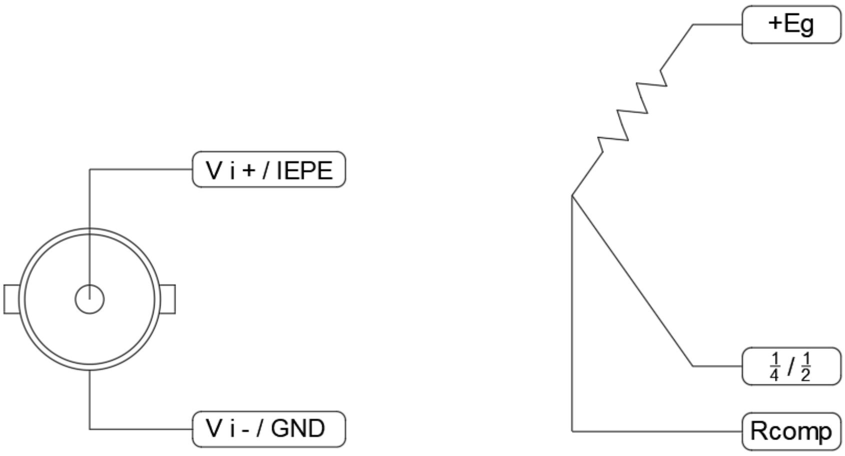

(a) accelerometers (b) strain gauges

Figure 3.34: Wiring configuration.

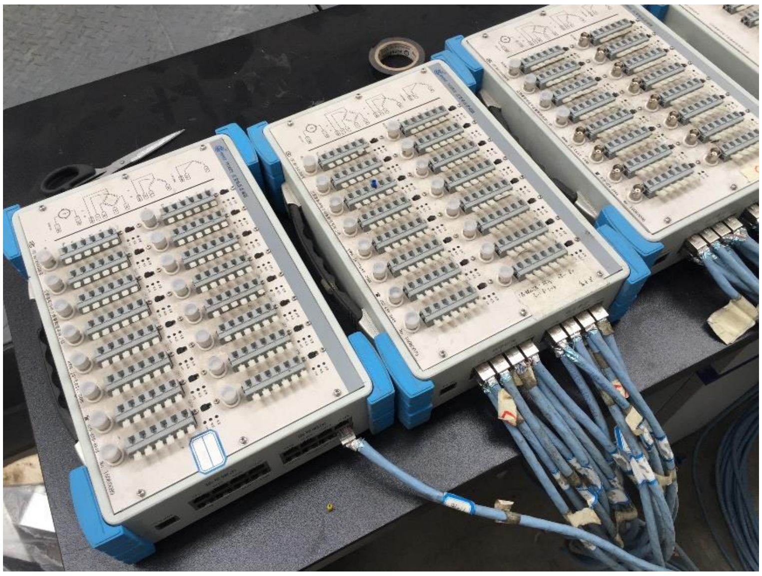

Figure 3.35: Data acquisition instrument.

3.7.4 3D laser scanner

3D laser scanning technology has been widely used to measure surface changes. This study investigated the potential use of scanning technology to detect the ground deformations of the soil-tunnel and free-field models in shaking table tests. The FARO FOCUS^S 150 (Figure 3.36) was employed to record the soil surface at eight scans, and the scanning sequence is shown in Table 3.10. The range accuracy of a single point was 1.5 mm at a distance of 10 m, and the vertical and level field of scanning were 300° and 360° respectively. Six target spheres (Figure 3.37) with diameter 7 cm were spatially fixed around the shaking table to reduce registration errors as shown in Figure 3.4. Before the shaking, the scanner was installed on a tripod which was mounted on the wood frame with dimensions of 2.5 m length and 1.2 m width via binding wires. Vertical distance between the center of scanner and the surface of frame was 1.1 m. The wood frame was elevated to the given location by crane with steel wire ropes after adjusting the scanner, and was then fastened to the middle of two model boxes with four safety ropes. The range of each scanning cooperated with vertical field of scanner to minimize the blind spots in the two model boxes. Thus, relative height from the surface of wood frame to the top of model boxes was 1.54 m. Location of the scanner relative to the shaking table and two model boxes was shown in Figure 3.38. It should be noted that this system was not involved with the dynamic measurements of the tests, and the scanner was controlled wirelessly for all scanning work.

Figure 3.36: FARO FOCUSS 150.

Figure 3.37: Target spheres.

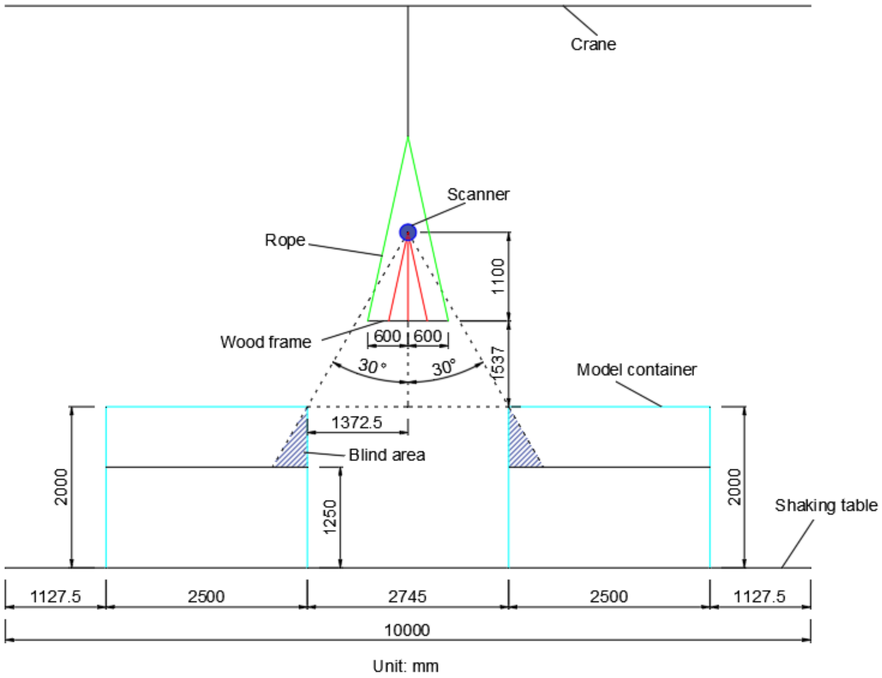

(a) Front view

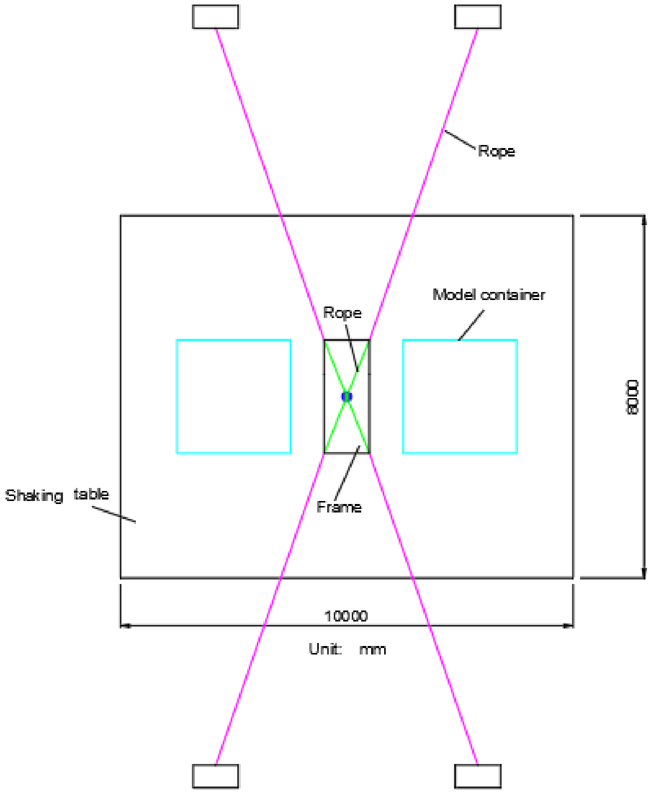

(b) Vertical view

Figure 3.38: Installation of 3D laser scanner.

3.7.5 Mini-cameras

In order to record the cracking process of tunnel lining, a new monitoring system was proposed based on the 1 g shaking table tests, as shown in Figure 3.39(a) and (b). The system was composed of CMOS mini-cameras, Micro SD cards, iPhones, and stainless steel square tube. The CMOS mini-cameras, as shown in Figure 3.39(c), were used to capture the surface of tunnel lining by video. Its resolution was 1920*1080 and frame rate was 30 FPS. The Micro SD cards were inserted to the mini-cameras to save the recordings and its storage was 32 G. The iPhones equipped with the Scam software, as the control device, were connected to each mini-camera by searching for the WiFi hotspot of this mini-camera, which supported the real time monitoring and parameter settings such as brightness, contrast, resolution, and night vision. It should be noted that each mini-camera and its corresponding iPhone had the same time, hence 16 mini-cameras were synchronized by using 16 iPhones. In the tests, 16 mini-cameras were installed on the stainless steel square tube (50 mm × 50 mm × 2800 mm) with double-sided foam tape and cable tie, as shown in Figure 3.39(d) and each lining was monitored by 4 mini-cameras in the middle cross section. The square tube crossing the four tunnel linings were fixed at the two ends of the model box with angle irons, bolts, and nuts.

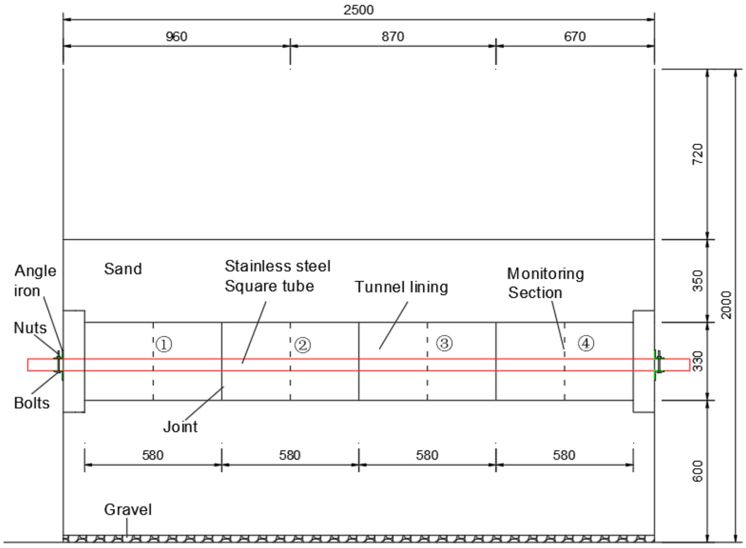

(a) Four monitoring sections in longitudinal direction

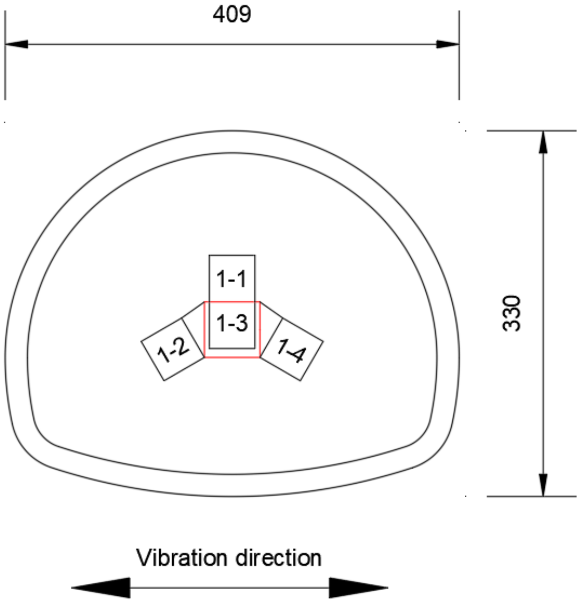

(b) Mini-cameras layout in each monitoring section

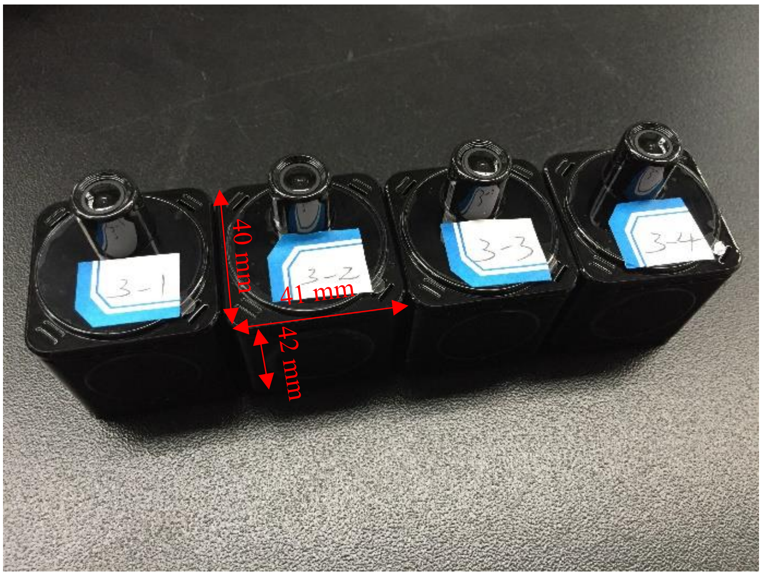

(c) Dimension of mini-cameras.

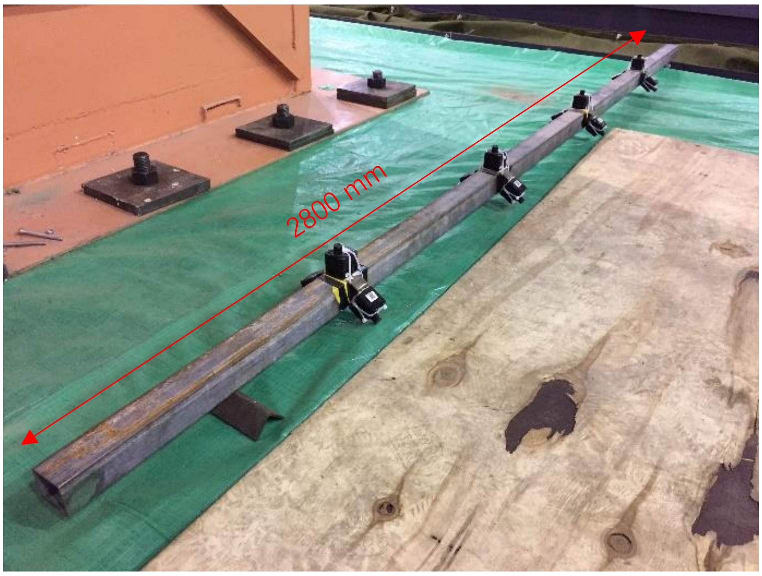

(d) Stainless steel square tube

Figure 3.39: A new cracking monitoring system equipped with mini-cameras. ① ~ ④ denote monitoring sections of lining cracks. (Unit: mm)

3.8 Input motions

Wolong record EW component from the M8.0 2008 Wenchuan earthquake was selected as the test input signal, because the examined Lebuguo tunnel is near the epicenter of the Wenchuan earthquake and severe damage was observed in many tunnels after this earthquake (Wang et al., 2009; Li, 2012; Wang and Zhang, 2013; Shen et al., 2014). The acceleration time history is shown in Figure 3.40(a), and acceleration Fourier spectra is depicted in Figure 3.40(b). The record has a predominant frequency of 2.4 Hz, a time step of 0.005 s, and a peak acceleration of 1.0 g. For this testing study, it is scaled to 0.3, 0.5, 0.6, 0.7, and 0.8 g. Following the similarity relations in Table 3.2, time scale of the original record is compressed by ratio of 5.5. A low level white noise signal is used to diagnose the variation of system resonant frequencies; an acceleration level of < 0.05 g is intended to guarantee that the structure are not imposed additional damage. Table 3.10 shows the loading sequence in the shaking table tests. In total, there are 47 motions exerted in the system including 10 with the amplitude of 0.3 g, 10 with the amplitude of 0.5 g, 3 with the increasing amplitudes of 0.6 g, 0.7 g and 0.8 g, and 24 white noise tests. Except for the cumulative damage caused by the repeated seismic shaking in 0.3 g and 0.5 g stages, the last three loading cases are adopted to observe the progressive damage explored in previous studies (Wang et al., 2015; Xin et al., 2019; Xu et al., 2021). It should be noted that all motions were input at the base of the model boxes along the transversal direction of the tunnel structure.

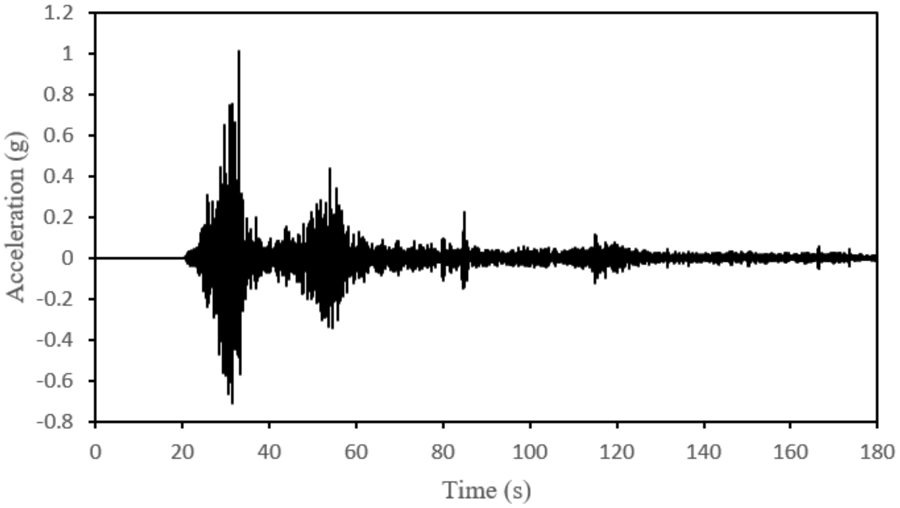

(a) Acceleration time histories

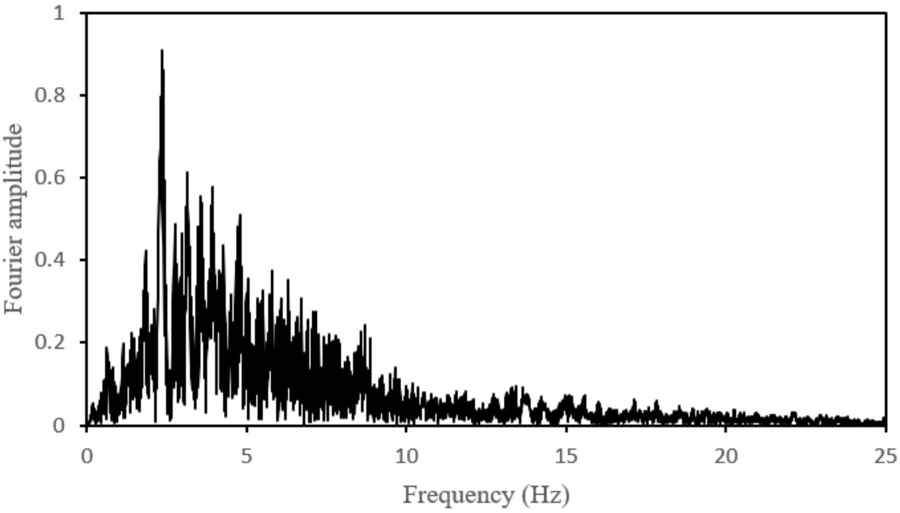

(b) Fourier amplitude spectrum

Figure 3.40: Wolong record EW component.

Table 3.10 Loading sequence.

Test ID	Test description	Scanning work
IM-1	0.05 g white noise	
IM-2	0.3 g compressed Wolong wave	Before IM-2
IM-3	0.05 g white noise	
IM-4	0.3 g compressed Wolong wave	
IM-5	0.05 g white noise	
IM-6	0.3 g compressed Wolong wave	After IM-6
IM-7	0.05 g white noise	
IM-8	0.3 g compressed Wolong wave	
IM-9	0.05 g white noise	
IM-10	0.3 g compressed Wolong wave	
IM-11	0.05 g white noise	
IM-12	0.3 g compressed Wolong wave	After IM-12
IM-13	0.05 g white noise	
IM-14	0.3 g compressed Wolong wave	
IM-15	0.05 g white noise	
IM-16	0.3 g compressed Wolong wave	
IM-17	0.05 g white noise	
IM-18	0.3 g compressed Wolong wave	
IM-19	0.05 g white noise	
IM-20	0.3 g compressed Wolong wave	After IM-20
IM-21	0.05 g white noise	
IM-22	0.5 g compressed Wolong wave	
IM-23	0.05 g white noise	
IM-24	0.5 g compressed Wolong wave	
IM-25	0.05 g white noise	
IM-26	0.5 g compressed Wolong wave	After IM-26

IM-27	0.05 g white noise	
IM-28	0.5 g compressed Wolong wave	
IM-29	0.05 g white noise	
IM-30	0.5 g compressed Wolong wave	
IM-31	0.05 g white noise	
IM-32	0.5 g compressed Wolong wave	After IM-32
IM-33	0.05 g white noise	
IM-34	0.5 g compressed Wolong wave	
IM-35	0.05 g white noise	
IM-36	0.5 g compressed Wolong wave	
IM-37	0.05 g white noise	
IM-38	0.5 g compressed Wolong wave	
IM-39	0.05 g white noise	
IM-40	0.5 g compressed Wolong wave	After IM-40
IM-41	0.05 g white noise	
IM-42	0.6 g compressed Wolong wave	
IM-43	0.05 g white noise	
IM-44	0.7 g compressed Wolong wave	After IM-44
IM-45	0.05 g white noise	
IM-46	0.8 g compressed Wolong wave	
IM-47	0.05 g white noise	

3.9 Summary

The shaking table facility at NEDL is used. The size of testing platform is 10 m × 8 m and the frequency range is 0.1-50 Hz. The dimension of two equivalent model boxes is 2.5 m length, 2.5 m width, and 2.0 m height. EPS geofoams with thickness of 15 cm as absorbing boundaries are placed on the inner sides of containers to reduce the reflections and refractions of seismic waves during the tests. A layer of gravel with thickness of 30 mm was glued at the bottom of the model boxes to increase the friction between ground and model container. Also, the elastic similarity relations derived by the Buckingham-π theorem and the equation (3-7) obtained based on two dimensionless parameters s and N_P are combined together to investigate the seismic response of tunnel structures. Moreover, the uniaxial compression tests and four-point bending tests were conducted to find the appropriate mix proportion of microconcrete, namely cement, slaked lime, river sand, and water with weight ratio of 0.8: 0.8: 6: 2.4. 316 stainless steel wire with diameter 0.2 mm was selected as the model reinforcement and its strength and elongation were measured by the tensile tests. The dry river sand in Sichuan province was adopted to model the ground surrounding the tunnel, and the sand properties were measured by sieve analysis, compaction tests, funnel method, pycnometer tests and direct shear tests. Furthermore, four types of sensors were installed, including accelerometers placed for measuing accelerations of sand mass, structure and shaking table, strain gauges adopted for measuring bending strains of structure, 3D laser scanner used for estimating ground deformations, and mini-cameras used for recording the evolution of tunnel damage. Finally, Wolong record EW component from the M8.0 2008 Wenchuan earthquake was selected as the test input signal. In order to diagnose the variation of system dynamic properties, white noise tests were conducted before and after each seismic shaking.

Chapter 4　Shaking table test results

4.1 Introduction

This chapter presents the results of the shaking table test program discussed in Chapter 3. As previously described, the shaking table model tests were designed to investigate the cumulative effect of multiple earthquake shakings on tunnel integrity, and the influence of tunnel presence on the response of surrounding soil. Therefore, a rich data set was generated over the course of multiple seismic shakings. Considering the length of the thesis, only representative results are reported. This chapter is organized as follows. Firstly, the ground deformations in the soil-tunnel and free-field model boxes are presented based on the 3D point cloud datasets and post-earthquake observations. Secondly, the structural damages are discussed according to the image data and post-earthquake observations. Thirdly, the variation of dynamic properties of tunnel structures is analyzed through the white noise tests. Also, the acceleration amplification effects in the seismic response of tunnel and soil are presented. Finally, the lining dynamic strains are studied using the strain data at the monitoring positions.

4.2 Ground deformation

This section first examined the distribution and development of the seismically-induced ground deformations in the soil-tunnel and free-field systems simultaneously during 1 g shaking table tests with LiDAR technology. Sand densification effects and the influence of tunnel presence on the soil response were assessed based on the settlements of the soil surface. Similar researches have not been seen in the literature. Then, the measurement results were compared with the post-earthquake observation results.

4.2.1 Registration errors

Registration is the process of aligning the coordinate systems of individual point clouds to a reference coordinate system with the transformation matrix which includes three translation and three rotation parameters. In this study, CloudCompare v2.12

(http://www.danielgm.net/cc/) was used to register successive point cloud datasets at eight scans with six spatially fixed target spheres. The scanning sequence was introduced in Table 3.9. Table 4.1 shows the registration errors of seven simulations, and the average value was 0.867 mm. Registration errors are inevitable during the processing of LiDAR data, and they will propagate into point cloud distance measurements and have a significant impact on small magnitude detections. In order to minimize these errors, target spheres were arranged outside the shaking table with different distances and angles from the scanner in this study. The calculated average error was lower than 1 mm, which can meet the accuracy of exploring surface elevation changes during the dynamic experiments. In addition, the registration errors as one source of uncertainties were used for later M3C2 distance calculations.

Table 4.1 Registration errors for alignment of successive scans (Unit: mm).

Simulation ID	Description	Registration error
1	Scan 1-Scan 2	0.848
2	Scan 2-Scan 3	1.145
3	Scan 3-Scan 4	0.627
4	Scan 4-Scan 5	1.007
5	Scan 5-Scan 6	0.817
6	Scan 6-Scan 7	0.812
7	Scan 7-Scan 8	0.811
Average		0.867

4.2.2 Elevation change detections

The M3C2 algorithm proposed by Lague et al (2013) was applied to measure surface elevation changes in this study. For any given core point i, the local normal vector *N* is estimated by fitting a plane to all the points contained in a neighbourhood within a radius of *D*/2, as shown in Figure 2.9(a). The normal scale *D* determines the normal direction. Then a search cylinder is defined and projected from point cloud 1 (reference) to point cloud 2 (compared) along the normal vector *N*, as shown in Figure 2.9(b). The radius and height of cylinder are called projection scale d and maximum depth h respectively. The mean position of each intersected cloud, i_1 and i_2, is obtained, and the distance from i_1 and i_2 is M3C2 distance. To obtain more accurate results, scale *D* should be 20-25 times the local roughness scale and scale d need to include the minimum 20 scanning points (Lague et al., 2013). In this study, the normal scale D and projection scale *d*, as crucial parameters, were assigned values of 0.032 m and 0.016 m respectively.

For each estimated distance, the M3C2 algorithm also considers the distance uncertainties combining the surface roughness, position uncertainty, and registration error. Level of Detection (LOD) at 95% confidence interval is defined by:

$$LOD_{95\%} = \pm 1.96\left(\sqrt{\frac{\sigma_1(d)^2}{n_1}+\frac{\sigma_2(d)^2}{n_2}}+reg\right) \tag{4.1}$$

Where $\sigma_1(d)$ and $\sigma_2(d)$ are the independent variances of point positions for each sub-point cloud, and n_1 and n_2 are the number of points in each sub-point cloud, and reg is the registration error between the two multitemporal point clouds. The measured distances are regarded as significant changes when they are larger than $LOD_{95\%}$. Above distance change detections and later volumetric change estimations were both conducted in the CloudCompare software.

Figure 4.1 shows the significant surface elevation changes between successive point cloud datasets. The left and right half of each case track the relative changes of soil-tunnel and free-field models respectively. The location of tunnel is denoted by dashed lines. For the simulation 1, it could be observed that obvious surface settlements occurred in two model boxes after three seismic shakings with the amplitude of 0.3 g. Clearly, the densification of sand during the dynamic process resulted in the settlements of the ground surfaces. In the soil-tunnel model system, apparent settlement trough was induced above the tunnel, but it was not symmetrically distributed at the soil surface, implying the uneven settlement. As the distance from the central axis increased, the settlement had a tendency to decrease. The value at the bottom of trough represented approximate 10 mm. Also, along the longitudinal axis of tunnel, the settlements at the two ends were lower than that in the middle region, which might be influenced by the tunnel ends. In the free-field model system, the deformations were almost uniform and lower than 5 mm except for the local areas. Based on the results of two model boxes, it could be found that the presence of tunnel can influence the response of the surrounding soil in the limited region. For the simulation 4, the soil settlements were computed after three seismic shakings with the amplitude of 0.5 g. As can be seen, significant deformations in the soil-tunnel model box still focused on the tunnel region, but the values were lower than that in the simulation 1. Furthermore, the settlements in the tunnel end regions tended to be consistent with that in the non-end region. As for the free-field model, the vertical displacements of the soil surface became more well distributed. According to the results in this simulation, it could be observed that the sand densification continued to develop, and the impact of tunnel presence on the soil response still existed. For the last simulation, the impact of high intensity with the PGA 0.6 g and 0.7 g was investigated. The elevation changes in the tunnel region tended to be stable. Near the end region, there was a hole in the soil surface, which was caused by the cracking of the tunnel structure. Also, the free-filed deformations reached stable. Overall, in the course of multiple earthquake shakings, the densification effects of sand could be observed in the two model boxes simultaneously and the influence of tunnel presence on the soil response was restricted in the limited region which was within around 1.5D-2D in the transversal direction. In addition, the tunnel ends could slightly influence the soil response around the local areas, but it did not interfere the observation in the middle region.

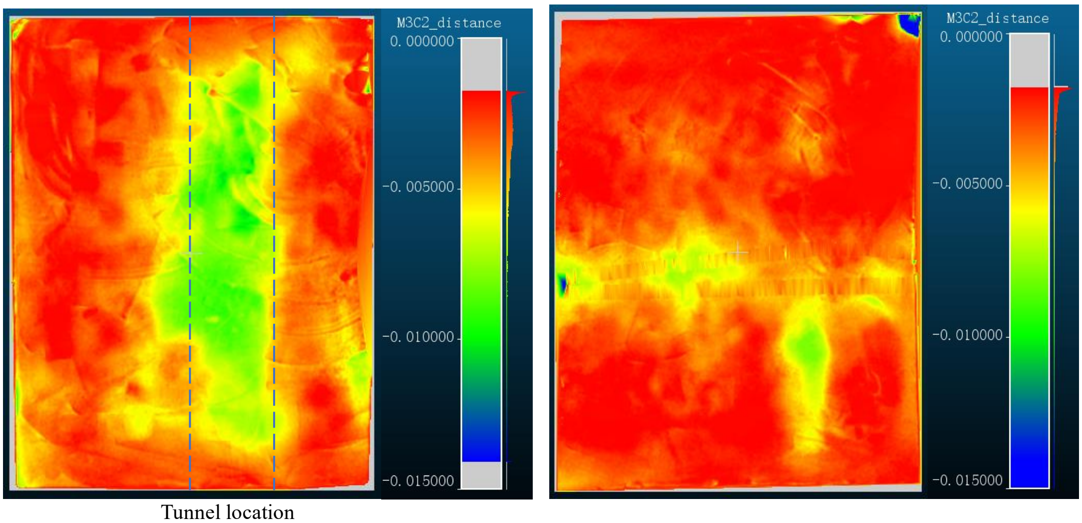

(a) Simulation 1 (scan 1-scan 2)

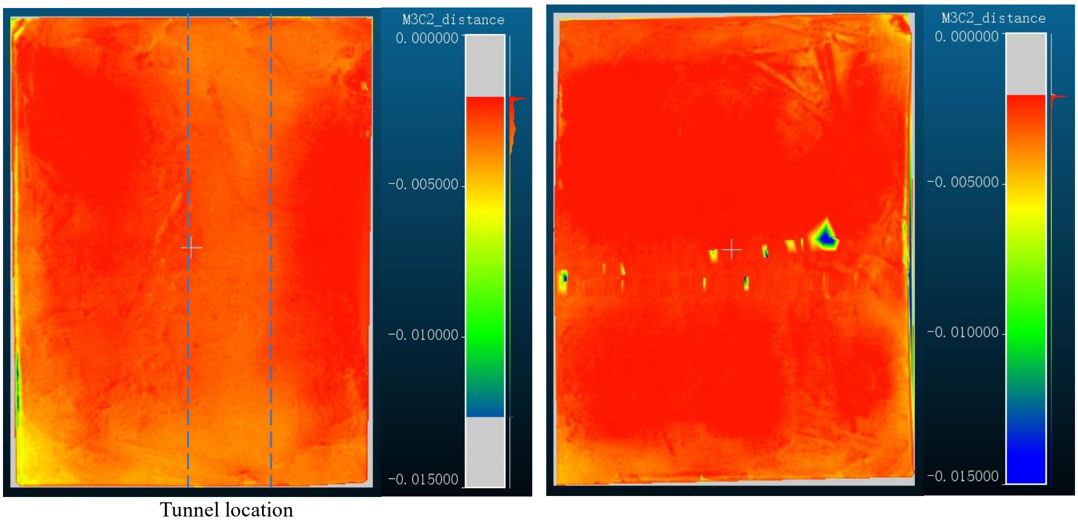

(b) Simulation 4 (scan 4-scan 5)

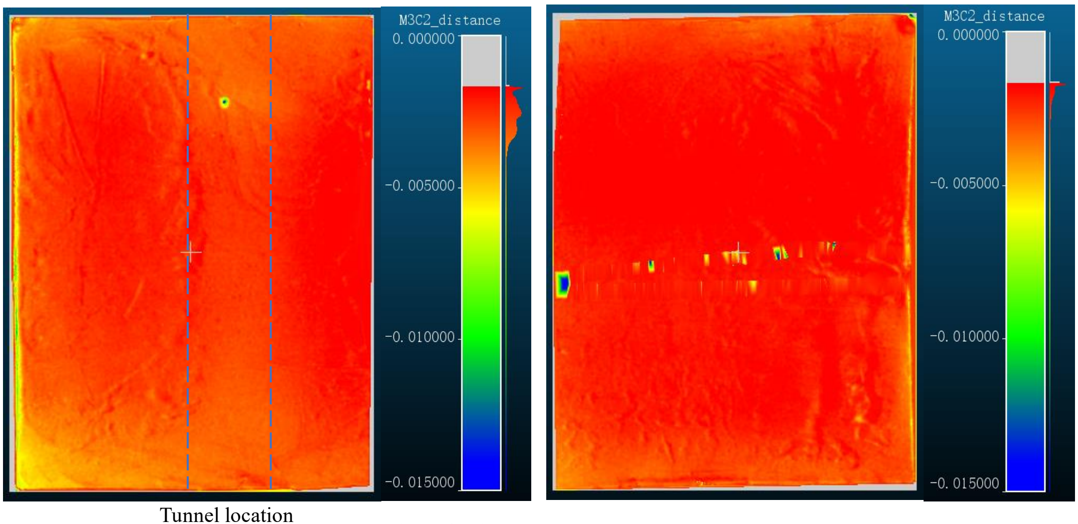

(c) Simulation 7 (scan 7-scan 8)

Figure 4.1: Significant surface elevation changes (left column: relative changes of soil-tunnel model; right column: relative changes of free-field model).

Table 4.2 shows the mean values of significant surface elevation changes for all seven simulations. The mean values were extracted from the Gaussian distribution model of detection results. For each simulation, negative values accounted for the settlement of the sand surface. The results indicated that the soil surfaces in two models settled continuously, and the mean values of the soil-tunnel model were bigger than that of the free-field model. In order to better describe the settlement trend in two models, the accumulated mean values were shown in Figure 4.2. From the beginning to the shaking 6, there was a significant increase for the settlement value because initial relatively loose sand densified quickly during the shaking. Between the shaking 6 and 20, it was evident that the settlement of the ground gradually grew slower when the intensity of seismic shaking remained unchanged, indicating that the sand densification tended to be stable. After the intensity increased to 0.5 g, the settlements first had a dramatic rise and then increased slowly. During this period ranging from the shaking 20 to 40, higher intensity triggered the further development of soil settlement. Entering the 0.6 g and 0.7 g stage, the slope of the settlement obviously increased again. It should be noted that although this stage had only two seismic shakings, its increment was slightly larger than that in the period with five excitations from the shaking 32 to 40, revealing the influence of high seismic intensity for ground failure. At the end of the tests, the accumulated values of the soil-tunnel model and free-field model were 19.422 mm and 17.108 mm respectively. Overall, during the evolution of surface settlements, there were three critical points which were at the shaking 6, shaking 26, shaking 44 respectively, since they accompanied with the obvious increase of the slope. Also, it was clear that the response of tunnels not only resulted from the soil shear deformation, but also the ground settlement. The combined effects of them may heavily damage the tunnel, which could be reflected by the results of structural damage indicated in Section 4.3.

Table 4.2 Mean values of surface elevation changes (Unit: mm).

Simulation ID	Description	ST model	FF model
1	Scan 1-Scan 2	-4.382	-3.162
2	Scan 2-Scan 3	-2.743	-3.280
3	Scan 3-Scan 4	-1.855	-1.661
4	Scan 4-Scan 5	-3.068	-2.740
5	Scan 5-Scan 6	-2.023	-1.946
6	Scan 6-Scan 7	-2.563	-2.031
7	Scan 7-Scan 8	-2.788	-2.288
Total		-19.422	-17.108

Note: ST model denotes soil-tunnel model and FF model is free-field model.

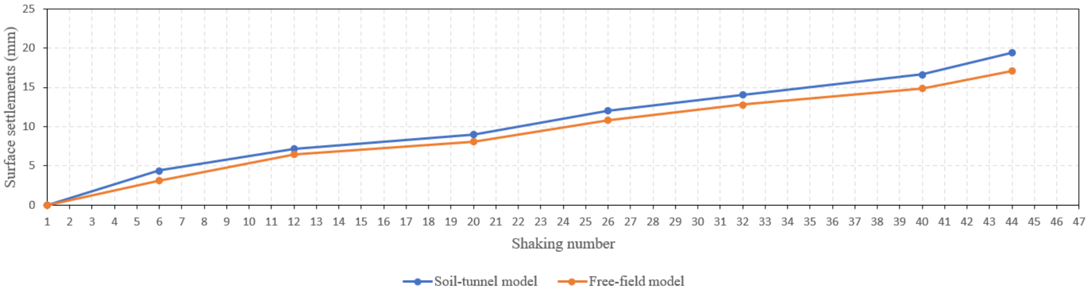

Figure 4.2: Variation of surface averaged settlements for the soil-tunnel and free-field models.

4.2.3 Volumetric change estimations

Once the M3C2 distances and uncertainty measure $LOD_{95\%}$ were obtained, only points with significant changes were used to estimate the volumetric changes in this study. Firstly, the points with significant changes were found out from a scalar field with binary attributes, 1 for significant changes and 0 for non-significant changes, and were separated out to generate a new point cloud. The resulting point cloud then was projected on to a 0.005 m grid. The voids within the points were filled with the linear interpolation method. The average differences in height of all points inside the grid was calculated for each cell. The volumetric changes were estimated with the area of cell and average difference in each cell.

Following the above method, the volumetric changes were estimated with the significant surface elevation changes (M3C2 with $LOD_{95\%}$) for seven simulations, as shown in Figure 4.3. To verify the accuracy of this method, the results were compared to the estimations using the DoD and M3C2 without $LOD_{95\%}$ methods. DoD, as a traditional method, was based on the difference of digital elevation models, and $LOD_{95\%}$ calculated by equation (4-1) represented the distance uncertainties. It was evident that the variation trends of volumetric reductions by three methods were consistent through the simulations. The estimations for the soil-tunnel model were significantly greater than that for the free-field model, indicating that the tunnel presence had the impact on the soil response. The estimations of DoD method were close to that of M3C2 without $LOD_{95\%}$ method in both models, implying that the advantage of M3C2 on the exhibition of different characteristic scales disappeared. Furthermore, these two methods highly overestimated the volumetric changes compared to the M3C2 with $LOD_{95\%}$ method, owing to that $LOD_{95\%}$ can separate non-significant changes from the calculations considering the uncertainties from surface roughness, position uncertainty, and registration error. Overall, the M3C2 with a spatially variable confidence interval method used in this study was more accurate to capture the ground deformations in the course of multiple seismic shakings.

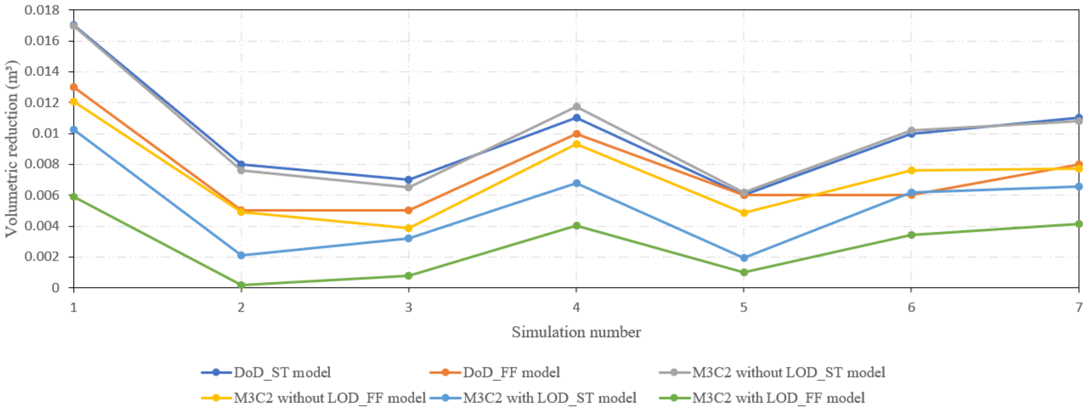

Figure 4.3: Estimations of volumetric reduction using DoD, M3C2 without LOD, and M3C2 with LOD methods in two models.

4.2.4 Observed soil deformation

Figure 4.4 and Figure 4.5 show the deformations of the soil surface in the soil-tunnel model and free-field model after the tests respectively. The red lines in the figures represented the height of the initial ground. It could be observed that the surface settlements in two models were obvious and the values were about 20 mm. The results were consistent with the detections by the 3D point cloud technology, indicating that the M3C2 algorithm was accurate. In addition, two holes were found on the ground surface of the soil-tunnel model, resulting from the cracking of the tunnel lining. One hole had been observed after the excitations of 0.6 g and 0.7 g, as shown in Figure 4.1(c), while the other was caused by the input with the amplitude of 0.8 g. Therefore, the structural damage resulted from the combined effects of the soil shear deformation and ground settlement, and the influence of high seismic intensity was apparent.

Figure 4.4: Soil surface in soil-tunnel model after the final input IM-47.

Figure 4.5: Soil surface in free-field model after the final input IM-47.

4.3 Structural damage

As previously described, a new cracking monitoring system equipped with wireless mini-cameras was proposed to detect the evolution of tunnel damages during 1 g shaking table tests. The arrange of the system was shown in Figure 3.39. In this section, based on image processing techniques, cracks in acquired images were identified and measured. To quantify the level of tunnel damage, a damage index was defined. Furthermore, the post-earthquake observation results of the tunnel structures were presented.

4.3.1 Crack identification and measurement method

Once the images of lining surface were acquired using the proposed cracking monitoring system, lining cracks were identified and measured according to the image processing techniques. Crack identification mainly includes the steps of contrast stretching, median filtering, locally adaptative thresholding segmentation, area opening operation, and skeletonization. Crack measurement is the calculation of crack average width, length and area through the binary image and skeleton. In the following sections, the processing methods are presented by using the data of mini-camera 2-4 from the lining 2 after the shaking IM-2.

4.3.1.1 Contrast stretching

The acquired images were first cropped to highlight the targeted cracks, as shown in Figure 4.6(a), avoiding the interferences of sensors, wire, and stains. In order to improve the computation efficiency for the subsequent processing, the original images with color were converted to grayscale images as shown in Figure 4.6(b) retaining the luminance information by using a weighted sum of the R, G, and B channels (MATLAB, R2021a),

$$f(x,y) = 0.2989R(x,y) + 0.5870G(x,y) + 0.1140B(x,y) \qquad (4.2)$$

Where (x,y) is the pixel coordinate.

Due to the low contrast of grayscale images caused by low and uneven lighting inside the tunnel, stretching method was applied to increase the image contrast by saturating the bottom 1% and the top 1% of all pixel intensity values. Figure 4.6(c) shows the contrast enhanced image, and the crack was more obvious in the image compare to that in Figure 4.6(b).

4.3.1.2 Median filtering

During the monitoring of the shaking table tests, noise might exist due to the vibration of the mini-cameras installed on the stainless steel square tube and uneven illumination mentioned above, which disturbed the crack identification to some degree. In order to increase the accuracy of crack identification, it was necessary to reduce the noise of the image. Median filtering (Lim, 1990) as a nonlinear operation was employed to remove the noise from the images without reducing the sharpness of images. In the output image, each pixel contained the median value in a 3-by-3 neighborhood around the corresponding pixel in the input image. Figure 4.6(d) shows the image after median filtering.

4.3.1.3 Thresholding segmentation

After the removing of noise, it can be seen that the crack regions were darker than the background, indicating that the gray values of cracks were lower than the values of background. This property could be used to separate the cacks from the image by applying a thresholding operation. In this study, binary images were obtained using locally adaptative thresholding segmentation (Bradley and Roth, 2007) which means that each input pixel was allocated a threshold using the local mean intensity around the neighborhood of the pixel, as shown in Figure 4.6(e). The pixel values of foreground (crack regions) and background were set to 0 (black) and 1 (white) respectively. Following the binarization operation, logical negation was performed on the binary images, as shown in Figure 4.6(f). Thus, the pixel values of crack and non-crack regions were set to 1 (white) and 0 (black) respectively.

4.3.1.4 Area opening operation

After the negation operation, there were still many misidentified objects in the image although the crack information was recognized well. This issue might result from the uneven illumination, stains, and uneven lining surface. In order to reduce the distractions for the following processing, these objects need to be removed. Area as a characteristic parameter could be used to distinguish the crack regions from the non-crack objects. Therefore, area opening operation was utilized to remove the connected components for which area was lower than the given value from binary images, as shown in Figure 4.6(g). It should be noted that the threshold of area cannot be too large to exclude the crack regions. Then, remained connected components in the image were detected, labelled, and measured for the sake of the identification of crack regions, as shown in Figure 4.6(h). Finally, the crack identification results were presented in Figure 4.6(i).

4.3.1.5 Crack measurement

Once the crack identification was completed, the crack could be quantified by three feature parameters such as crack average width, length and area, according to the binary image and crack skeleton. The skeleton of crack regions was obtained by removing the pixels on the boundaries of objects without allowing objects to break apart (Kong and Azriel, 1996), as shown in Figure 4.6(j). Meanwhile, spurs or branches of skeleton were removed as much as possible. Then, Euclidean distance transforms (Maurer et al., 2003) of the binary images were computed to extract the distances along the skeleton image of the crack. For each pixel in binary images, the distance between that pixel and the nearest nonzero pixel was calculated based on the distance transform. The crack average width was then obtained. As for the crack area, it could be received according to the measurement for the labelled connected components, while the crack length was calculated by the ratio of the area to average width.

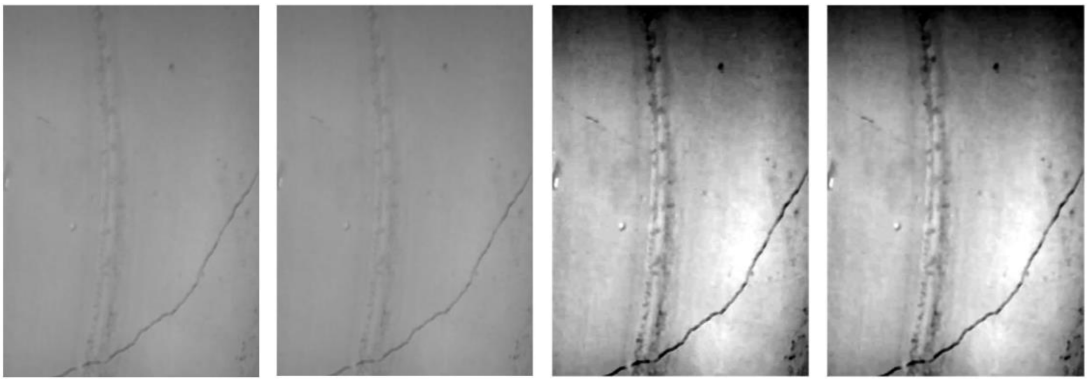

(a) Original image (b) Grayscale image (c) Intensity adjust (d) Median filtering

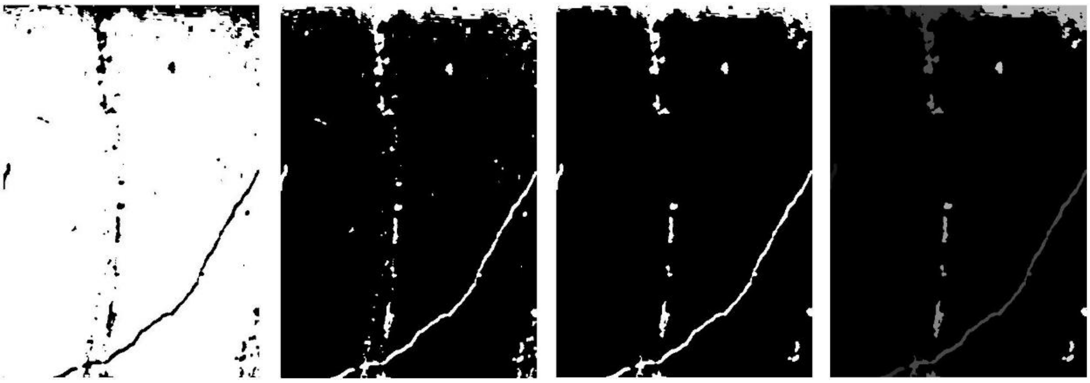

(e) Binary image (f) Negation (g) Area opening operation (h) Labelled

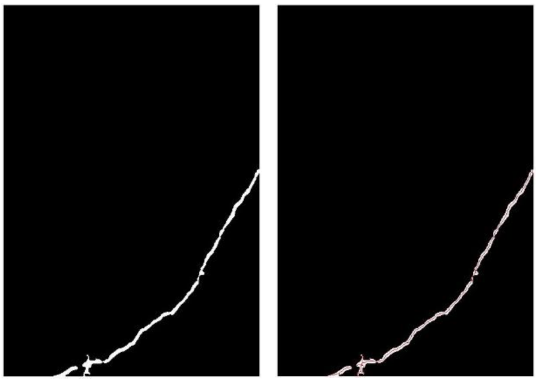

(i) Crack (j) Skeleton

Figure 4.6: Crack extraction of the lining 2 after shaking IM-2.

4.3.2 Crack parameters

This section introduces the evolution of tunnel damages recorded by the proposed monitoring system during the shaking table tests. The acquired data of mini-cameras 2-4 and 3-2 was analyzed as the examples. Figure 4.7 and Figure 4.8 show the cropped original images of two mini-cameras respectively, and every image was obtained after the seismic shaking of Table 3.9. It could be seen that two linings had damages after the first shaking, and the cracks both occurred near the springing of linings, which referred to the ovaling deformation mode of tunnels under the seismic shear waves (Owen and Scholl, 1981; Wang, 1993; Hashash et al., 2001; Tsinidis et al., 2020). Also, with the increasing of the number of vibrations, the damage of linings tended to be more obvious. To describe the cracking process of two linings quantitatively, the methods mentioned in Section 4.3.1 were utilized to identify and measure the cracks in these images. For example, the crack extraction of the lining 2 after shaking IM-2 was shown in Figure 4.6, and that of the lining 3 after shaking IM-4 was presented in Figure 4.9.

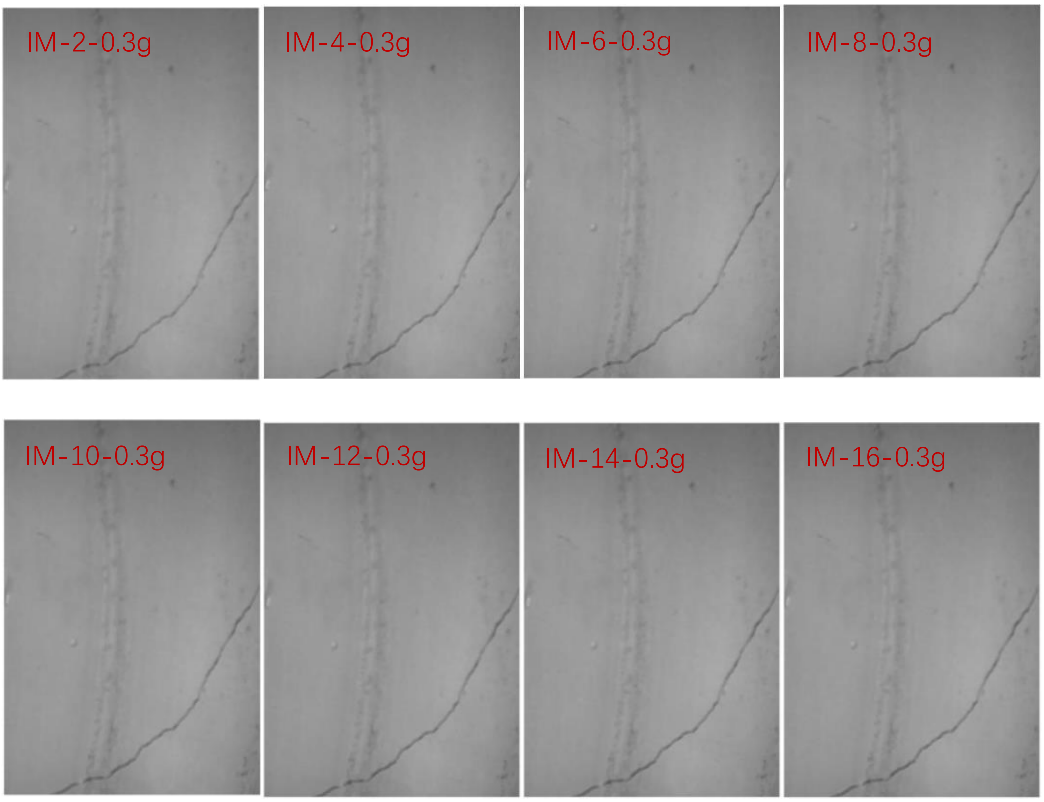

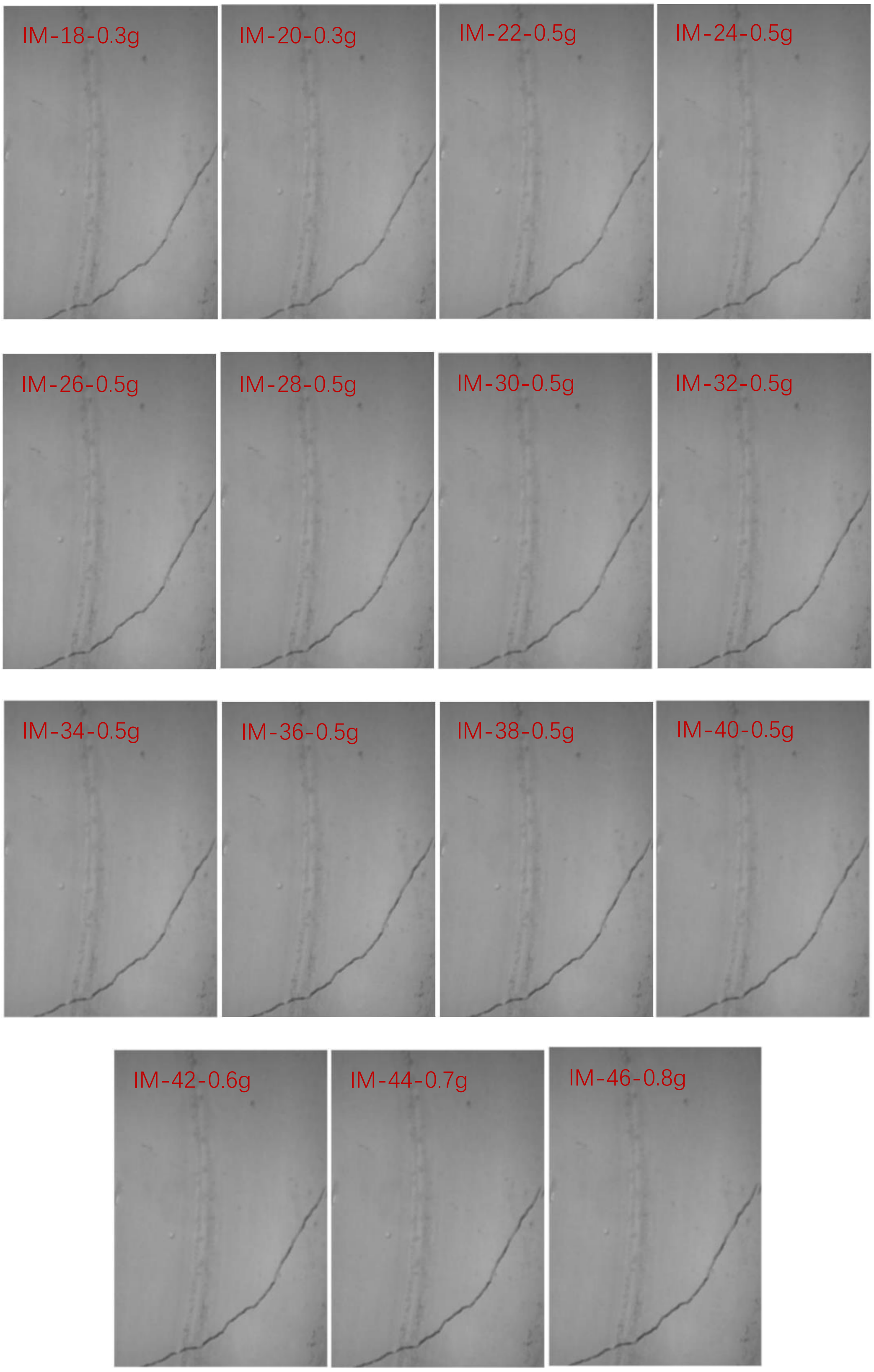

Figure 4.7: Cropped original images of the lining 2 from mini-camera 2-4.


IM-2


IM-4


IM-6


IM-8


IM-10


IM-12


IM-14


IM-16

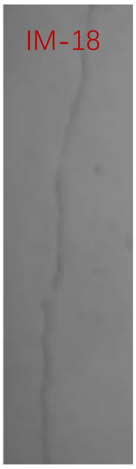
IM-18


IM-20


IM-22


IM-24


IM-26


IM-28


IM-30


IM-32


IM-34


IM-36

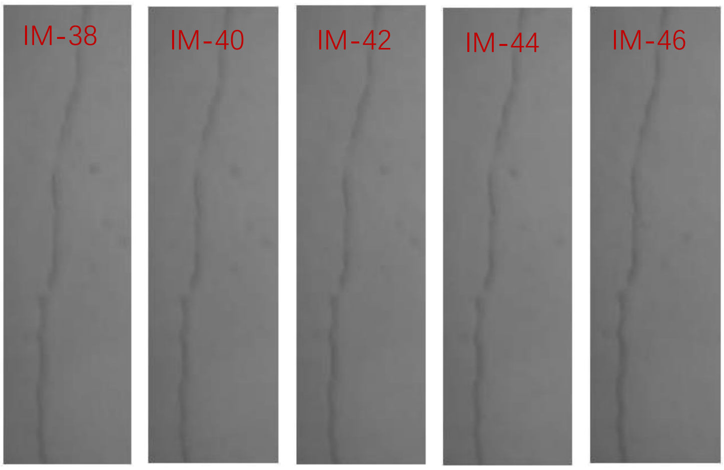

Figure 4.8: Cropped original images of the lining 3 from mini-camera 3-2.

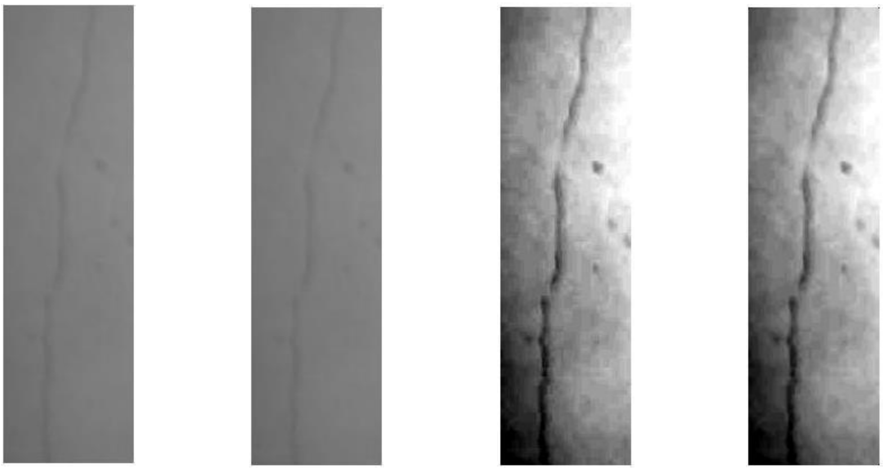

(a) Original image (b) Grayscale image (c) Intensity adjust (d) Median filtering

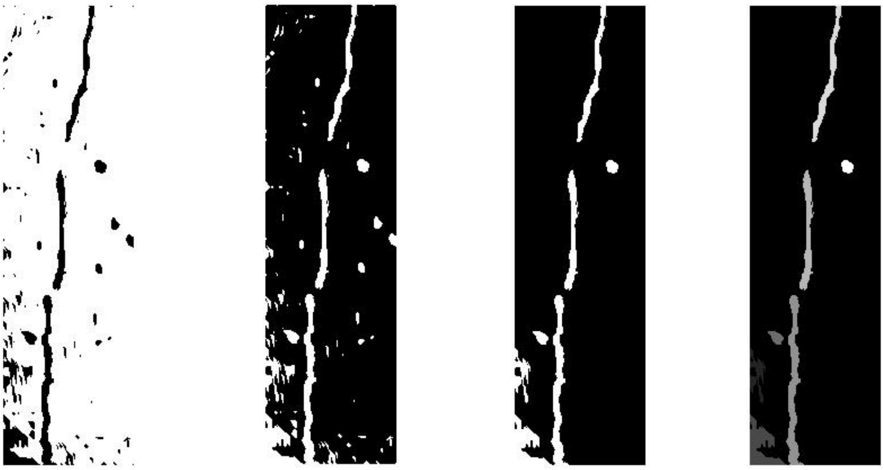

(e) Binary image (f) Negation (g) Area opening operation (h) Labelled

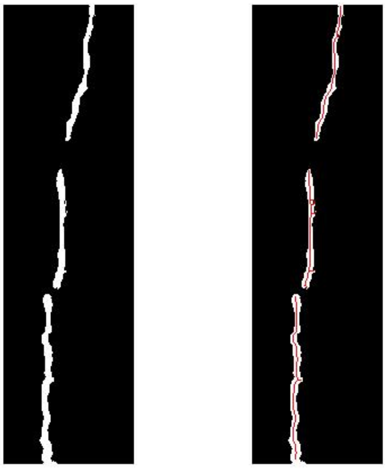

(i) Crack (j) Skeleton

Figure 4.9: Crack extraction of the lining 3 after shaking IM-4.

Figure 4.10 shows the evolution of extracted crack parameters for the lining 2 including the crack average width, area, and length. It could be seen that the results of average width and area showed an obvious upward trend over the course of multiple earthquake shakings, indicating that the status of the lining structure deteriorated continuously. The variation of crack length remained small during the tests. As for the lining 3, the basic laws were almost consistent with that of the lining 2 as shown in Figure 4.11, but the values of average width and area were lower than that of the lining 2. It should be noted that two linings were located in the middle region of the model, therefore the influence of end boundary effects on the tunnel response can be minimized.

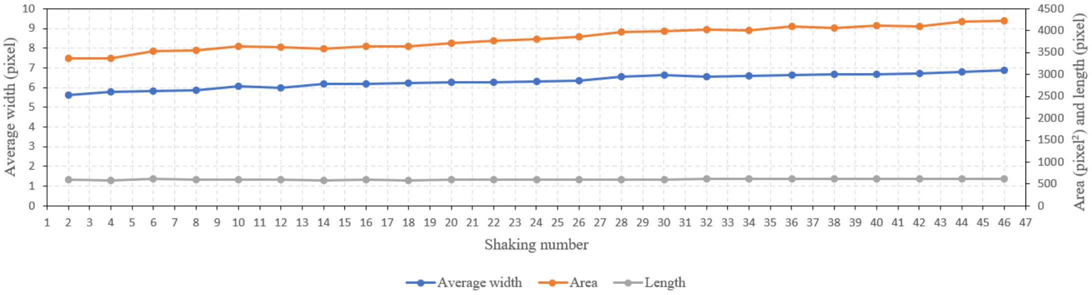

Figure 4.10: Variation of crack average width, area and length for the lining 2.

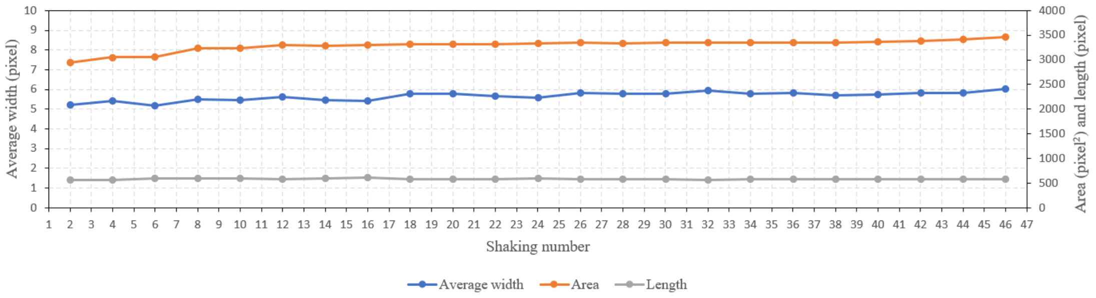

Figure 4.11: Variation of crack average width, area and length for the lining 3.

4.3.3 Damage index

This study attempted to investigate the cumulative effects on the stability of tunnels under earthquakes with the proposed cracking monitoring system. To quantify the level of tunnel damage, a damage index was defined based on the ratio between the area of lining cracks and the area of original image. The relationship between the image-based damage index and the settlement of soil surface was established. Figure 4.12 shows the evolution of damage indexes and the settlements of soil surface for the lining 2. It shows an obvious upward trend during the shaking table tests, indicating that the level of tunnel damage gradually increased. After the first seismic shaking, the damage of the lining occurred and the damage index reached about 0.40 % based on the calculation of residual cracking. From the shaking 2 to 6, there was an obvious increase for the index, which was consistent with the settlement results. Between the shaking 6 to 26, the index results experienced first a slowly and then a dramatically increase, fitting the trend of surface settlement. For the case of the stage ranging from the shaking 26 to 46, the data followed the similar tendency compared to the previous stage. Overall, the trend in the evolution of damage indexes kept similar to that in the progression of surface settlements, implying that the seismically-induced ground failure might play an important role in the seismic response of shallow tunnels. Except for the image-based damage index, the variation of dynamic properties of the tunnel structures could be used for the damage detection, as discussed in Section 4.4. As for the lining 3, the evolution of damage indexes and the settlements of soil surface was shown in Figure 4.13. The basic laws of these results were similar to that of the lining 2.

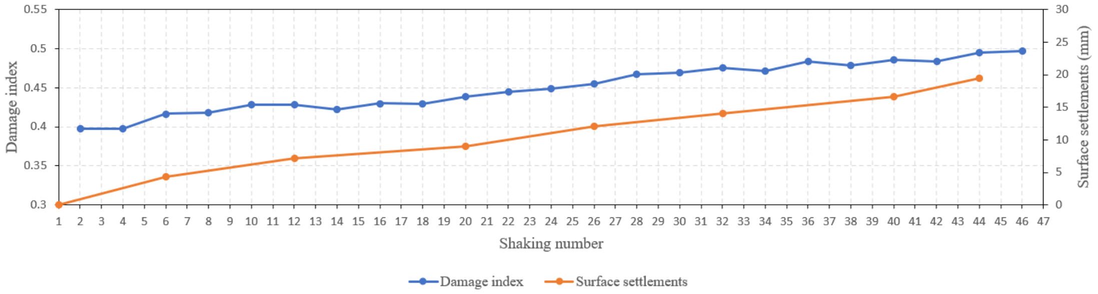

Figure 4.12: Variation of damage index and soil surface settlements for the lining 2.

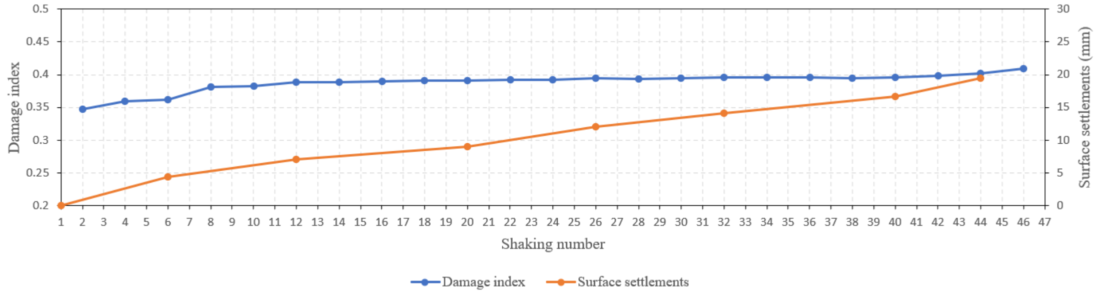

Figure 4.13: Variation of damage index and soil surface settlements for the lining 3.

4.3.4 Observed structural damage

Figure 4.14, Figure 4.15 and Figure 4.16 show the final damage patterns of tunnel lining 1, 2 and 3 respectively. In the lining 1, severe damages occurred such as the longitudinal crack at the crown, longitudinal crack at the sidewall, penetrating crack at the springing, and longitudinal crack at the invert. In the lining 2, significant damages also were observed, for example the longitudinal crack at the crown, longitudinal crack at the invert, inclined crack at the sidewall, and transverse cracks at the lining. As for the lining 3, the longitudinal cracks at the crown, springing, and invert were clear. The damage patterns revealed in this experiment have also been collected in the previous field post-earthquake obervations (Wang et al., 2001; Wang et al., 2009; Li, 2012) and experimental studies (Sun et al., 2011; Wang et al., 2015; Meng et al., 2016; Xin et al., 2019). Normally, the shoulder and springing were the most vulnerable positions in the transversal vibration due to the ovaling deformation mode of tunnel. In addition, to better inspect the lining damages, the external surfaces of the lining 1, 2, 3 were detected before moving the lining structure, as shown in Figure 4.17, Figure 4.18 and Figure

4.19 respectively. The external damages were obvious and appeared at the positions correlating to the observed internal damages. Actually, for the real tunnels, the external surface of tunnel structure could not be inspected in the post-erathquake observations. Alternative methods need to be found to assess its change. In general, this research provides more evidence to the vulnerabilities of tunnels under the muliple earthquakes, which is meaningful to the future seismic design of tunnels.

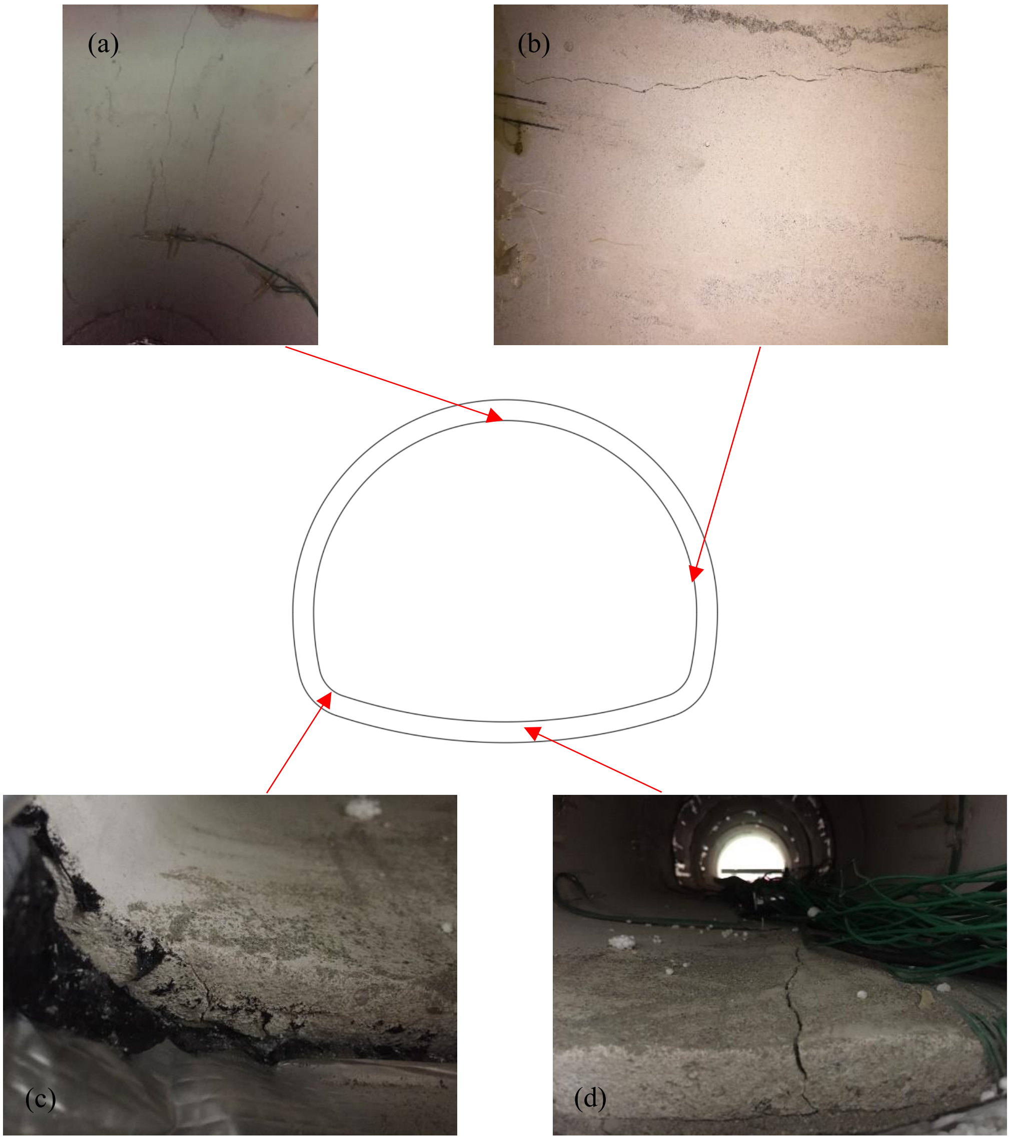

Figure 4.14: Internal damages of lining 1: (a) crown; (b) sidewall; (c) springing; (d) invert.

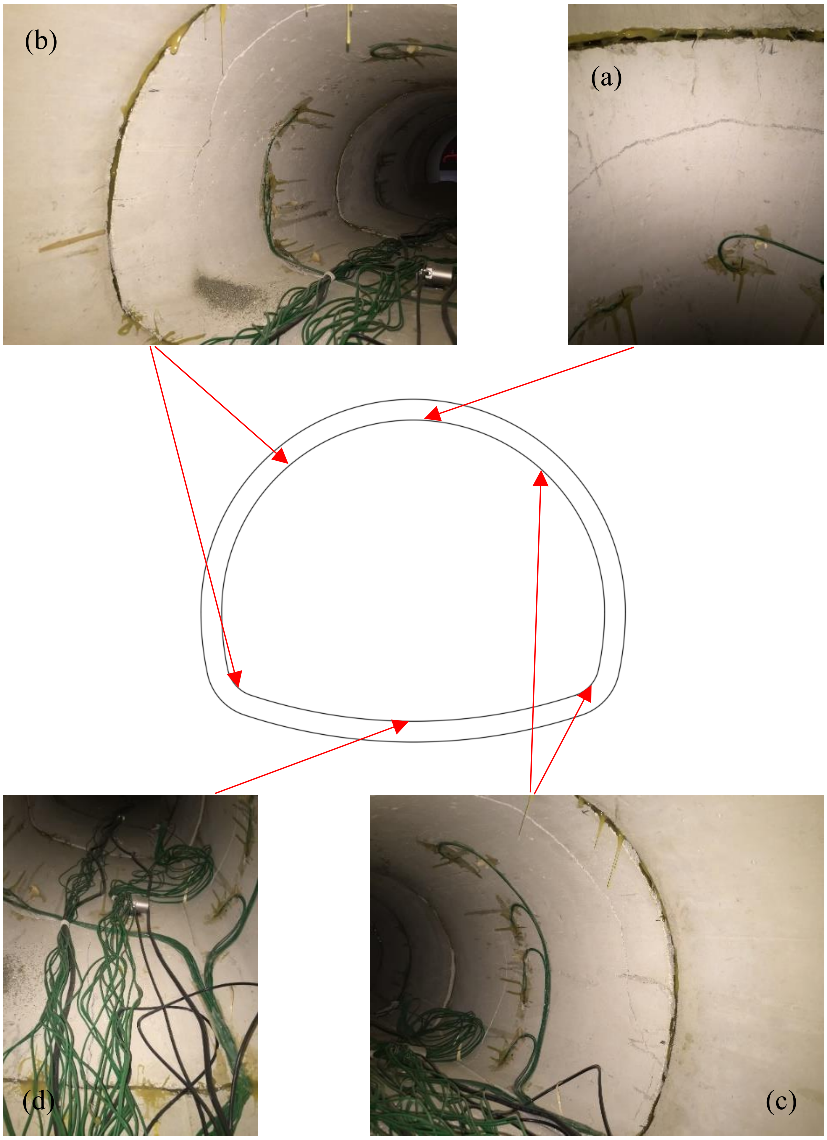

Figure 4.15: Internal damages of lining 2: (a) crown; (b) and (c) springing and shoulder; (d) invert;

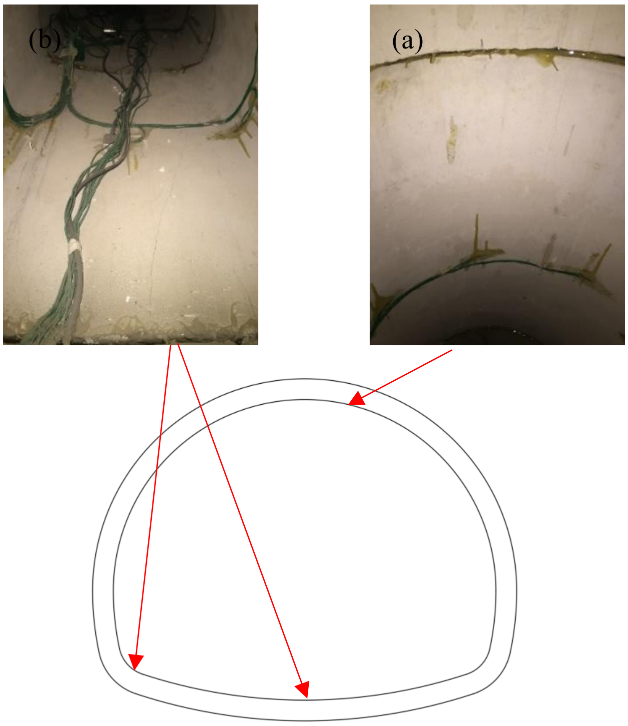

Figure 4.16: Internal damages of lining 3: (a) crown; (b) springing and invert.

(a)

(b)

(c)

Figure 4.17: External damages of lining 1: (a) crown; (b)-(c) sidewall and springing.

(a)

(b)

Figure 4.18: External damages of lining 2: (a)-(b) crown, shoulder, sidewall, and springing.

Figure 4.19: External damages of lining 3.

4.4 Dynamic properties of model structure

As described in Section 3.8, white noise tests were applied after each seismic shaking to track the dynamic properties of the soil-tunnel system. In this section, the natural frequencies and damping ratios of the tunnel structures were extracted from the response signals of accelerometers installed on the lining invert. Then, the variation trend of the identified parameters was discussed.

4.4.1 Model parameter identification methods

4.4.1.1 Natural frequency identification

The natural frequency of structure is identified using synchrosquzzed wavelet transform (SWT) introduced by Daubechies et al (2011). SWT is a powerful tool to sharpen the frequency localization in time-frequency domain by reallocating the wavelet coefficients. It consists of three steps. First, the wavelet coefficients $W_s(a,b)$ of the signal $s(t)$ are calculated with the continuous wavelet transform (CWT),

$$W_s(a,b) = \frac{1}{\sqrt{a}}\int_{-\infty}^{\infty} s(t)\psi^*(\frac{t-b}{a})dt \tag{4.3}$$

Where a and b are the dilation and translation parameters respectively, and ψ^* is the complex conjugate of mother wavelet ψ. In this study, Morlet wavelet is selected for the mother wavelet.

Second, the instantaneous frequency $\omega_s(a,b)$ for the signal $s(t)$ is obtained as the derivative of wavelet coefficients $W_s(a,b)$ at any point (a,b),

$$\omega_s(a,b) = \frac{-i}{W_s(a,b)} \frac{\partial}{\partial b} W_s(a,b) \tag{4.4}$$

Third, the calculated wavelet coefficients $W_s(a,b)$ are reassigned to the time-frequency domain at new points $[\omega_s(a,b), b]$,

$$T_x(\omega_c, b) = (\Delta\omega)^{-1} \sum_{a_k : |\omega(a_k,b) - \omega_c| \leq \Delta\omega/2} W_s(a_k, b) a_k^{-3/2} (\Delta a)_k \tag{4.5}$$

Where $\Delta\omega = \omega_c - \omega_{c-1}$ and $\Delta a = a_k - a_{k-1}$.

Further, the natural frequency f is extracted from the ridges of the time-frequency domain.

4.4.1.2 Damping ratio identification

The damping ratio of structure is calculated from the free-decay response of the signal $s(t)$ produced by white noise excitations. Random decrement technique (RDT) proposed by Cole (1968) is employed to extract this free vibration. RDT is based on the assumption that the response of structure consists of a deterministic part and a random part. An initial condition m, as triggering value, is set to select a sufficient number of samples followed by the operation of averaging. It is estimated as follows (Rodrigues and Brincker, 2005),

$$m = \sqrt{2}\sigma_s \tag{4.6}$$

Where σ_s is the standard deviation of signal $s(t)$.

Therefore, the random component is removed, and the free-decay response $x(t)$ with the deterministic part is obtained. The envelop $z(t)$ of decaying response can be generated by using Hilbert transform (Hilbert, 1912) which is defined as follows,

$$H[x(t)] = \frac{1}{\pi}\int_{-\infty}^{\infty}\frac{x(\tau)}{t-\tau}d\tau \tag{4.7}$$

An analytic signal is created by coupling $x(t)$ and $H[x(t)]$as follows,

$$z(t) = x(t) + iH[x(t)] \tag{4.8}$$

Then, a simple exponential function is fitted to the envelop of the free-decay response,

$$y = Ae^{-Bt} \tag{4.9}$$

The damping ratio is estimated by,

$$\xi = \frac{B}{\omega_n} \tag{4.10}$$

Where ω_n is the eigen frequency.

4.4.2 Variation of natural frequencies

In this study, after the white noise tests, the SWT method was utilized to extract the first natural frequency from the acquired acceleration signal at the tunnel invert. As the example, Figure 4.20 (a) shows the SWT scalogram for the lining 2 at the IM-1 and Figure 4.20 (b) describes the corresponding power of coefficients and frequency plot. The first natural frequency was then extracted from the ridge (highest peak). The evolution of the damage indexes and the identified first natural frequencies for the lining 2 was shown in Figure 4.21. The results indicated that after the initial seismic shaking, the dominant frequency had a significant decrease, from 12.11 Hz to 11.27 Hz. Considering the damage index result about 0.40 %, the non-linear seismic responses occurred at this stage and the stiffness of the structure was reduced. From the shaking 3 to 7, the frequency remained unchanged, however the damage indexes had an upward trend, which may be caused by the combined effects of the soil shear deformation and ground settlement. Between the shaking 7 to 45, the frequency first increased to 11.43 Hz and then remained constant, which corresponded to the growing of damage index. It seems that the structure vibrated at higher frequencies when the damage had occurred. This observation could be reminiscent of what was previously seen in the structural engineering like building, namely structural resurrection phenomena (Vamvatsikos and

Cornell, 2002). For this underground structure surrounded by the ground, it might be attributed to the influence of the soil settlements, apart from the soil shear deformation. As for the shaking 47 which was after the seismic shaking with an amplitude of 0.8 g, the natural frequency decreased to 11.27 Hz eventually. At this moment, it could be judged that the severe cumulative damage of the lining came up and the densification of the soil tended to be stable. Overall, under the combined effects of the soil shear deformation and ground settlement, the frequency shifting behaviour, in the course of multiple earthquake shakings, did not follow the simple pattern, where a reduction in natural frequencies is expected when structural damage occurs like Wang et al. (2015). This unconventional dynamic behaviour provides an insight to better understand the resilience and life-long performance of earthquakes exposed underground structures. As for the lining 3, the variation of damage indexes and the first natural frequencies was presented in Figure 4.22. The basic laws of these results were similar to that of the lining 2.

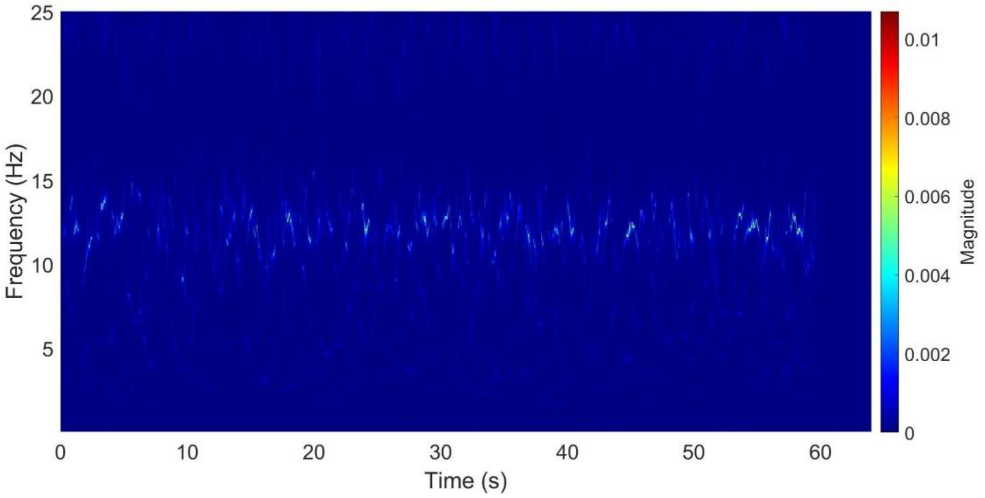

(a) SWT scalogram

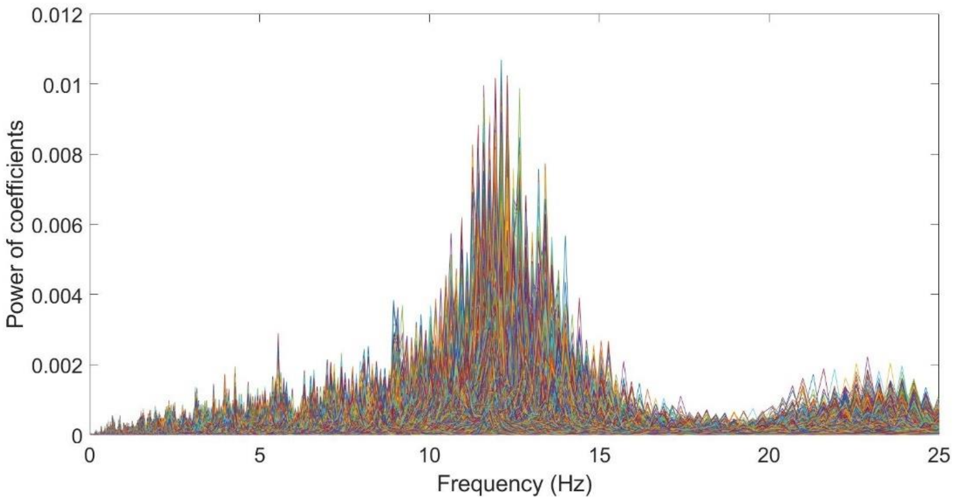

(b) Power of coefficients vs frequency plot

Figure 4.20: Time-frequency analysis for lining 2 at IM-1.

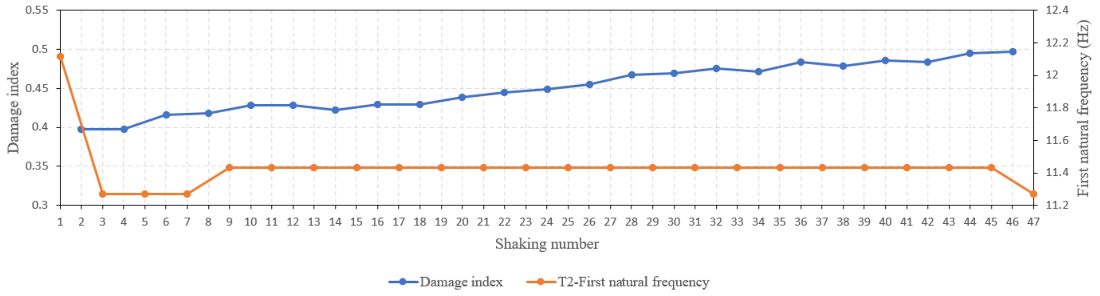

Figure 4.21: Variation of damage index and first natural frequency for the lining 2.

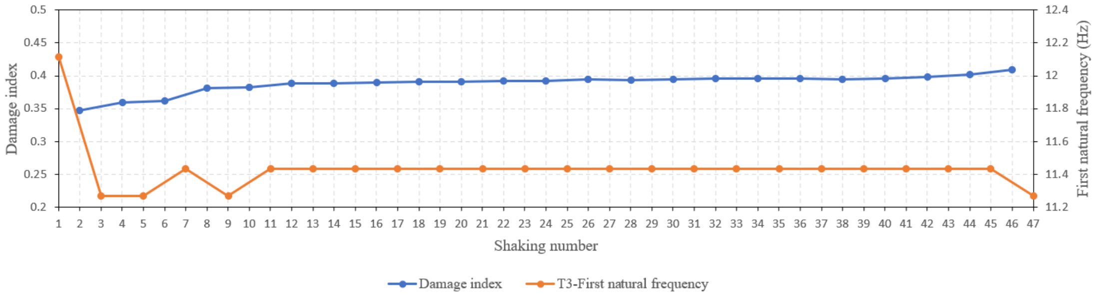

Figure 4.22: Variation of damage index and first natural frequency for the lining 3.

4.4.3 Variation of damping ratios

By using the RDT, the free-decay response of the measured acceleration signals could be obtained. As the example, Figure 4.23 shows the free-decay response for the lining 2 at the IM-1. Based on the Hilbert transform and exponential fitting, the damping ratios were calculated. The evolution of the damage indexes and damping ratios for the lining 2 was shown in Figure 4.24. At the IM-3 stage, the value of damping ratio decreased remarkably, from 8.73% to 7.47%, indicating that structural damages resulted in the reduction of damping ratio. Subsequently, with the increasing of the damage index of the lining, damping ratios had a downward trend, followed by a relatively stable period. After the IM-33, there was an upward trend for the structural damping ratios ending at 7.46%. It should be noted that the variation trend of damping ratios resulted from the combined effects of the soil shear deformation and ground settlement. In addition, the results of the lining 3 were similar to that of the lining 2, as shown in Figure 4.25.

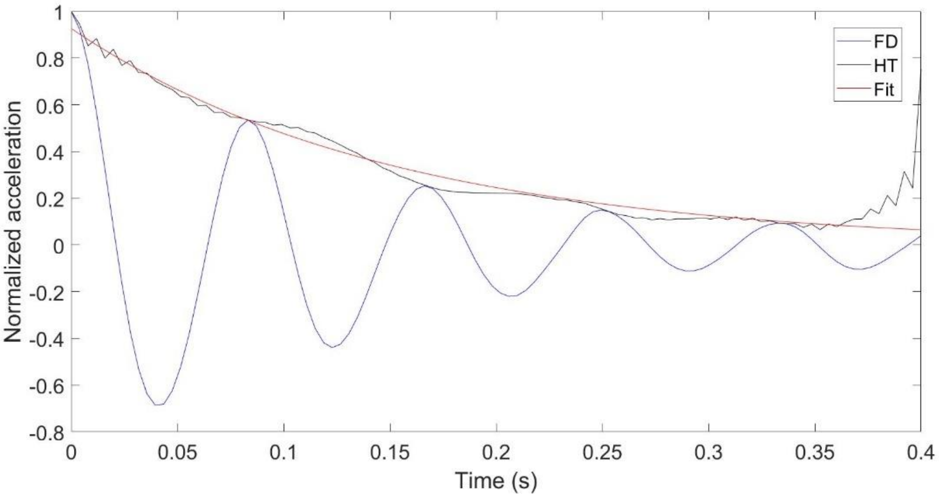

Figure 4.23: Free-decay response estimations for the lining 2 at IM-1. FD: Free-decay response; HT: Hilbert transform; Fit: Fitting.

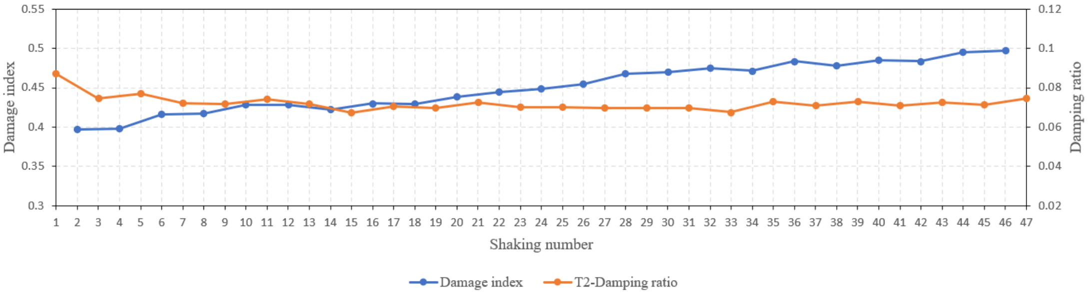

Figure 4.24: Variation of damping ratio for the lining 2.

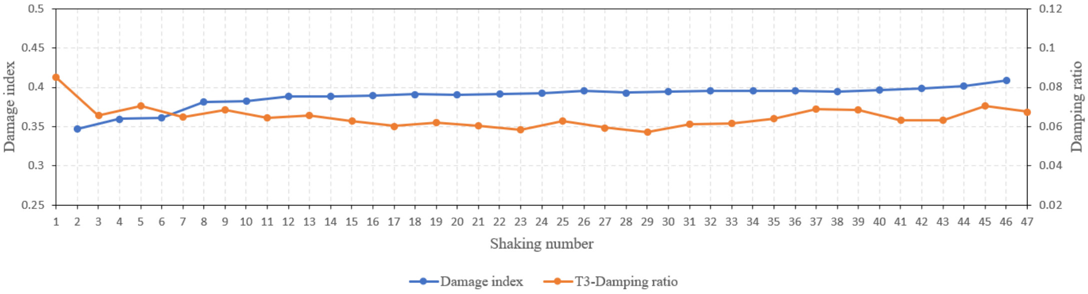

Figure 4.25: Variation of damping ratio for the lining 3.

4.5 Acceleration amplification factors

The arrangement of accelerometers in the soil-tunnel and free-field models was shown in Figure 3.30 and Figure 3.31 respectively. This section highlighted the acceleration amplification factors of the tunnel and soil in the course of multiple seismic actions. The acceleration amplification factor was defined as the ratio of peak acceleration of accelerometers in the model box to peak value of accelerometers on the shaking table. In addition, the FFT was used to analyze the acceleration response data.

4.5.1 Soil response

When the seismic wave propagates in the ground, the soil deposits could amplify the seismic motion through the soil column toward the surface (Kramer, 1996). This site amplification effect has been investigated in the previous shaking table tests of tunnels (Sun et al., 2011; Wang et al., 2015; Xin et al., 2019; Yang et al., 2021). Generally, it was observed that the amplification effect of the ground decreased with the increasing of the amplitude of input motions due to the soil non-linearity behaviour. This study explored the site amplification effect, considering the combined effects of the soil shear deformation and ground settlement. Also, the influence of the presence of tunnel on the ground response was considered.

Figure 4.26 shows the evolution of acceleration amplification factors in the left section of the soil-tunnel model. The left section involved the two vertical arrays of soil accelerometers. They were located at three elevations; AA1 and AA2 were installed at the ground level, AA3 was placed at the crown level, and AA4 was at the invert level. The results indicated that the acceleration amplification factors increased with the increasing of the elevation for all earthquake shakings. Although AA1 and AA2 located at the same elevation, the factors of AA2 were always larger than that of AA1, which might be due to the impact of the tunnel presence. Moreover, it could be seen that the factors had a downward trend with the increasing of the seismic intensity due to the soil non-linearity and stiffness degradation. However, the values of AA4 showed an opposite tendency when entering the 0.5 g stage because the characteristic of surrounding soil was not fully reflected at this height. In addition, it could be found that from the initial shaking 2 to shaking 6, the amplification factors of three accelerometers (i.e. AA1, AA2 and AA3) significantly increased, which was caused by the quick development of soil settlements. Subsequently, the factors indicated a slight increase during the remaining shakings of 0.3 g stage. Overall, the amplification factors were influenced by the combined effects of the soil shear deformation and ground settlement during the whole process. The degree depended on which effect played a dominant role.

Figure 4.27 shows the evolution of acceleration amplification factors in the left section of the free-field model. The left section involved the two vertical arrays of soil accelerometers. They were located at three elevations; BA9 and BA10 were installed at the ground level, BA17 and BA11 were placed at the crown level, and BA16 and BA 12 were at the invert level. The basic laws were consistent with that of the soil-tunnel model. It could be observed that at the same elevation (crown or invert level), the amplification factors of accelerometers agreed well during almost the whole process, indicating the effectiveness of the geofoam boundary and the uniformity of the sand ground. Also, the difference between BA9 and BA10 was still found, probably because the ground surface was lack of the confinement of the surrounding soil. Compared to the results of ground level in the soil-tunnel model, this difference decreased due to without the influence of the tunnel.

In order to further observe the influence of the tunnel presence on the soil response, the results of two models were put together, as shown in Figure 4.28. It could be seen that at the same elevation, the acceleration amplification factors in two models matched well except for the local cases. This finding demonstrated that the geofoam boundaries in two models were effective to prevent the reflections and refractions of seismic waves, the preparation of two models were successful, and the influence of the tunnel presence on the soil response was very limited.

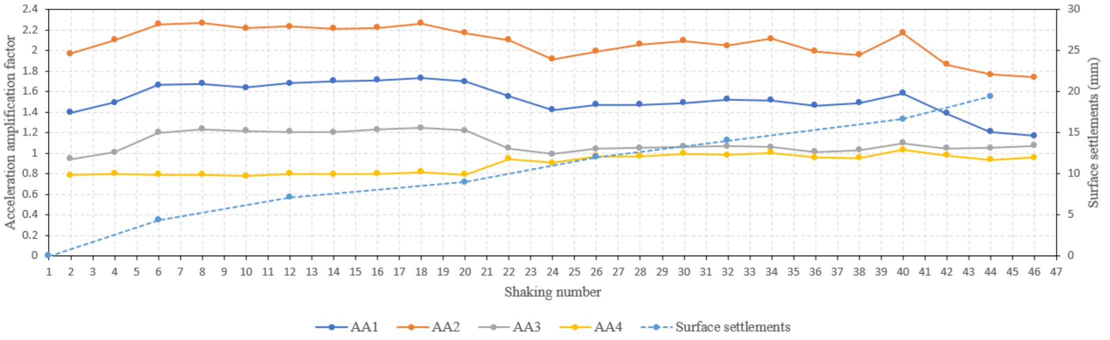

Figure 4.26: Variation of acceleration amplification factors in left section of soil-tunnel model.

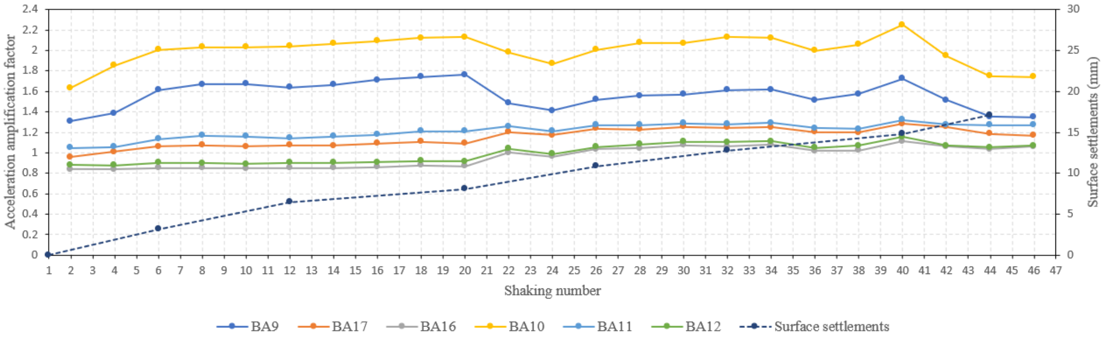

Figure 4.27: Variation of acceleration amplification factors in left section of free-field model.

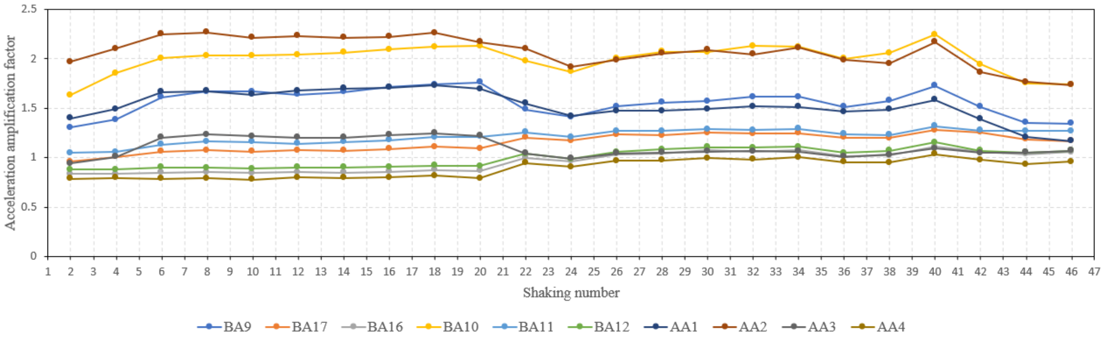

Figure 4.28: Variation of acceleration amplification factors in left section of soil-tunnel model and free-field model.

Acceleration amplification factors were calculated based on the time history results. In order to obtain a further understanding of the amplification effects, the FFT at the monitoring points was calculated. Figure 4.29 shows the accelerometer FFT results for the left section in IM-2-0.3g and other typical cases are given in Appendix. In each figure, the left column represented the results of the free-field model, while the right column presented the results of the soil-tunnel model. It could be seen that Fourier amplitude increased from the shaking table surface to the ground level, and the trend of amplification was obvious. The Fourier amplitudes were nearly identical at the same elevation of two models, which was consistent with the results of acceleration amplification factors. Moreover, it was evident that the high-frequency content was lost when the seismic waves cross the tunnel by comparing the Fourier spectrum of ground level accelerometers (BA9, BA10, AA1 and AA2), indicating that the presence of tunnel had an impact on the soil response. Such frequency loss was also observed in the previous studies (Sun et al., 2011; de Silva et al., 2021). In addition, the status of soil accelerometer after the tests was shown in Figure 4.30. This was the profile of the sand ground, perpendicular to the vibration direction. It could be observed that the accelerometer almost did not twist during the ground deformations, indicating that the design of the box of polymethyl methacrylate was effective.

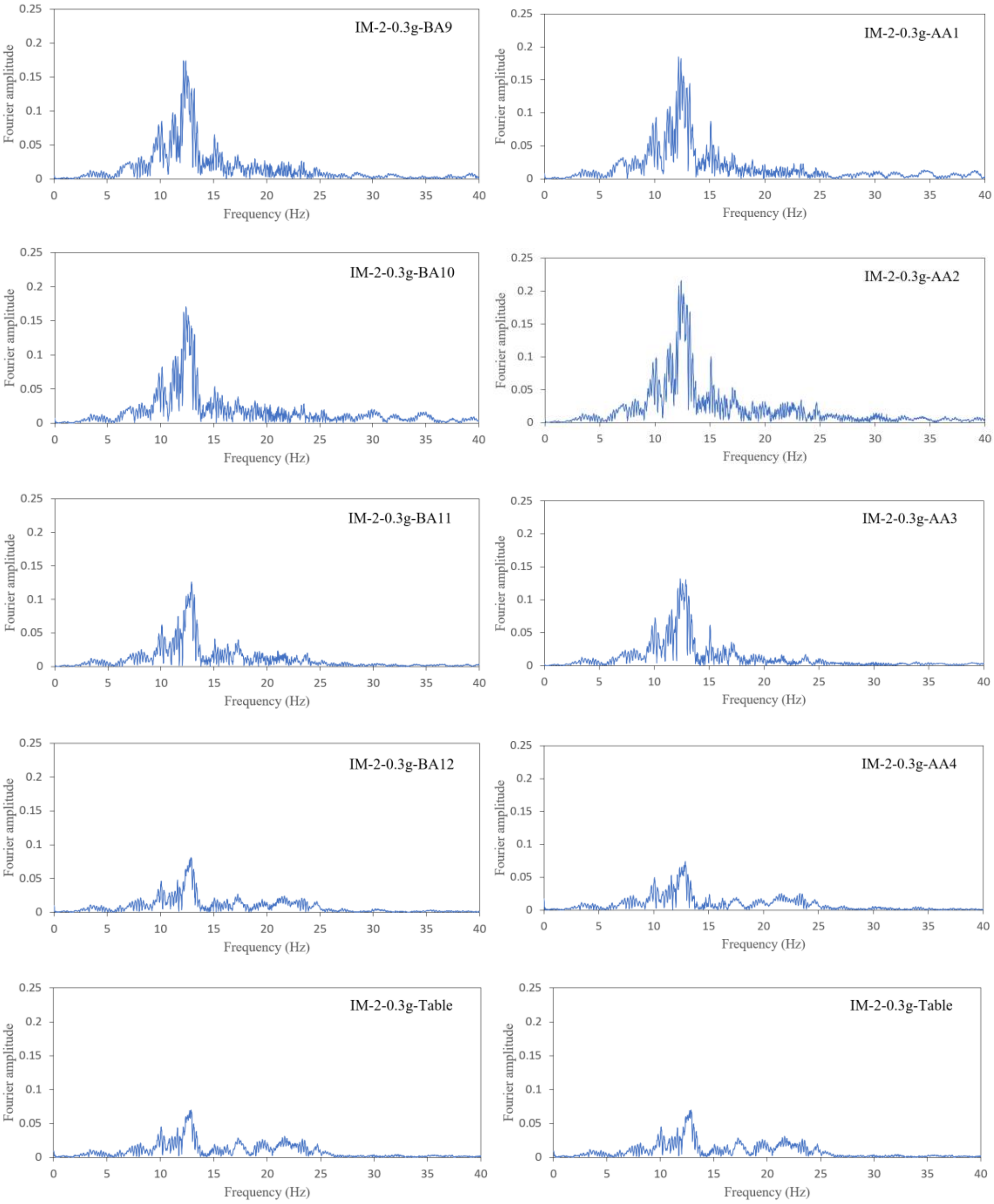

Figure 4.29: FFTs of soil accelerometers in IM-2-0.3g.

Figure 4.30: Status of soil accelerometer after the tests.

4.5.2 Structure response

The seismic response of tunnels is different from that of above ground structures, since kinematic loading induced by the surrounding ground plays an important role compared to inertial loads resulting from the vibration of the tunnel itself (Wang 1993; Hashash et al., 2001). Therefore, the traditional view was that the response of tunnel structures follows the response of surrounding soil. In this section, the variation of acceleration amplification factors on the tunnel invert of the soil-tunnel model was investigated, considering the combined effects of the soil shear deformation and ground settlement, as shown in Figure 4.31. It could be seen that the trends of amplification factors on the three lining sections were almost consistent with that of the soil accelerometer at the same elevation. From the shaking 2 to 8, the values exhibited an upward trend, which might result from the quick densification of the relatively loose sand ground. Between the shaking 8 to 20, the values tended to be stable with the settlement rate reduced. From the shaking 20 to 26, with the increasing of the seismic intensity (0.5 g), the amplification factors significantly increased, which was consistent with the trend of the ground settlements. Between the shaking 26 to 40, the factors tended to be stable, but had slight fluctuations due to the development of soil non-linearity. From the shaking 40 to 46, with the increasing of earthquake intensity (0.6 g, 0.7 g and 0.8 g), the amplification factors of tunnel structures had an upward trend, but the opposite results were observed on soil accelerometer. This might be caused by the development of tunnel damages and ground deformations. Overall, the variation of acceleration amplification factors of the tunnel lining was almost consistent with that of the soil accelerometer, when taking into account the combined effects of the soil shear deformation and ground settlement. The ground settlement could significantly influence the seismic response of tunnel structures. Also, the amplification factors increased with the increase of seismic intensity, which contrasted with the results of Wang et al. (2015) that the amplification factors decreased with the progressive increase of input intensity. The authors considered the shear deformation of surrounding rock and employed the unreinforced tunnel lining.

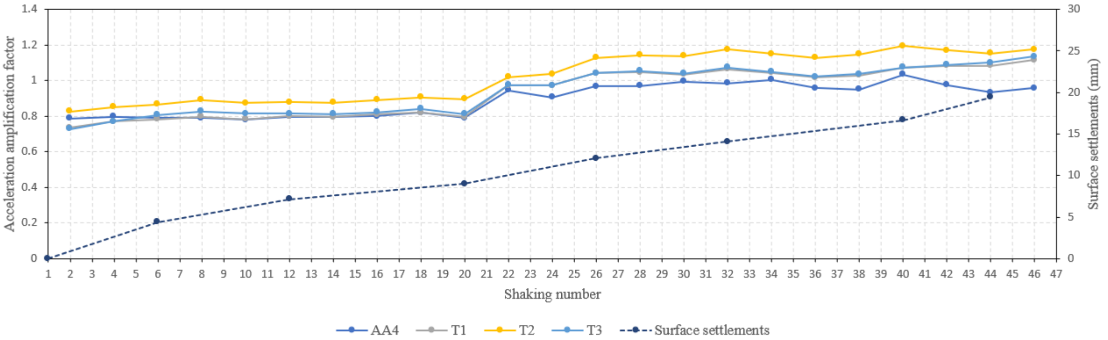

Figure 4.31: Variation of acceleration amplification factors on the tunnel invert.

4.6 Strain of model structure

The arrangement of strain gauges on the model structures was shown in Figure 3.33. The seismic lining strain was defined as the dynamic incremental strain above the static strain. Generally, it was observed that the shoulder and springing were the vulnerable positions in the transversal section of tunnel structures due to the ovaling deformation mode (Xin et al., 2014; Wang et al., 2015; Xin et al., 2019; Yang et al., 2021; Xu et al., 2022). Therefore, this section focused on the seismic response of shoulder and springing of the tunnel, considering the combined effects of the soil shear deformation and ground settlement. Figure 4.32 shows the variation of maximum seismic strain of the tunnel lining 3 in the course of multiple earthquake shakings. It could be seen that the tensile strains at the monitoring positions continuously increased during the shaking until the strain gauges were broken. The strain of springing was larger than the value of shoulder due to the stress concentration at the connection of invert and sidewall. The variation trends of two positions were consistent with the trend of the surface settlements, implying that the ground settlement played an important role on the seismic response of tunnel structures. Moreover, the variation trend of springing strains fitted to the trend of damage index results discussed in Section 4.3.3, indicating the accuracy of image processing.

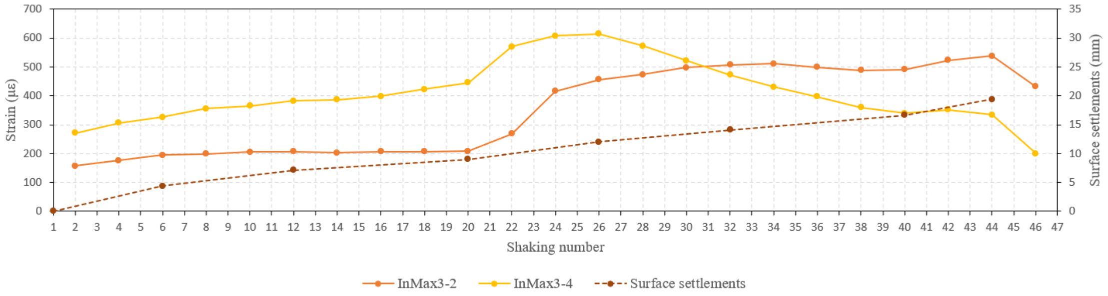

Figure 4.32: Variation of maximum seismic strains of the tunnel lining 3.

4.7 Conclusion

In the second section, the ground deformations of the soil-tunnel and free-field models were discussed based on the 3D point cloud datasets and the post-earthquake observations. Firstly, the average registration error was lower than 1 mm, which can meet the accuracy of exploring surface elevation changes during the dynamic experiments. Secondly, the M3C2 algorithm was applied to measure surface elevation changes in this study. The densification effects of sand could be observed in the two model boxes simultaneously and the influence of tunnel presence on the soil response was restricted in the limited region which was within around 1.5D-2D in the transversal direction. In addition, the tunnel ends could slightly influence the soil response around the local areas, but it did not interfere the observation in the middle region. Also, it was clear that the response of tunnels not only resulted from the soil shear deformation, but also the ground settlement. The combined effects of them may heavily damage the tunnel, which could be reflected by the results of structural damage. Thirdly, the volumetric changes were estimated with the significant surface elevation changes (M3C2 with $LOD_{95\%}$) for seven simulations, and the results were compared to the estimations using the DoD and M3C2 without $LOD_{95\%}$ methods. It was found that the estimations of the DoD method were close to that of the M3C2 without $LOD_{95\%}$ method in both models, implying that the advantage of the M3C2 on the exhibition of different characteristic scales disappeared. Also, these two methods highly overestimated the volumetric changes compared to the M3C2 with $LOD_{95\%}$ method, owing to that $LOD_{95\%}$ can separate non-significant changes from the calculations considering the uncertainties from surface roughness, position uncertainty, and registration error. Furthermore, through the post-earthquake observations, it could be observed that the surface settlements in two models were obvious, and the values were almost consistent with the detections by the 3D point cloud technology, indicating that the M3C2 algorithm was accurate.

In the third section, the structural damages are discussed according to the image data and post-earthquake observations. Firstly, once the images of lining surface were acquired using the proposed cracking monitoring system, lining cracks were identified and measured according to the image processing techniques. It could be seen that the results of average width and area showed an obvious upward trend over the course of multiple earthquake shakings, indicating that the status of the tunnel structure deteriorated continuously. Secondly, to quantify the level of tunnel damage, a damage index was defined based on the ratio between the area of lining cracks and the area of original image. The relationship between the image-based damage index and the settlement of soil surface was established. The trend in the evolution of damage indexes kept similar to that in the progression of surface settlements, implying that the seismically-induced ground failure might play an important role in the seismic response of shallow tunnels. Except for the image-based damage index, the variation of dynamic properties of the tunnel structures could be used for the damage detection. Thirdly, the damage patterns revealed in this experiment have also been collected in the previous field post-earthquake observations and experimental studies. Normally, the shoulder and springing were the most vulnerable positions in the transversal vibration due to the ovaling deformation mode of tunnel. This research provides more evidence to the vulnerabilities of tunnels under the multiple earthquakes, which is meaningful to the future seismic design of tunnels.

In the fourth section, the variation of dynamic properties of tunnel structures is presented. Under the combined effects of the soil shear deformation and ground settlement, the frequency shifting behaviour, in the course of multiple earthquake shakings, did not follow the simple pattern, where a reduction in natural frequencies is expected when structural damage occurs like Wang et al. (2015). Moreover, it was seen that the structural damages resulted in the reduction of damping ratio, but when the structural status continuously deteriorated, an upward trend for structural damping ratios was observed. It should be noted that the variation trend of damping ratios resulted from the combined effects of the soil shear deformation and ground settlement. This unconventional dynamic behaviour provides an insight to better understand the resilience and life-long performance of earthquakes exposed underground structures.

In the fifth section, the acceleration amplification factors of soil and tunnel in the course of multiple seismic actions are presented. For the seismic response of the soil, it was observed that the acceleration amplification factors increased with the increasing of the elevation for all earthquake shakings, and the amplification effect of the ground decreased with the increasing of the amplitude of input motions due to the soil non-linearity behaviour. The amplification factors were influenced by the combined effects of the soil shear deformation and ground settlement during the whole process. The degree depended on which effect played a dominant role. Moreover, it could be seen that at the same elevation, the acceleration amplification factors in two models matched well except for the local cases. This finding demonstrated that the geofoam boundaries in two models were effective to prevent the reflections and refractions of seismic waves, the preparation of two models were successful, and the influence of the tunnel presence on the soil response was very limited. In addition, it could be seen that the Fourier amplitude in two models increased from the shaking table surface to the ground level, and the trend of amplification was obvious. It was evident that the high-frequency content was lost when the seismic waves cross the tunnel by comparing the Fourier spectrum of ground level accelerometers, indicating that the presence of tunnel had an impact on the soil response. For the seismic response of the tunnel, the variation of acceleration amplification factors of the tunnel lining was almost consistent with that of the soil accelerometer, when taking into account the combined effects of the soil shear deformation and ground settlement. The ground settlement could significantly influence the seismic response of tunnel structures. Also, the amplification factors increased with the increase of seismic intensity, which contrasted with the results of Wang et al. (2015) that the amplification factors decreased with the progressive increase of input intensity.

In the sixth section, the maximum seismic strains of tunnel lining are studied using the strain data at the monitoring positions. It could be seen that the tensile strains at the monitoring positions continuously increased during the shaking until the strain gauges were broken. The strain of springing was larger than the value of shoulder due to the stress concentration at the connection of invert and sidewall. The variation trends of two positions were consistent with the trend of the surface settlements, implying that the ground settlement played an important role on the seismic response of tunnel structures. Moreover, the variation trend of springing strains fitted to the trend of damage index results, indicating the accuracy of image processing.

Overall, the findings are a precursor to better understand the resilience and life-long performance of earthquake exposed underground structures. They can support, as validating data, the development of means to replicate the non-classical soil-structure interaction mechanisms that pertain when cumulative earthquake load is applied, and subsequently lead to unconventional dynamic behaviour. These are important to assess the health condition of operational tunnel and provide timely and necessary rehabilitation. Furthermore, there is a pressing need to investigate the cumulative effect of earthquakes on actual monitored tunnels, which could allow us to fully understand such effect and verify the presented results.

Chapter 5 Conclusions and Future work

In this last chapter, the conclusions drawn from the previous chapters are summarized in Section 5.1, and recommendations for future work are presented in Section 5.2.

5.1 Conclusions

The aims of this research were to experimentally examine the performance of tunnel structures in the transversal direction over the course of multiple earthquake shakings, and to examine the effect of tunnel presence on the soil response, namely analyze soil-structure interaction effects. In order to achieve these aims, two model systems were employed simultaneously during the shaking table tests, one with the tunnel and the other without the tunnel.

In Chapter 2, a comprehensive review was provided to understand the seismic damage characteristics of tunnels based on post-earthquake observations, the application of shaking table technology on cumulative damage of tunnels, and the methods about quantifying the damage both on the tunnel and the surrounding ground. Firstly, although many experimental and numerical studies focused on the behaviour of tunnels under single earthquakes or under seismic excitations with increasing intensities, the cumulative effect of multiple seismic events is not well-understood within an earthquake prone region. Secondly, four derived similitude rules were used in previous 1 g shaking table tests of underground structures, including elastic-gravity similarity law, elastic similarity law (gravity distortion method), artificial mass method, and general similarity law (less artificial mass method). Their limitation is that using existing similitude rules to simulate the tunnel lining cannot guarantee the similitude of structural nonlinear behaviour. Also, the quantitative analysis of lining cracks (e.g. average width, length and area) and ground deformations (e.g. volume) need to be further explored. Thirdly, four main approaches were used to measure surface elevation changes between multi-temporal point cloud datasets, including DoD, C2C, C2M and

M3C2. M3C2 algorithm has been widely used on soil erosion, landslides and rockfalls, due to its accuracy. Furthermore, due to the low and uneven lighting, serious noise, and background interference of tunnel environment, crack monitoring systems need to be individually designed to capture the high-quality image data, and the crack identification and measurement need to be realized with suitable methods. Finally, in order to quantify the level of tunnel damage, damage indexes or levels were used in the previous studies. Quantitative damage indexes were traditionally determined by the demand-capacity ratios of structural response parameters, while qualitative methods in the literature described the performance of tunnel lining according to the visual signs of distress. Both were proposed based on the response of tunnels following an earthquake, and their performance in the literature indicated the obvious differences. Also, the seismically-induced ground failure was not included in the previous studies.

In Chapter 3, the experimental models used in this research were presented. The shaking table facility at NEDL is used. The size of testing platform is 10 m × 8 m and the frequency range is 0.1-50 Hz. The dimension of two equivalent model boxes is 2.5 m length, 2.5 m width, and 2.0 m height. EPS geofoams with thickness of 15 cm as absorbing boundaries are placed on the inner sides of containers to reduce the reflections and refractions of seismic waves during the tests. A layer of gravel with thickness of 30 mm was glued at the bottom of the model boxes to increase the friction between ground and model container. Also, the elastic similarity relations derived by the Buckingham-π theorem and the equation (3-7) obtained based on two dimensionless parameters s and N_P are combined together to investigate the seismic response of tunnel structures. Moreover, the uniaxial compression tests and four-point bending tests were conducted to find the appropriate mix proportion of microconcrete, namely cement, slaked lime, river sand, and water with weight ratio of 0.8: 0.8: 6: 2.4. 316 stainless steel wire with diameter 0.2 mm was selected as the model reinforcement and its strength and elongation were measured by the tensile tests. The dry river sand in Sichuan province was adopted to model the ground surrounding the tunnel, and the sand properties were measured by sieve analysis, compaction tests, funnel method, pycnometer tests and direct shear tests. Furthermore, four types of sensors were installed, including accelerometers placed for measuing accelerations of sand mass, structure and shaking table, strain gauges adopted for measuring bending strains of structure, 3D laser scanner used for estimating ground deformations, and mini-cameras used for recording the evolution of tunnel damage. Finally, Wolong record EW component from the M8.0 2008 Wenchuan earthquake was selected as the test input signal. In order to diagnose the variation of system dynamic properties, white noise tests were conducted before and after each seismic shaking.

In Chapter 4, the results of the shaking table test program were presented. In the second section, the ground deformations of the soil-tunnel and free-field models were discussed based on the 3D point cloud datasets and the post-earthquake observation. Firstly, the average registration error was lower than 1 mm, which can meet the accuracy of exploring surface elevation changes during the dynamic experiments. Secondly, the M3C2 algorithm was applied to measure surface elevation changes in this study. The densification effects of sand could be observed in the two model boxes simultaneously and the influence of tunnel presence on the soil response was restricted in the limited region which was within around 1.5D-2D in the transversal direction. In addition, the tunnel ends could slightly influence the soil response around the local areas, but it did not interfere the observation in the middle region. Also, it was clear that the response of tunnels not only resulted from the soil shear deformation, but also the ground settlement. The combined effects of them may heavily damage the tunnel, which could be reflected by the results of structural damage. Thirdly, the volumetric changes were estimated with the significant surface elevation changes (M3C2 with $LOD_{95\%}$) for seven simulations, and the results were compared to the estimations using the DoD and M3C2 without $LOD_{95\%}$ methods. It was found that the estimations of the DoD method were close to that of the M3C2 without $LOD_{95\%}$ method in both models, implying that the advantage of the M3C2 on the exhibition of different characteristic scales disappeared. Also, these two methods highly overestimated the volumetric changes compared to the M3C2 with $LOD_{95\%}$ method, owing to that $LOD_{95\%}$ can separate non-significant changes from the calculations considering the uncertainties from surface roughness, position uncertainty, and registration error. Furthermore, through the post-earthquake observation, it could be observed that the surface settlements in two models were obvious, and the values were almost consistent with the detections by the 3D point cloud technology, indicating that the M3C2 algorithm was accurate.

In the third section, the structural damages are discussed according to the image data and post-earthquake observations. Firstly, once the images of lining surface were acquired using the proposed cracking monitoring system, lining cracks were identified and measured according to the image processing techniques. It could be seen that the results of average width and area showed an obvious upward trend over the course of multiple earthquake shakings, indicating that the status of the tunnel structure deteriorated continuously. Secondly, to quantify the level of tunnel damage, a damage index was defined based on the ratio between the area of lining cracks and the area of original image. The relationship between the image-based damage index and the settlement of soil surface was established. The trend in the evolution of damage indexes kept similar to that in the progression of surface settlements, implying that the seismically-induced ground failure might play an important role in the seismic response of shallow tunnels. Except for the image-based damage index, the variation of dynamic properties of the tunnel structures could be used for the damage detection. Thirdly, the damage patterns revealed in this experiment have also been collected in the previous field post-earthquake observations and experimental studies. Normally, the shoulder and springing were the most vulnerable positions in the transversal vibration due to the ovaling deformation mode of tunnel. This research provides more evidence to the vulnerabilities of tunnels under the multiple earthquakes, which is meaningful to the future seismic design of tunnels.

In the fourth section, the variation of dynamic properties of tunnel structures is presented. Under the combined effects of the soil shear deformation and ground settlement, the frequency shifting behaviour, in the course of multiple earthquake shakings, did not follow the simple pattern, where a reduction in natural frequencies is expected when structural damage occurs like Wang et al. (2015). Moreover, it was seen that the structural damages resulted in the reduction of damping ratio, but when the structural status continuously deteriorated, an upward trend for structural damping ratios was observed. It should be noted that the variation trend of damping ratios resulted from the combined effects of the soil shear deformation and ground settlement. This unconventional dynamic behaviour provides an insight to better understand the resilience and life-long performance of earthquakes exposed underground structures.

In the fifth section, the acceleration amplification factors of soil and tunnel in the course of multiple seismic actions are presented. For the seismic response of the soil, it was observed that the acceleration amplification factors increased with the increasing of the elevation for all earthquake shakings, and the amplification effect of the ground decreased with the increasing of the amplitude of input motions due to the soil non-linearity behaviour. The amplification factors were influenced by the combined effects of the soil shear deformation and ground settlement during the whole process. The degree depended on which effect played a dominant role. Moreover, it could be seen that at the same elevation, the acceleration amplification factors in two models matched well except for the local cases. This finding demonstrated that the geofoam boundaries in two models were effective to prevent the reflections and refractions of seismic waves, the preparation of two models were successful, and the influence of the tunnel presence on the soil response was very limited. In addition, it could be seen that the Fourier amplitude in two models increased from the shaking table surface to the ground level, and the trend of amplification was obvious. It was evident that the high-frequency content was lost when the seismic waves cross the tunnel by comparing the Fourier spectrum of ground level accelerometers, indicating that the presence of tunnel had an impact on the soil response. For the seismic response of the tunnel, the variation of acceleration amplification factors of the tunnel lining was almost consistent with that of the soil accelerometer, when taking into account the combined effects of the soil shear deformation and ground settlement. The ground settlement could significantly influence the seismic response of tunnel structures. Also, the amplification factors increased with the increase of seismic intensity, which contrasted with the results of Wang et al. (2015) that the amplification factors decreased with the progressive increase of input intensity.

In the sixth section, the maximum seismic strains of tunnel lining are studied using the strain data at the monitoring positions. It could be seen that the tensile strains at the monitoring positions continuously increased during the shaking until the strain gauges were broken. The strain of springing was larger than the value of shoulder due to the stress concentration at the connection of invert and sidewall. The variation trends of two positions were consistent with the trend of the surface settlements, implying that the ground settlement played an important role on the seismic response of tunnel structures. Moreover, the variation trend of springing strains fitted to the trend of damage index results, indicating the accuracy of image processing.

Overall, the findings are a precursor to better understand the resilience and life-long performance of earthquake exposed underground structures. They can support, as validating data, the development of means to replicate the non-classical soil-structure interaction mechanisms that pertain when cumulative earthquake load is applied, and subsequently lead to unconventional dynamic behaviour. These are important to assess the health condition of operational tunnel and provide timely and necessary rehabilitation. Furthermore, there is a pressing need to investigate the cumulative effect of earthquakes on actual monitored tunnels, which could allow us to fully understand such effect and verify the presented results.

5.2 Future work

Based on the results in this thesis, the following suggestions could be made for further investigations,

- In this study, the cumulative effect of multiple moderate or severe seismic events on tunnels was explored and the continuous damage of structures was observed. However, the impact of low seismic shakings was not well-understood. It is necessary to investigate the seismic performance of tunnels under multiple earthquake actions that are small ones not able to exert sizeable damage.

- The proposed cracking monitoring system equipped with mini-cameras focused on the vulnerable positions of tunnel lining. Therefore, in order to record the performance of full-lining sections, the system should be redesigned. Then, a damage grading system under multiple earthquake shakings could be proposed based on the image-based damage index, dynamic properties of lining and settlements of ground surface. It could be used to conduct the vulnerability assessment of exiting tunnels by fragility curves. In addition, with the increasing of volume of image data, deep learning, such as convolutional neural networks (CNN)-based model and recurrent neural networks (RNN)-based model, can be used for automatic feature extraction in future studies.
- 3D laser scanning technology was used to monitor the surface changes. Due to the scanning field of scanner, there were blind areas in two model boxes, which leaded to the incomplete data. In order to reduce the blind area, more scan stations may be employed after the seismic shaking, but more scanning time is required. Therefore, the balance between the scanning time and resolution should be found. In addition, six target spheres were spatially fixed around the shaking table to reduce the registration errors in this study. The impact of different target sphere combinations on the surface change estimations could be further investigated. Moreover, the shape of the earthquake-induced settlement trough could be further studied quantitatively.
- In order to prevent the reflections and refractions of seismic waves during the tests, EPS geofoam was used to simulate the absorbing boundaries. Although the results indicated the effectiveness of geofoam, it was a simplified method. In the future work, the laminar box could be used to more accurately model the free-field boundary which has been attempted in recent shaking table test of tunnels (Xu et al., 2021; Yang et al., 2021). Moreover, tunnel end effects should be reduced in the model tests.
- This thesis investigated the transversal seismic performance of tunnel structures under

shear seismic waves. In practical, the seismic waves propagated in the surrounding soil at three directions, resulting in the three-dimensional seismic behaviour of tunnel structures. Also, asynchronous excitation can influence the seismic performance of tunnels significantly.

Bibliography

Ai, D., Jiang, G., Siew Kei, L., Li, C., 2018. Automatic pixel-level pavement crack detection using information of multi-scale neighborhoods, IEEE Access 6, 24452–24463.

American Lifelines Alliance (ALA), 2001. Seismic Fragility Formulation for Water Systems, part 1. Guideline, ASCE-FEMA, Reston, VA, pp. 2001.

Andreotti, G., Lai, C., 2019. Use of fragility curves to assess the seismic vulnerability in the risk analysis of mountain tunnels. Tunn. Undergr. Space Technol. 91, 103008.

Antoniou, M., Nikitas, N., Anastasopoulos, I., Fuentes, R., 2020. Scaling laws for shaking table testing of reinforced concrete tunnels accounting for post-cracking lining response. Tunnelling and Underground Space Technology. 101. 103353.

Argyroudis, S., Pitilakis, K., 2012. Seismic fragility curves of shallow tunnels in alluvial deposits. Soil Dynamics and Earthquake Engineering. 35: 1-12.

Argyroudis, S., Tsinidis, G., Gatti, F., Pitilakis, K., 2017. Effects of SSI and lining corrosion on the seismic vulnerability of shallow circular tunnels. Soil Dyn. Earthquake Eng. 98, 244–256.

Asakura, T., Sato, Y., 1996. Damage to mountain tunnels in hazard area. Soil Foundations. Special Issue. pp 301-310.

Asakura, T., Sato, Y., 1998. Mountain tunnels damage in the 1995 Hyogoken-nanbu Earthquake. Quart. Rep. RTRI (Railway Tech. Res. Inst.) 39 (1), 9–16.

Asakura, T., & Kojima, Y., 2003. Tunnel maintenance in Japan. Tunnelling and Underground Space Technology, 18(2–3), 161–169.

Attard, L., Debono, C.J., Valentino, G., Castro, M.D., 2018. Tunnel inspection using photogrammetric techniques and image processing: a review. ISPRS journal of photogrammetry and remote sensing. 144, 180–188.

Barnhart, T., Crosby, B., 2013. Comparing two methods of surface change detection on an evolving thermokarst using high-temporal-frequency terrestrial laser scanning, Selawik River, Alaska. Remote Sensing. 5(6), 2813–2837.

Benjamin, J., Rosser, N., Brain, M., 2016 Rockfall Detection and Volumetric Characterisation Using LiDAR. In Landslides and Engineered Slopes. Experience, Theory and Practice: Proceedings of the 12th International Symposium on Landslides; CRC Press: Naples, Italy, pp. 389–395.

Bernard, T.G., Lague, D., Steer, P., 2020. Beyond 2D inventories: synoptic 3D landslide volume calculation from repeat LiDAR data. Earth Surf. Dyn. Discus. 1–28.

Bradley, D., Roth, G., 2007. Adapting Thresholding Using the Integral Image. Journal of Graphics Tools. 12 (2): 13–21.

Brodu, N., Lague, D., 2012. 3D terrestrial lidar data classification of complex natural scenes using a multi-scale dimensionality criterion: Applications in geomorphology. ISPRS Journal of Photogrammetry and Remote Sensing. 68, 121–134.

Carpinteri, A., 1982. Notch sensitivity in fracture testing of aggregative materials. Eng. Fract. Mech. 16 (4), 467–481.

Carpinteri, A., 1984. Stability of fracturing process in RC beams. J. Struct. Eng. 110 (3), 544–558.

Chen, J., Shi, X., Li, J., 2010. Shaking table test of utility tunnel under non-uniform earthquake wave excitation. Soil Dyn. Earthquake Eng. 30 (11), 1400–1416.

Chen, G.X., Wang, Z.H., Zuo, X., Du, X.L., Gao, H.M., 2013. Shaking table test on the seismic failure characteristics of a subway station structure on liquefiable ground. Earthquake Engineering and Structural Dynamics. 42(10): 1489–507.

Chen, G.X., Chen, S., Zuo, X., Du, X.L., Qi. C.Z., Wang, Z.H., 2015. Shaking-table tests and numerical simulations on a subway structure in soft soil. Soil Dynamic and Earthquake Engineering. 76: 13-28.

Chen, G.X., Shen, S., Qi, C.Z., Du, X.L., Wang, Z.H., Chen, W.Y., 2015. Shaking table tests on a three-arch type subway station structure in a liquefiable soil. Bull Earthquake Eng. 13, 1675–1701.

Chen, S., Tang, B., Zhao, K., Li, X., Zhuang, H., 2020. Seismic response of irregular underground structures under adverse soil conditions using shaking table tests. Tunn. Undergr. Space Technol. 95, 103145.

Chiu, Y.C., Kung, C.L., Wang, T.T., 2020. Site characteristics of a rock tunnel based on field-monitored seismic response. In: Proceeding of EUROCK 2020 - the ISRM European Rock Mechanics Symposium.

Cignoni, P., Rocchini, C., Scopigno, R., 1998. Metro: Measuring Error on Simplified Surfaces. Computer Graphics Forum. 17, 167–174.

Cilingir, U., Madabhushi, S.P.G., 2011. A model study on the effects of input motion on the seismic behaviour of tunnels. Soil Dyn. Earthquake Eng. 31, 452–462.

Cole, H.A., 1968. On-the-line analysis of random vibrations. In: Proceedings of the AIAA/ASME Ninth Structures. Structural Dynamics and Materials Conference, Palm Springs, CA, April1–3, 1968.

Corigliano, M., Lai, C., Barla, G. 2007. Seismic vulnerability of rock tunnels using fragility curves. In: 11th ISRM Congress, Lisbon, Portugal. International Society for Rock Mechanics.

Corrado, M., Cadamuro, E., Carpinteri, A., 2011. Dimensional analysis approach to study snap back-to-softening-to-ductile transitions in lightly reinforced quasi-brittle materials. Int. J. Fract. 172 (1), 53–63.

Daubechies, I., Lu, J., Wu, H.T., 2011. Synchrosqueezed wavelet transforms: an empirical mode decomposition-like tool. Appl Comput Harmon Anal. 30, 243–

261.

de Silva, F., Fabozzi, S., Nikitas, N., Bilotta, E., Fuentes, R., 2021. Seismic vulnerability of circular tunnels in sand. Geotechnique, 1–15.

DiFrancesco, P.M., Bonneau, D., Hutchinson, D.J., 2020. The Implications of M3C2 Projection Diameter on 3D Semi-Automated Rockfall Extraction from Sequential Terrestrial Laser Scanning Point Clouds. Remote Sensing. 12, 1885.

Dowding, C.H., Rozen, A., 1978. Damage to rock tunnels from earthquake shaking. J. Geotech. Eng. Div., ASCE 104 (GT2), 175-191.

Duke, C.M., Leeds, D.J., 1959. Effects of Earthquakes on Tunnels: Paper Presented at the RAND Second Protective Construction Symposium, March 24-26.

Eltner, A., Maas, H.-G., Faust, D., 2018. Soil micro-topography change detection at hillslopes in fragile Mediterranean landscapes. Geoderma. 313, 217–232.

Fabozzi, S., Bilotta, E., Lanzano, G., 2017. A numerical study on seismic vulnerability of tunnel linings. In: Proceedings of 3rd Performance Based Design in Earthquake Geotechnical Engineering. Vancouver, Canada, 16–19 June 2017.

Gao, C.D., Li, P.F., Hu, J.F., Yan, L., Latifi, H., Yao, W.Q., Hao, M.K., Gao, J.J., Dang, T.M., Zhang, S.H., 2021. Development of gully erosion processes: A 3D investigation based on field scouring experiments and laser scanning, Remote Sensing of Environment. 265, 112683.

GAQSIQ (General Administration of Quality Supervision, Inspection and Quarantine of China) and SA (Standardization Administration of China), 2010. Metallic materials---Tensile testing---Part 1: Method of test at room temperature (GB/T 228.1-2010). China Architecture & Building Press, Beijing, China.

Girardeau-Montaut D, Roux M, Marc R, Thibault G. 2005. Change detection on points cloud data acquired with a ground laser scanner. International Archives of Photogrammetry, Remote Sensing and Spatial Information Sciences. 36, 30–35.

Gomez-Gutierrez, A., Rito Goncalves, G., 2020. Surveying coastal cliffs using two UAV platforms (multirotor and fixed-wing) and three different approaches for the estimation of volumetric changes. International Journal of Remote Sensing. 41, 8143–8175.

Goodwin, N.R., Armston, J.D., Stiller, I., Muir, J., 2016. Assessing the repeatability of terrestrial laser scanning for monitoring gully topography: a case study from Aratula, Queensland, Australia. Geomorphology. 262, 24–36.

Han, J., El Naggar, M.H., Hou, B., Du, X., Shuai, Y., Li, L., 2020. Nonlinear soil response under non-uniform seismic excitation from multi-point shaking table tests. Soil Dynamics and Earthquake Engineering, 139, 106342.

Hashash, Y.M.A., Hook, J.J., Schmidt, B., Yao, J.I.C., 2001. Seismic design and analysis of underground structures. Tunn. Underground Space Technology 16 (2), 247–293.

HAZUS, 2004. Multi-Hazard Loss Estimation Methodology: Earthquake Model. Department of Homeland Security, FEMA, Washington, DC, USA.

Huang, C.X., Wang, X.H., Zhou, H., Liang, Y., 2019. Damping effects of different shock absorbing materials for tunnel under seismic loadings. Journal of Vibroengineering. 21(5): 1353-1372.

Huang, T.H., Ho, T.Y., Yao, X.L., Chang, Q.D., Lee, H.C., 1999. Quick investigation and assessment on tunnel structures after earthquake, and the relevant reinforced methods (in Chinese). Report for the Public Construction Commission, Taipei, Taiwan.

Huang, H., Sun, Y., Xue, Y., Wang, F., 2017. Inspection equipment study for subway tunnel defects by grey-scale image processing. Adv. Eng. Inform. J. 32, 188–201.

Huang, G., Qiu, W., Zhang, J., 2017. Modelling seismic fragility of a rock mountain tunnel based on support vector machine. Soil Dyn. Earthquake Eng. 102, 160–

171.

Huang, Z., Argyroudis, S., Pitilakis, K., Zhang, D., Tsinidis, G., 2022. Fragility assessment of tunnels in soft soils using artificial neural networks. Undergr. Space.

Ikuma, M., 2005. Maintenance of the undersea section of the Seikan Tunnel. Tunn. Undergr. Space Technol. 20 (2), 143–149.

Jiang L.Z., Chen J., Li J., 2010. Seismic response of underground utility tunnels: shaking table testing and FEM analysis. Earthquake Eng. Eng. Vib. 9, 555–567.

Koch, C., Georgieva, K., Kasireddy, V., Akinci, B., Fieguth, P.A., 2015. A review on computer vision based defect detection and condition assessment of concrete and asphalt civil infrastructure. Adv. Eng. Inf. 29, 196–210.

Kong, T.Y., Azriel R., 1996. Topological Algorithms for Digital Image Processing, Elsevier Science, Inc.

Kontoe, S., Zdravkovic, L., Potts, D., Mentiki, C., 2011. On the relative merits of simple and advanced constitutive models in dynamic analysis of tunnels. Geotechnique 61 (10), 815–829.

Kramer, S.L., 1996. Geotechnical earthquake engineering. Prentice Hall, Upper Saddle River, N.J. 653 pp.

Lague, D., Brodu, N., Leroux, J., 2013. Accurate 3D comparison of complex topography with terrestrial laser scanner: application to the Rangitikei canyon (N-Z). ISPRS Journal of Photogrammetry and Remote Sensing. 82, 10–26.

Langhaar, H., 1951. Dimensional Analysis and Theory of Models, John Wiley and Sons, New York.

Lanzano, G., Bilotta, E., Russo, G., Silvestri, F., Madabhushi, S.P.G., 2012. Centrifuge modelling of seismic loading on tunnels in sand. Geotech. Test. J. 35 (6), 854–869.

Li, T.B., 2012. Damage to mountain tunnels related to the Wenchuan earthquake and some suggestions for aseismic tunnel construction. Bull. Eng. Geol. Environ. 71 (2), 297–308.

Li, L., Nearing, M.A., Nichols, M.H., Polyakov, V.O., Cavanaugh, M.L., 2020. Using terrestrial LiDAR to measure water erosion on stony plots under simulated rainfall. Earth Surf. Process. Landf. 45, 484–495.

Lim, J.S., 1990. Two-Dimensional Signal and Image Processing, Englewood Cliffs, NJ, Prentice Hall. pp: 469-476.

Lin, G., Zhu, T., Lin B., 2000. Similarity technique for dynamic structural model test. Journal of Dalian University of Technology. 40(1), 1-8. (in Chinese)

Maurer, C., Qi, R., Raghavan, V., 2003. A Linear Time Algorithm for Computing Exact Euclidean Distance Transforms of Binary Images in Arbitrary Dimensions. IEEE Transactions on Pattern Analysis and Machine Intelligence, 25(2), 265-270.

Meng, G.W., Zhou, J.M., Gao, B., 2016. Study on seismic response of fiber reinforced concrete tunnel lining with shaking table test. Chinese Journal of Rock Mechanics and Engineering. 35, 1-9. (in Chinese)

Meymand, P.J., 1998. Shaking Table Scale Model Tests of Nonlinear Soil-Pile-Superstructure Interaction in Soft Clay, PhD dissertation, U.C. Berkeley.

MOC (Ministry of Construction of China) and GAQSIQ (General Administration of Quality Supervision, Inspection and Quarantine of China), 2002. Standard for test method of mechanical properties on ordinary concrete (GB/T 50081-2002). China Architecture & Building Press, Beijing, China.

MOHURD (Ministry of Housing and Urban-Rural Development of China) and AMR (Administration for Market Regulation of China), 2019. Standard for geotechnical testing method (GB/T 50123-2019), China Planning Press, Beijing, China.

MOHURD (Ministry of Housing and Urban-Rural Development of China), 2009. Standard for test method of basic properties of construction mortar (JGJ/T 70-2009), China Architecture & Building Press, Beijing, China.

Mohan, A., Poobal, S. 2017. Crack detection using image processing: a critical review and analysis. Alex. Eng. J. 57, 787–798.

National Research Council, 2013. Underground engineering for sustainable urban development. National Academies Press.

Oliveira, H., Correia, P.L., 2013. Automatic road crack detection and characterization. IEEE Transactions on Intelligent Transportation System. 14(1): 155−168.

Ouyang, A., Luo, C., Zhou, C., 2011. Surface distresses detection of pavement based on digital image processing, Computer and Computing Technologies in Agriculture IV. pp: 368–375.

Owen, G.N., Scholl, R.E., 1981. Earthquake engineering of large underground structures. Report no. FHWA/RD-80/195. Federal Highway Administration and National Science Foundation.

Qi, D., Liu, Y., Gu, Q., Zheng, F., 2014. An algorithm to detect the crack in the tunnel based on the image processing. Journal of Computers. 26(3): 11-19.

Qin, R., Tian, J., Reinartz, P., 2016. 3D change detection – Approaches and applications. ISPRS Journal of Photogrammetry and Remote Sensing. 122, 41–56.

Quan, D.Z., 2016. Seismic response characteristic and calculation method of subway station in loess (Ph.D. thesis). Chang’ an University. (in Chinese)

Rodrigues, J., Brincker, R., 2005. Application of the random decrement technique in operational modal analysis. In: Proceedings of the 1st International Operational Modal Analysis Conference, Copenhagen, Denmark, April 26–27, pp. 191–200.

Sharma, S., Judd, W.R., 1991. Underground opening damage from earthquakes. Eng. Geol. 30, 263-276.

Shen, Y.S., Gao, B., Yang, X.M., Tao, S.J., 2014. Seismic damage mechanism and dynamic deformation characteristic analysis of mountain tunnel after Wenchuan earthquake. Eng. Geol. 180, 85–98.

Shen, Y.S., Wang, Z.Z., Yu, J., Zhang, X., Gao, B., 2020. 1.Shaking table test on flexible joints of mountain tunnels passing through normal fault. Tunn. Undergr. Sp. Technol. 98, 103299.

Shen, B., Zhang, W., Qi, D., Wu, X., 2015. Wireless multimedia sensor network based subway tunnel crack detection method. Int. J. Distrib. Sensor Networks. 11(6).

Spencer, B.F., Hoskere, V., Narazaki, Y., 2019. Advances in Computer Vision-Based Civil Infrastructure Inspection and Monitoring. Engineering 5, 199–222.

Stevens, P.R., 1977. A review of the effects of earthquakes on underground mines. United States Geological Survey Open File Report 77-313. US Energy Research and Development Administration, Reston, VA.

Sui, C.Y., Gao, B., Shen, Y.S., Wang, J.X., Wang, S.S., 2017. Shaking table test and analysis on tunnel structures with high steep slope. Journal of Vibration and Shock. 36 (19): 186-194. (in Chinese)

Sun, T., Yue, Z., Gao, B., Li, Q., Zhang, Y., 2011. Model test study on the dynamic response of the portal section of two parallel tunnels in a seismically active area. Tunn. Undergr. Space Technol. 26 (2), 391–397.

Sun, B.B., Zhang, S.R., Deng, M.J., Wang, C., 2020. Nonlinear dynamic analysis and damage evaluation of hydraulic arched tunnels under mainshock-aftershock ground motion sequences. Tunn. Undergr. Sp. Tech. 98, 103321.

Tao, S.J., Gao, B., Xin, C.L., 2015. Seismic damage analysis of tunnel front slope and shaking table tests on highway tunnel portal. Electronic Journal of Geotechnical Engineering. 20: 2167-2182.

Telling, J., Lyda, A., Hartzell, P., Glennie, C., 2017 Review of Earth Science Research Using Terrestrial Laser Scanning. Earth-Science Rev. 169, 35–68.

Tsinidis, G., Pitilakis, K., Madabhushi, G., Heron, C., 2015a. Dynamic response of flexible square tunnels: centrifuge testing and validation of existing design methodologies. Géotechnique 65 (5), 401–417.

Tsinidis, G., Heron, C., Pitilakis, K., Madabhushi, G., 2015b. Centrifuge modelling of the dynamic behavior of square tunnels in sand. In: Taucer, F., Apostolska, R. (eds), Experimental Research in Earthquake Engineering. Geotechnical and Geological Earthquake Engineering, vol. 35, Springer, Switzerland, pp 509–523.

Tsinidis, G., de Silva, F., Anastasopoulos, I., et al., 2020. Seismic behaviour of tunnels: from experiments to analysis. Tunn. Undergr. Sp. Tech. 99, 103334.

Ukai, M., 2007. Advanced inspection system of tunnel wall deformation using image processing. Quart. Rep. RTRI. 48 (2), 94–98.

United Nations, 2019. World Urbanization Prospects: The 2018 Revision., United Nations Department of Economic and Social Affairs.

Vamvatsikos, D., Cornell, C.A., 2002. Incremental dynamic analysis. Earthq Eng Struct Dyn. 31 (3), 491-514.

Wang, J.N., 1993. Seismic Design of Tunnels: A State-of-the-Art Approach, Monograph, monograph 7. Parsons, Brinckerhoff, Quade and Douglas Inc, New York.

Wang, W.L., Wang, T.T., Su, J.J., Lin, C.H., Seng, C.R., Huang, T.H., 2001. Assessment of damage in mountain tunnels due to the Taiwan Chi-Chi earthquake. Tunneling and Underground Space Technology. 16, 133-150.

Wang, Z.Z., Gao, B., Jiang, Y.J., Yuan, S., 2009. Investigation and assessment on mountain tunnels and geotechnical damage after the Wenchuan earthquake. Sci. China, Ser. E-Technol. Sci. 52 (2), 546–558.

Wang, Z.Z., Zhang, Z., 2013. Seismic damage classification and risk assessment of mountain tunnels with a validation for the 2008 Wenchuan earthquake. Soil Dyn. Earthquake Eng. 45, 45–55.

Wang, Z.Z., Jiang, Y.J., Zhu, C.A., Sun, T.C., 2015. Shaking table tests of tunnel linings in progressive states of damage. Tunn. Undergr. Space Technol. 50, 109–117.

Wang, G.B., Yuan, M.Z., Miao, Y., et al., 2018. Experimental study on seismic response of underground tunnel–soil–surface structure interaction system. Tunn. Undergr. Space Technol. 76, 145–159.

Wang, B., Zhang, Z., He, C., Zheng, H., 2017. Implementation of a long-term monitoring approach for the operational safety of highway tunnel structures in a severely seismic area of China. Struct. Control Health Monitor. 24 (11), e1993.

Wheaton, J.M., Brasington, J., Darby, S.E., Sear, D.A., 2010. Accounting for uncertainty in DEMs from repeat topographic surveys: improved sediment budgets. Earth Surface Processes and Landforms: the journal of the British Geomorphological Research Group. 35(2), 136–156.

Winiwarter, L., Anders, K., Höfle, B., (2021). M3C2-EP: Pushing the limits of 3D topographic point cloud change detection by error propagation. ISPRS Journal of Photogrammetry and Remote Sensing. 178, 240–258.

Xin, C.L., Gao, B., 2014. Shaking table tests on seismic damage mechanism of lining structures in mountain highway tunnel. Electronic Journal of Geotechnical Engineering. 19: 6795-6806.

Xin, C.L., Wang, Z.Z., Zhou, J.M., Gao, B., 2019. Shaking table tests on seismic behavior of polypropylene fiber reinforced concrete tunnel lining. Tunn. Undergr. Space Technol. 88, 1–15.

Xu, H., Li, T., Xia, L., Zhao, J.X., Wang, D., 2016. Shaking table tests on seismic measures of a model mountain tunnel. Tunn. Undergr. Sp. Tech. 60, 197–209.

Xu, C., Jiang, Z., Du, X., Shen, Y., Chen, S., 2021. 1-g shaking table tests of precast horseshoe segmental tunnel: Experimental design, dynamic properties, deformation mode and damage pattern. Tunn. Undergr. Space Technol. 113, 103976.

Xu, C., Jiang, Zhi., Du, X., Zhong, Z., Shen, Y., 2022. Seismic Displacement and Deformation Analyses of a Precast Horseshoe Segmental Tunnel. Tunn. Undergr. Space Technol, 124: 104476.

Yang, B., Zheng, Y.Z., Lai, J., Liu, Y., Li, X.D., 2015. Shaking Table Model Test and Numerical Modeling for Tunnels Traversing Faultage. The Open Civil Engineering Journal, 9, 789-798.

Yang, Y.S., Yu, H.T., Yuan, Y., Sun, J., 2021. 1 g Shaking table test of segmental tunnel in sand under near-fault motions. Tunn. Undergr. Space Technol. 115, 104080.

Yu, Y.Y., 2013. Study on damage mechanism of lining structure of mountain tunnel. Institute of Engineering Mechanics, China Earthquake Administration. (in Chinese)

Yu, H.T., Chen, J.T., Yuan, Y., Zhao, X., 2016a. Seismic damage of mountain tunnels during the 5.12 Wenchuan earthquake. J. Mountain Sci. 13 (11), 1958–1972.

Yu, H., Chen, J., Bobet, A., Yuan, Y., 2016b. Damage observation and assessment of the Longxi tunnel during the Wenchuan earthquake. Tunn. Undergr. Space Technol. 54, 102–116.

Yu, H., Yan, X., Bobet, A., Yuan, Y., Xu, G., Su, Q., 2018. Multi-point shaking table test of a long tunnel subjected to non-uniform seismic loadings. Bull. Earthq. Eng. 16 (2), 1041–1059.

Yuan, Y., Yang, Y., Zhang, S., et al., 2020. A benchmark 1 g shaking table test of shallow segmental mini-tunnel in sand. B Earthq. Eng. 18, 5383–5412.

Zhang, M.Z., 1997. Study on similitude laws for shaking table tests. Earthquake Engineering and Engineering Vibration. 17 (2), 52-58.

Zhang, W., Zhang, Z., Qi, D., Liu, Y., 2014. Automatic crack detection and classification method for subway tunnel safety monitoring. Sensors. 14 (10), 19307–19328.

Zhang, W., Han, L., Feng, L., Ding, X., Wang, L., Chen, Z., et al., 2020. Study on seismic behaviors of a double box utility tunnel with joint connections using shaking table model tests. Soil Dyn Earthq Eng. 136, 106118.

Appendix

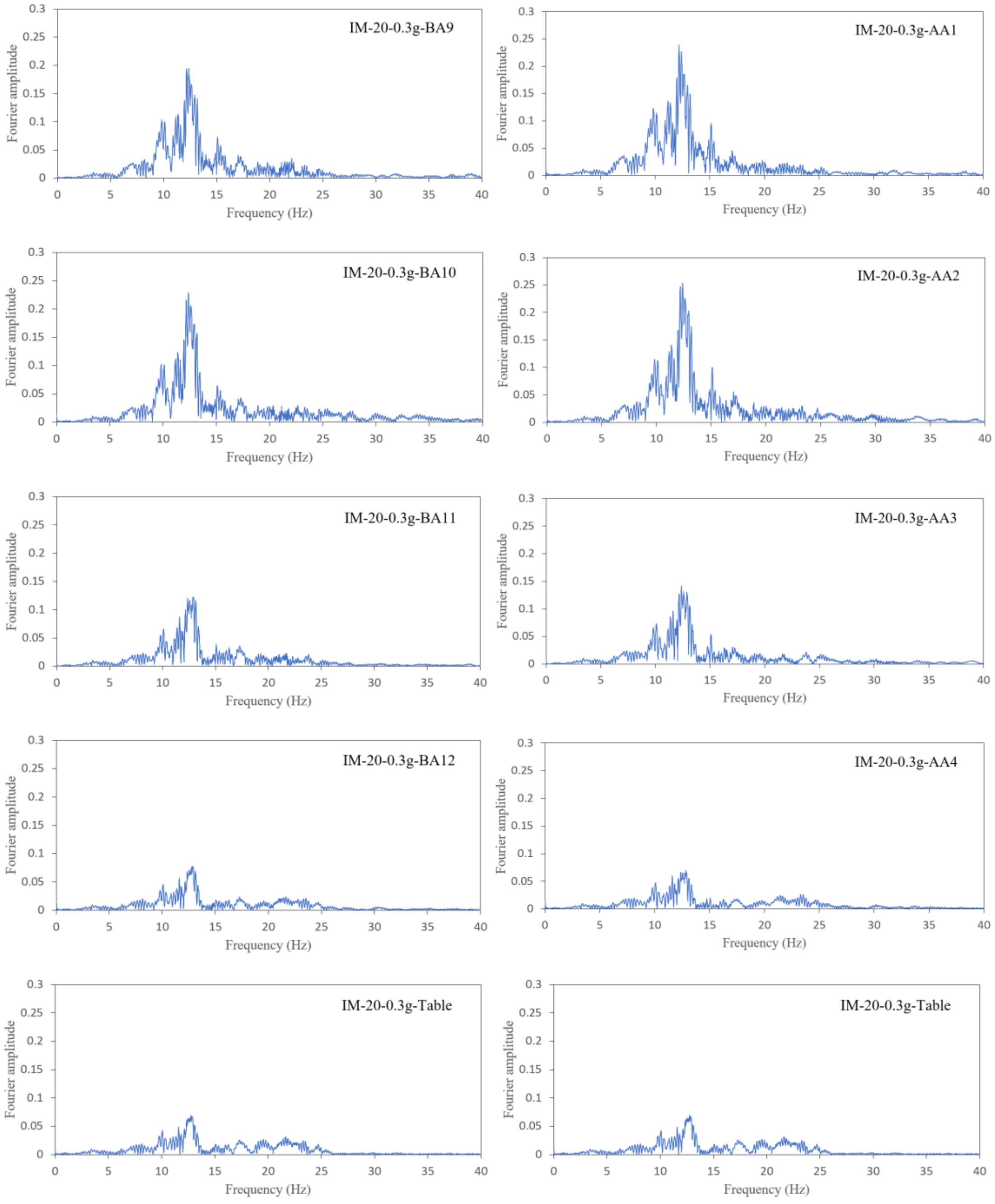

A.1: FFTs of soil accelerometers in IM-20-0.3g.

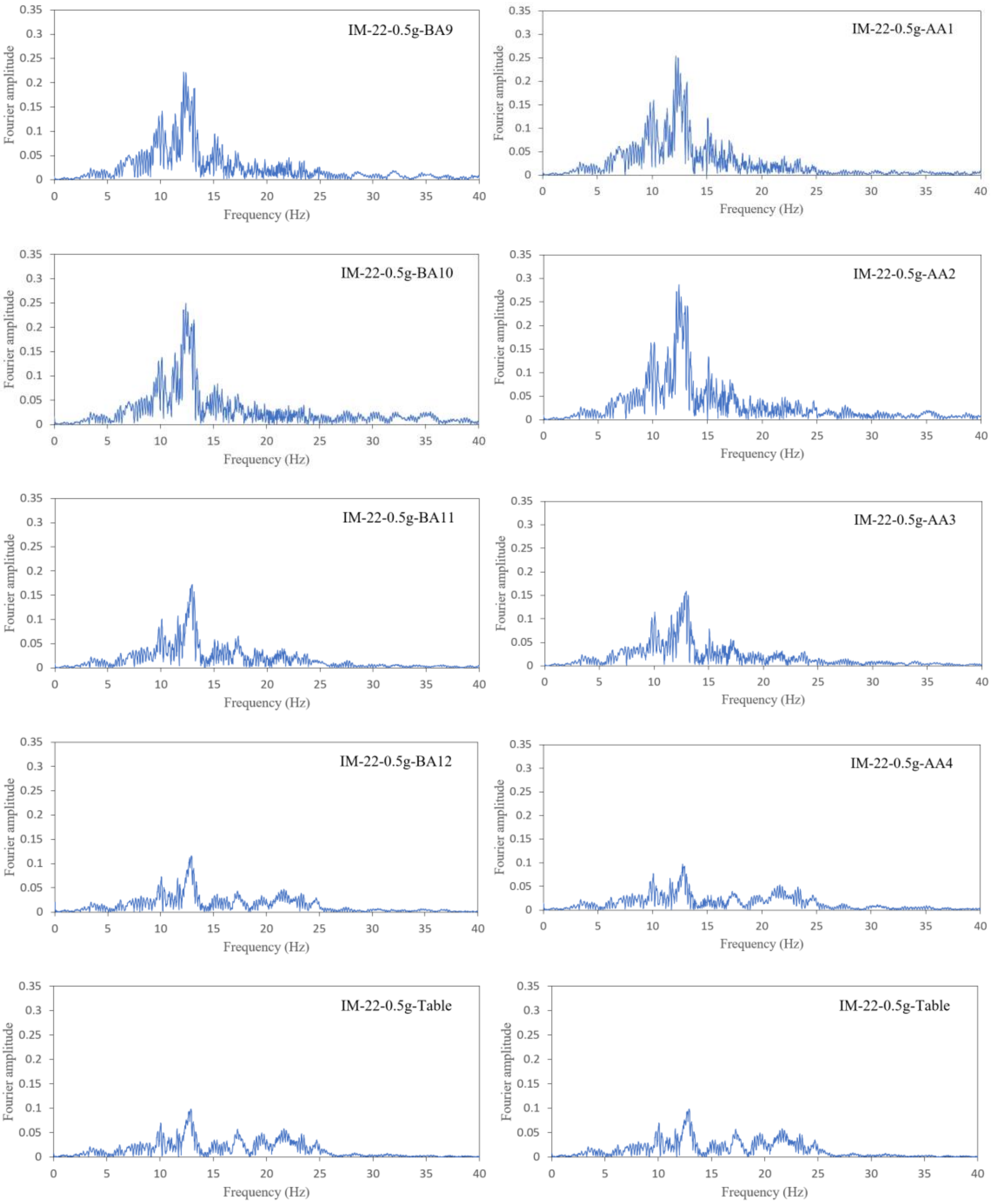

A.2: FFTs of soil accelerometers in IM-22-0.5g.

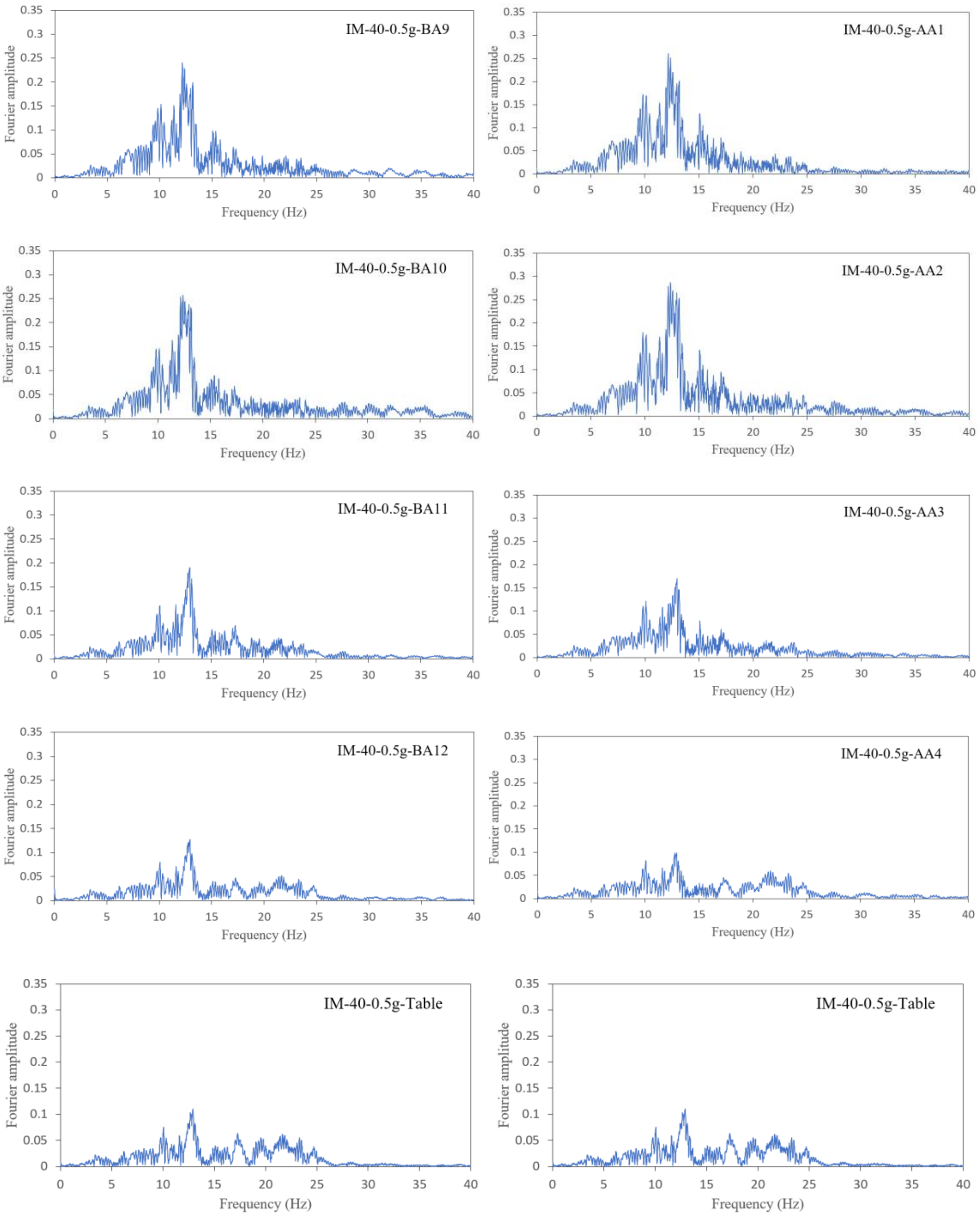

A.3: FFTs of soil accelerometers in IM-40-0.5g.

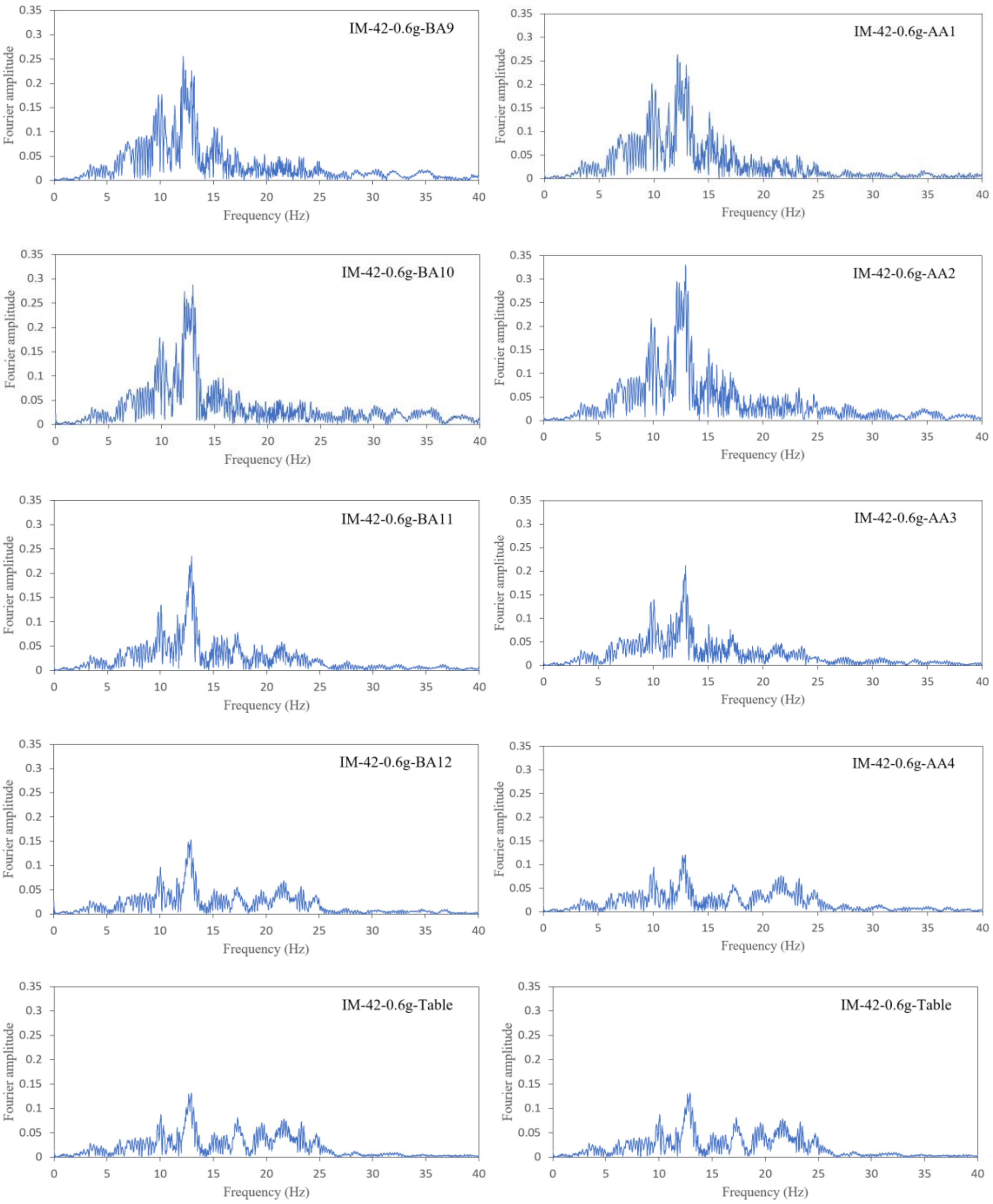

A.4: FFTs of soil accelerometers in IM-42-0.6g.

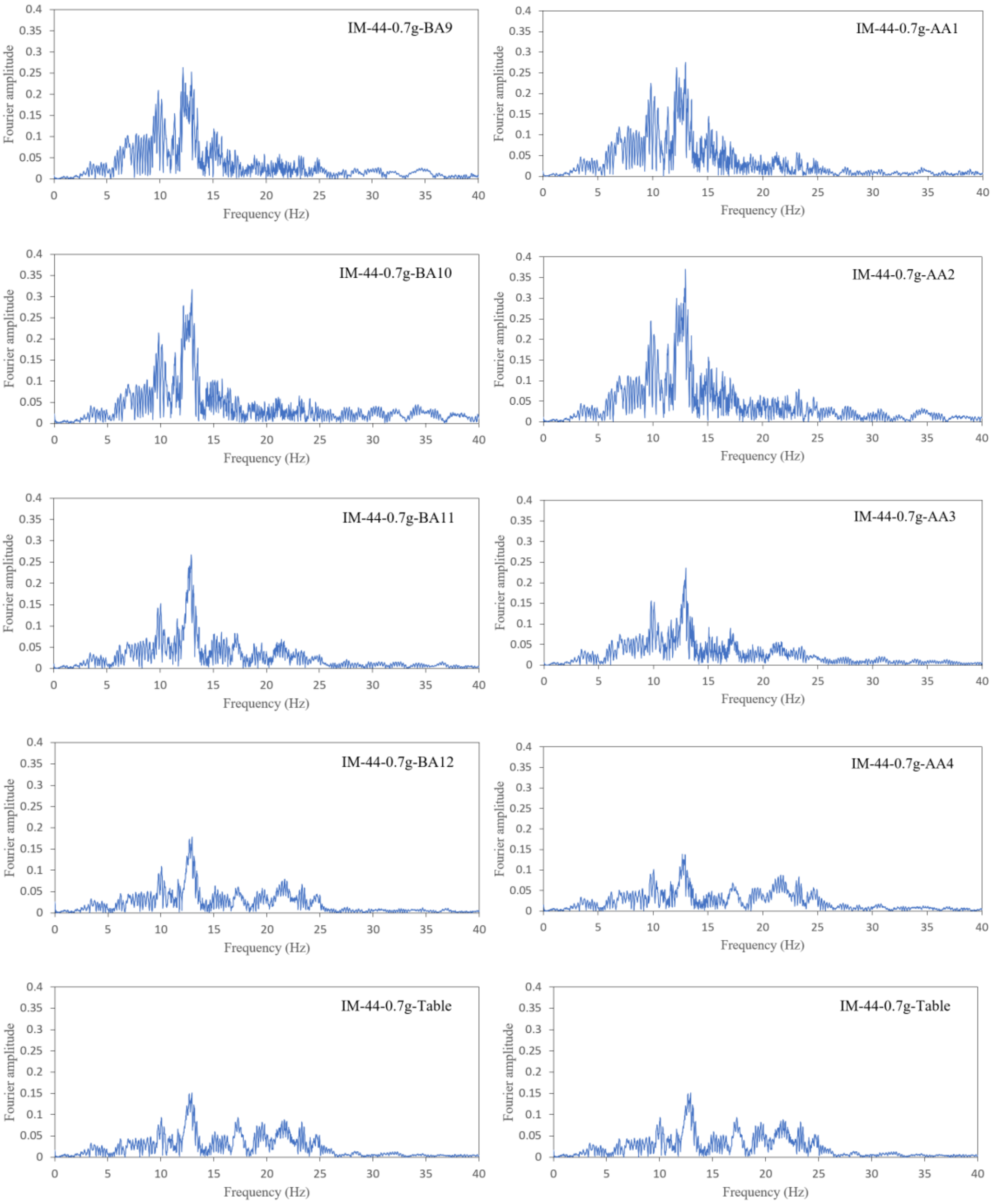

A.5: FFTs of soil accelerometers in IM-44-0.7g.

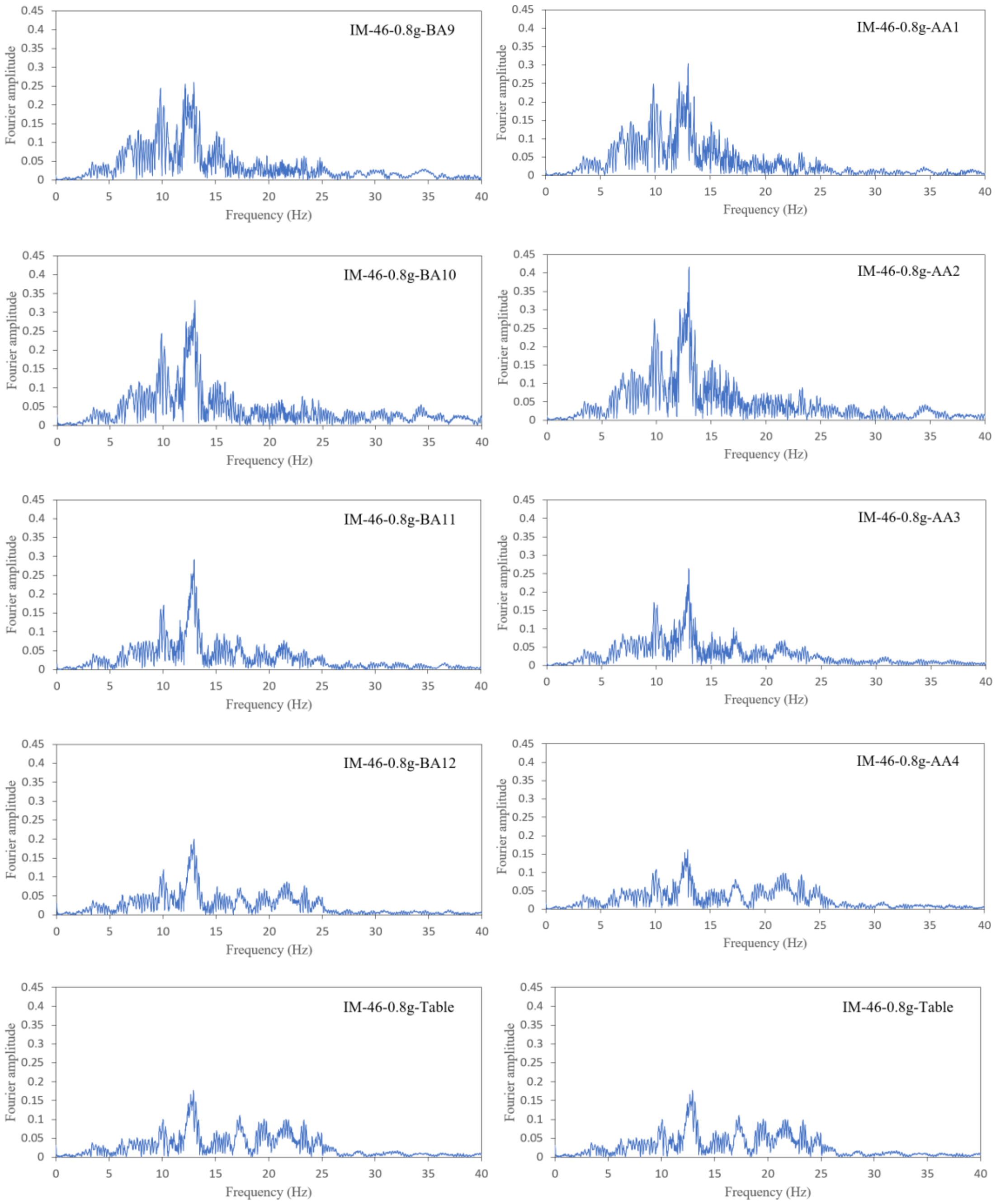

A.6: FFTs of soil accelerometers in IM-46-0.8g.